Tiago Peixoto da Silva Lobo

Gap soliton transparency switching and defect mode formation in one-dimensional Kerr-metamaterial superlattices and strips

Brazil

November 2017

Tiago Peixoto da Silva Lobo

Gap soliton transparency switching and defect mode formation in one-dimensional Kerr-metamaterial superlattices and strips

Thesis presented to the *Program de Pós Graduação em Materiais* in partial fulfillments of the requirements for the degree of *Doutor em Ciências.*

Universidade Federal de Alagoas – UFAL

Programa de Pós-Graduação em Materiais

Supervisor: Solange Bessa Cavalcati

Brazil

November 2017
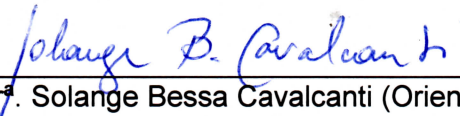
Tiago Peixoto da Silva Lôbo

Gap soliton transparency switching and defect mode formation in one-dimensional Kerr-metamaterial superlattices and strips

Tese apresentada ao Programa de Pós-Graduação em Materiais da Universidade Federal de Alagoas e aprovada em 29 de Novembro de 2017.

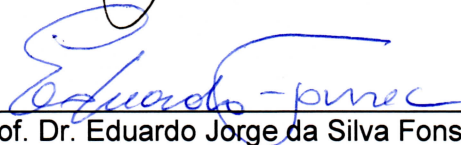## BANCA EXAMINADORA

Profª. Drª. Solange Bessa Cavalcanti (Orientadora - PPGMateriais/UFAL)

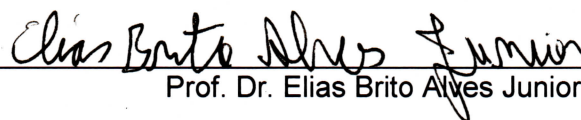Prof. Dr. Luiz Eduardo Moreira Carvalho de Oliveira (UNICAMP)

Prof. Dr. Eduardo Jorge da Silva Fonseca (PPGMateriais/UFAL)

Prof. Dr. Frederico Correia Moreira (CECA/UFAL)

Prof. Dr. Alex Emanuel Barros Costa (IFAL)

Prof. Dr. Elias Brito Alves Junior

Acknowledgements

Abstract

Plasmon-polariton gap soliton formation and transparency switching in one-dimensional nonlinear layered systems composed of alternate layers of a Kerr material and a dispersive linear metamaterial are theoretically studied. The behavior of the electric field profile inside the layered system is shown for different values of nonlinear power, linking the localized modes of the electric field with complete transparency states of the system. A detailed investigation on the influence of a defocusing nonlinearity on the transmission switching phenomenon, in the frequency range where the linear dispersion predicts the photon-plasmon coupling, is made, revealing different effects in the top and bottom edges of the plasmon-polariton gap. Specifically, we found a broadening of the plasmon-polariton gap when increasing the nonlinear power. In addition, a switching from very low to high transmission states is obtained and localized plasmon-polariton gap solitons of various orders are found for various values of frequencies and nonlinear strength.

Defect modes in a reduced lattice composed of a regular material sandwiched by a bilayer Kerr/dispersive metamaterial are also studied. The behavior of the electric profile inside the strips is studied for varying defect layer size and for an increasing focusing nonlinearity, linking each transparency point to a defect mode. In addition, the transmission function is found to be periodic in the linear regime and this periodicity is not affected by a focusing nonlinearity. Furthermore, each defect mode is linked to a n-peak electric field profile and a well defined parity. By choosing consecutive defect modes we have shown that the parity is switched and the electric field profile gets a new peak added to it, in the linear regime. Moreover, by fixing a defect layer size and studying the effects of an increasing focusing nonlinearity we found multistability, hysteresis and observed parity switch and new peaks being added to the electric profile as one chooses consecutive transparency points.

Keywords: Solitons, Transparency switching, Kerr material, Metamaterial, Band-gap, Plasmon-polariton, Parity Switch, Defect Modes.

Resumo

A formação de sólitons no gap plasmon-polariton e alterações no estado de transmissão de uma rede não linear unidimensional composta de camadas alternadas de um material Kerr e um metamaterial dispersivo linear são estudados teoricamente. O comportamento do perfil do campo elétrico dentro da estrutura estratificada é mostrado para diferentes valores da potência não-linear, conectando os modos localizados do campo elétrico com estados de transmissão total do sistema. Uma investigação detalhada da influência de uma não-linearidade desfocalizadora no fenômeno de alternância de transmissão, na faixa de frequência onde a dispersão linear prediz o acoplamento fóton-plasmon, é feita, revelando diferentes efeitos para as bordas inferiores e superiores do gap plasmon-polariton. Especificamente, nós achamos um alargamento do gap plasmon-polariton com o aumento da potência não-linear. Em adição, uma alternância dos estados de trânsmissão de muito baixos para muito altos foi observado e gap sólitons plasmon-polaritons de várias ordens foram achados para vários valores de frequência e potência não linear.

Modos defeito em uma rede reduzida composta de um material regular entre bicamadas Kerr/metamaterial dispersivo também são estudados. O comportamento do perfil do campo elétrico dentro das camadas é estudado para variáveis valores da camada defeito e para uma não linearidade focalizadora crescente, ligando cada ponto de transparência a um modo defeito. Em adição, achamos que a função transmissão é periódica no regime linear, e que essa periodicidade não é afetada por uma não linearidade focalizadora. Além disso, cada ponto defeito é ligado à um perfil do campo elétrico de n-picos e possuem paridade bem definida. Ao escolher modos defeito consecutivos mostra-se que a paridade é alternada e que o perfil do campo elétrico tem um novo pico adicionado a ele, no regime linear. Ademais, ao fixar o tamanho da camada defeito, o estudo dos efeitos de uma não linearidade focalizadora revela um perfil multiestável, histerese e alternância de paridade e novos picos sendo adicionados ao perfil do campo elétrico quando pontos de transparência consecutivos são observados.

Palavras-chave: Solitons, Alternância de transparência, Material Kerr, Metamaterial, Band-gap, Plasmon-polariton

List of Figures

Contents

1 Introduction

In the last few decades, researchers all over the world have managed to produce artificial complex materials widely used to shape and manipulate light (VALENTINE et al., 2008; VALENTINE et al., 2009). The remarkable flexibility of high-quality optical materials has allowed the fabrication of nanostructures (VESELAGO, 1968; SHELBY; SMITH; SCHULTZ, 2001), where one may tailor the electromagnetic dispersion and mode structures at one's choice, providing new phenomena for further investigations and new device applications. In addition, such new materials have given a refreshing flavor to old subjects as nonlinear wave propagation through one-dimensional (1D) layered systems (LI et al., 2003; JIANG et al., 2003). In particular, systems containing metamaterials, which exhibit electric and magnetic negative responses to an optical field within the same frequency range, provide excellent man-made materials for a number of areas of intense interest (PARAZZOLI et al., 2004; WILTSHIRE et al., 2001). Recently, the merging of plasmonic and metamaterial areas has opened up a new perspective toward achieving the ultimate control of light in the nanoscale dimension (FANG; KOSCHNY; SOUKOULIS, 2010; XIAO et al., 2010a).

Plasmon-polaritons (PPs) are elementary excitations due to the resonant coupling of plasmons with light. Recent work on the dispersion relation of a layered system composed by bilayers AB of a dispersive metamaterial (A) and air (B) has demonstrated that, under oblique incidence of light, a resonant coupling between a plasmon and a photon gives rise to a non-Bragg bulk-like PP gap at the plasmonic frequency (REYES-GÓMEZ et al., 2009; CARVALHO et al., 2011). As photons and plasmons have different dispersion relations, there is an anticrossing region evidencing the photon-plasmon coupling. Outside this region there is no coupling and therefore, plasmons and photons retrieve their individual character. By substituting the air layers by a nonlinear Kerr material, and choosing a particular frequency within the anticrossing region, multistability, transmission switch and resonant formation of soliton waves seem to occur at particular values of nonlinearity intensities for which total transmission ($T = 1$) is possible. Various layer arrangements were studied such as periodic, quasi-periodic and disordered arrangements, with absorption included, indicating that nonlinear switching with soliton formation is a robust phenomenon (REYES-GÓMEZ; CAVALCANTI; OLIVEIRA, 2014; REYES-GÓMEZ; CAVALCANTI; OLIVEIRA, 2015; REYES-GÓMEZ; CAVALCANTI; OLIVEIRA, 2016).

In this work we extend these previous findings on layered systems, to understand the role of nonlinearity on the dispersion relation around the anticrossing region. To this end, we investigate the transmission properties of incident light, under oblique incidence, upon a layered system composed of bilayers nonlinear/metamaterial in a periodic arrangement.

A thorough investigation on the influence of nonlinearity on the transparency-switching phenomenon is made, by sweeping the frequency region where the photon-plasmon coupling occurs in the case of a self-defocusing Kerr nonlinearity. It should be noted here that it has been previously shown (REYES-GÓMEZ; CAVALCANTI; OLIVEIRA, 2014) that the transparency switching phenomenon is robust with respect to absorption and could be observed even in the case of a single bilayer and relatively high levels of absorption. As expected, there are no total transmission states as those now have lower intensity, however the overall behavior is the same with or without absorption. For this reason, we neglect absorption and focus on the influence of the nonlinearity on the transparency switching phenomenon by sweeping the frequency region where the photon-plasmon coupling occurs in the case of a self-defocusing nonlinearity. We find that the detuning, that is, the depart of the frequency investigated from the resonant frequency, does not hinder soliton formation. Actually, we find that within the whole range of frequencies between the resonant points of total transmission ($T = 1$), lower intensity solitons of all orders are still formed. Furthermore, we show that in the self-defocusing case, the top edge of the PP gap is shifted to higher frequencies proportionally to the nonlinearity intensity while the lower PP gap edge essentially does not change in frequency. Thus, the "nonlinear PP gap" becomes larger than the linear one.

We also investigate defect modes in small one-dimensional photonic lattices composed of a regular material (with nondispersive permittivity and permeability) sandwiched between two bilayers made of Kerr/dispersive metamaterial. The regular material can be seen as a defect to a periodic lattice, raising the question of how the light propagates when the lattice has a local defect? For this reason, we theoretically analyze the linear defect modes in the linear and nonlinear regime for frequencies where the plasmon-polariton occurs, linking these modes to resonant modes of the system and to a parity switching phenomenon. Furthermore, we also show that the presence of a focusing Kerr nonlinearity does not change the periodicity of the transmission, linking the resonant modes in the presence of a focusing nonlienarity to a geometrical property of the system. Moreover, we show that consecutive defect modes increase the number of peaks of the electric profile and always have different parity. By choosing one defect mode and studying the influence of a focusing nonlienarity on its properties we also observe that consecutive resonant modes also present an increase in the number of peaks of the electric profile and possess different parity, linking the increase in the defect layer size to an increase in the light intensity.

We present our investigations on the role of the nonlinearity in the transparency switching phenomenon and in the defect modes of a nonlinear lattice as follows: chapter 2 is devoted to give an overview on metamaterials and plasmonic metamaterials, talking about some recent advances on the design and fabrication of materials with near zero permittivity or permeability; chapter 3 talks about the mathematical formalism necessary to study linear optical lattices, starting from Maxwell's equations we obtain the equation describing

light propagation in one-dimensional lattices, talk about the transfer matrix formulation, the Kronig-Penney model, and photonic band gaps; chapter 4 introduces the subject of nonlinear light propagation in media with a center of symmetry, reviewing some effects that stems from this: optical switching, multistability, hysteresis and soliton formation; chapter 5 gives an overview of the subject of gap-soliton formation; in chapter 6 we outline the computational program developed, and explain some new techniques designed in order to visualize our results, as well point out the main differences between our methodology and the literature; in chapter 7 we present our results on the defect modes of a nonlinear system for frequencies near the PP-gap edge; chapter 8 deals with the characterization of the transmission properties and the electric field profile of a lattice composed 32 bilayers of a linear dispersive metamaterial and a Kerr material for a defocusing nonlinearity and for frequencies near the PP gap; finally, in chapter 9 we present our conclusions and talk about future works.

2 Plasmonic metamaterials

In general, all materials are composites, even if they are made up by lots of small elements like atoms and molecules (for the naturally occurring ones). The way these elements are arranged changes the electromagnetic response of the material. In particular, two classifications are often used related to the spatial symmetries of the elements: amorphous, i.e., the elements are arranged in a random fashion; and crystalline, meaning that its constituents are in a periodical ordered arrangement. In order to calculate the electromagnetic properties of a homogeneous medium one needs to define (or describe) its permittivity ϵ and its permeability μ, both which depends on the spatial properties and the constituents of the material. This chapter aims to: give a brief overview on some theories used to describe optical materials; talk about recent advances in the desing and use of metamaterials and plasmonic materials.

2.1 Initial considerations

The focus of this thesis is in the interplay between electromagnetic waves and matter using only classical tools. Quantum effects will be disregarded unless explicited otherwise. Under these assumptions, two theories are dominant when studying electromagnetic wave propagation in matter: Bragg scattering (ASHCROFT; MERMIN, 1976) and the effective-medium approximation (LANDAUER, 1952; BRUGGEMAN, 1935). Bragg effects are important when the wavelength of the incident wave is comparable with the distance between elements in the material. When this happens, each constituent of the material in question reflects the wave. The way this reflected waves interact with other reflected waves and with the incident wave dictates the propagation of an electromagnetic wave through this kind of media. We call a Bragg reflection when the waves reflected by the elements interfere constructively reflecting most of the incident power. Consider a crystal made out of parallel planes of ions with spacing d. The condition for a peak in the reflection of the incident power of an incoming wave with wavelength λ is that the waves are specularly reflected (meaning that the incidence angle equals the angle of reflection) and that the reflected waves interfere constructively. The difference in the path of the waves reflected by two different planes is $2d\sin\theta$, where θ is the angle of incidence. To have a constructive interference this difference must be equal to an integer number of wavelengths, leading to the Bragg condition:

$$n\lambda = 2d\sin\theta; \tag{2.1}$$

where n is an integer.

The second effect of interest is given when the wavelength of the electromagnetic radiation is much larger than the lattice period. There is no considerable reflection or diffraction as the electromagnetic wave travels through the material, but they are still substantially affected. When this happens, the fine detail of the structure may be disregarded and replaced by a homogeneous and continuous material. Thus, one can find effective parameters, like the electric permittivity and magnetic permeability, to represent the material. This is known as the effective-medium approximation. This theory is the one we are interested in. When talking about materials we will talk about their effective permittivity and permeability, allowing mixtures, man-made materials and alloys, for example, to be studied under the same set of mathematical equations.

These effects (Bragg reflections, and the possibility of using effective values for the permittivity and permeability) are still of considerable importance when dealing with man-made materials, where the atoms and molecules are replaced by macroscopic elements, bigger than the molecules that normally constitute a material, but small enough that the effective medium approximation is still valid. By controlling the constituents of a material one can tailor its permittivity and permeability allowing a variety of effects that were impossible to obtain on ordinary materials (optical cloaking (CAI et al., 2007) and double negative materials (VESELAGO, 1968) for example). These man-made materials are called metamaterials. Huge attention has been given to this area in order to study, develop and design new metamaterials to a wide range of applications. Despite this, a more concise definition of what is a metamaterial is still hard to pinpoint. Here we will quote two definitions in current use (SOLYMAR; SHAMONINA, 2009):

- Metamaterials are engineered composites that exhibit superior properties not found in nature and not observed in the constituent materials.

- A metamaterial is an artificial material in which the electromagnetic properties, as represented by the permittivity and permeability, can be controlled. It is made up of periodic arrays of metallic resonant elements. Both the size of the element and the unit cell are small relative to the wavelength.

Both definitions have their flaws, the first one is not specific enough (mixtures, in general, are not metamaterials and fits the definitions), while the second one is too restrictive (the non-naturality of the assertion can be questioned). We will use the term metamaterial as a mix of the two definitions, engineered composites in which its permittivity and permeability can be controlled. A more curious header can find an extensive discussion about the meaning of the word metamaterial in (SIHVOLA, 2007).

Metamaterials are constituted of small macroscopic elements embedded in linear or nonlinear media in a specific arrangement (periodic, or not). The first double negative metamaterial was obtained by a periodic array of inter-spaced split ring resonators (SRR)

and continuous wires (SMITH et al., 2000). Since then, a great amount of research has been dedicated to the design of new metamaterials, for example: huge nonlinearities are found by using arrays of SRRs and cut wires as the unit cell (BAI et al., 2015); the development of a low-profile aperture capable of microwave imaging without lenses (HUNT et al., 2013); an invisibility cloak (SCHURIG et al., 2006).

When designing metamaterials one needs a theory to describe the materials, i.e., a way to find both permittivity and permeability of a material constituted of small macroscopic elements is necessary. In the effective-medium approximation specific models are used to obtain a more detailed understanding of both μ and ϵ. The Lorentz model provide a very good approximation for the electromagnetic response of dielectrics using only classical physics and the Drude model is remarkably accurate for metals and semiconductors. Despite being still used today these methods have their shortcomings. For example, the Lorentz model attributes a single resonance frequency to each atom. In comparison, the quantum description, which is detailed in (BOYD, 2008), allows more than one resonance frequency. The next section is devoted to briefly explain the Lorentz model and the Drude model.

2.2   Lorentz and Drude Model

In 1900, prior to development of quantum mechanics, Hendrik Lorentz described, using only classical mechanics, the interaction of light with matter in terms of Maxwell's equations. Even with only classical tools, the Lorentz oscillator model is able to describe accurately some materials and is still an important tool today. Lorentz developed a theory capable of accounting for both the complex dielectric constant of materials and its variation with the frequency of light. The model proposed treats the atom as a damped harmonic oscillator, i.e., electrons are considered bound to the nucleus of the atom with a spring-like force. This theory can be extended to treat nonlinear media by adding nonlinearities in the damped harmonic oscillator (BOYD, 2008). Following the Lorentz theory, the motion of an electron with position $x(t)$ is found by solving the following equation:

$$\frac{d^2}{dt^2}x(t) + 2\gamma\frac{d}{dt}x(t) + \omega_0^2 x^2(t) + \mathrm{N}\left(x(t)\right) = -e\frac{E(t)}{m}; \tag{2.2}$$

where $E(t)$ is an applied electric field, $-e$ is the charge of the electron, m is the electron mass, γ is the dipole damping rate, ω_0 is the resonance frequency and $N(x(t))$ is a nonlinear function of the electron position. The terms in eq. 2.2 have a physical meaning, $-2m\gamma dx(t)/dt$ is the damping force, while the term $-m\omega_0^2 x(t) + N(x(t))$ is the restoring force. This restoring force corresponds to a potential energy function of the form:

$$U(x(t)) = -\int -m\omega_0^2 x(t) + N(x(t))dx = \frac{1}{2}m\omega_0^2 x^2(t) - \int N(x)dx. \tag{2.3}$$

Assuming an applied optical field of the form:

$$E(t) = \sum_n E_n e^{-i\omega_n t} \qquad (2.4)$$

and that no nonlinerities are present ($N(x) = 0$), one obtain the usual Lorentz model result

$$x(t) = \sum_n \hat{x}(\omega_n) e^{-i\omega_n t} \qquad (2.5)$$

where:

$$\hat{x}(\omega_n) = -\frac{1}{m} \frac{e E_n(\omega_n)}{\omega_0^2 - \omega_n^2 - 2i\omega_n\gamma}. \qquad (2.6)$$

The polarization contribution (to the frequency ω_n) of all the dipoles generated by the incident field is given by $P^{(1)}(\omega_n) = -nex(\omega_n)$ (JACKSON, 1999), where n is the number density of atoms, while the linear susceptibility $\chi^{(1)}$ is defined as $P^{(1)}(\omega_n) = \epsilon_0 \chi^{(1)}(\omega_n) E(\omega_n)$. Thus, one can find that the linear susceptibility is given by:

$$\chi^1(\omega_n) = \frac{ne^2/m}{\epsilon_0 \left(\omega_0^2 - \omega_n^2 - 2i\omega_n\gamma \right)}. \qquad (2.7)$$

Despite its simplicity, the Lorentz model is still used to this day to study the properties of dielectrics (KATS et al., 2011; BAI et al., 2015). In addition, it can also be used to find higher order susceptibilities. To do so, one may replace $N(x)$ with the appropriate expression for the type of nonlinearity being treated and use a procedure similar to that of Rayleigh-Schrodinger perturbation theory in quantum mechanics to find the values of $\chi^{(n)}$ (BOYD, 2008). As of now, we will restrain our analysis to linear materials, i.e., materials where $\chi^{(n)} = 0$ for $n > 1$.

Despite all its advantages, the Lorentz model is not suitable to treat materials containing free charge carriers, like metals and semiconductors. The spring like force is not present because, in metals and semiconductors, electrons in the valency band can move freely. The Drude model address these problems by not including the restoring force into the electron equation of motion:

$$\frac{dp(t)}{dt} = -\frac{p(t)}{\tau} - eE(t) \qquad (2.8)$$

where $p(t)$ is the electron momentum and τ is the mean free time (the time interval which, in average, an electron picked at random will wait until its next collision). Assuming a steady-state solution of the form $p(t) = p(\omega)e^{-i\omega t}$ and $E(t) = E(\omega)e^{-i\omega t}$, one may find:

$$p(\omega) = -\frac{eE(\omega)}{\frac{1}{\tau} - i\omega}. \qquad (2.9)$$

Since the current density j in a metal can be written as, assuming time harmonic behavior, $j(\omega) = -nep(\omega)/m = \sigma(\omega)E(\omega)$, the AC conductivity $\sigma(\omega)$ can be defined as:

$$\sigma(\omega) = \frac{ne^2\tau}{1 - i\omega\tau}. \qquad (2.10)$$

The complex dielectric constant can be shown to be (ASHCROFT; MERMIN, 1976):

$$\epsilon(\omega) = 1 + \frac{i\sigma(\omega)}{\omega};\tag{2.11}$$

thus, the electric permittivity in the Drude model is:

$$\epsilon(\omega) = 1 - \frac{\omega_p^2}{\omega^2 + i\gamma\omega};\tag{2.12}$$

where we replaced the term containing the mean free time for an absorption coefficient γ, as it is more common in the literature; $\omega_p = \sqrt{ne^2/\epsilon_0 m}$ is the plasma frequency.

Together, the Drude and the Lorentz models are able to describe the electric response of matter. Both of them allow a negative response of the material, as one can see in figure 1(a). Physically, this means that the electric polarization of the medium and the polarization of the external field have opposite signs. Here we have assumed that the material response would be due to free electrons only, but the magnetic permeability also has negative value when the material response is due to bound magnetic moments and the frequency is smaller than the plasmonic frequency.
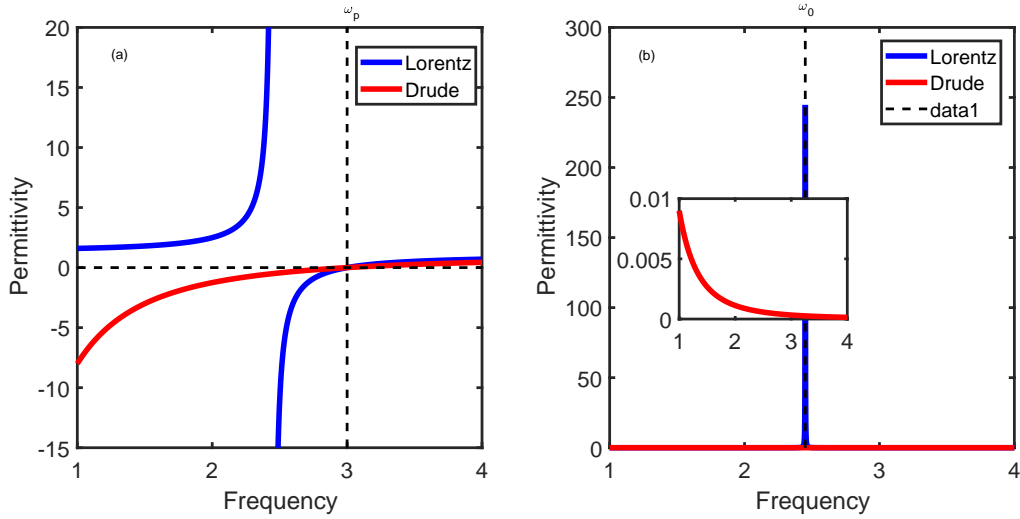
Figure 1 – (a) The real part of the electric permittivity for $\omega_p = 3$ and resonance frequency of $\omega_o = 2.45$ (for the Lorentz model only) (in arbitrary units). The dashed lines corresponds to the plasmonic frequency and to the zero value of the permittivity. Both models exhibit negative response. (b) The imaginary part of the electric permittivity. The inset shows the Drude model in detail, as its goes to 0 very fast.

The negative behavior of the permittivity is actually very common. Most metals (gold, silver and aluminum, for example) (PENDRY; SMITH, 2005) have a negative permittivity for frequencies around $400 - 790$ THz, i.e., in the visible range and near the ultraviolet. A problem arises when dealing with lower frequencies, from the infrared

downwards. In this limit the dissipation is very large, making the permittivity function practically imaginary (as one can easily see from fig. 1(b)). Negative permeability, on the other hand, exists for some ferromagnetic and antiferromagnetic systems (PIMENOV et al., 2005) in the microwave and far infrared region. Furthermore, the range of frequency that a material exhibits negative response is normally very narrow, making naturally occurring materials with simultaneous negative values for both permeability and permittivity very hard to find.

2.2.1 Plasmas
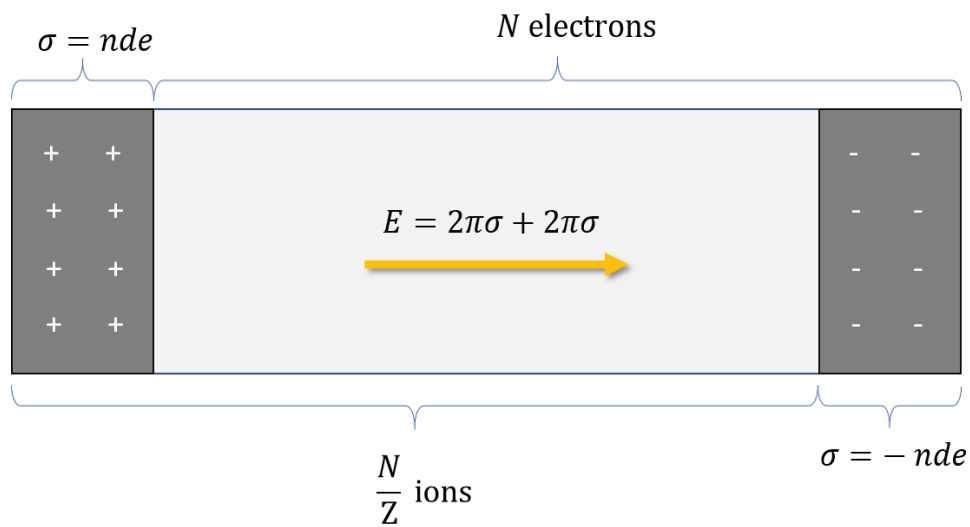
Figure 2 – Simple model of a plasma oscillation. An electron gas displaced in respect to a background ionic lattice. This generates a surface area, that creates an electromagnetic field of magnitude $4\pi\sigma$. This leads to an oscillation of the electron gas at the plasma frequency.

Plasmas is an old topic in physics started by Langmuir in the 1920s. They are are the object of study of lots of fields, as for example: radio broadcasting, which led to the discovery of the ionosphere, explaining why radio waves were reflected back to Earth; magnetohydrodynamics, which treats plasma as a conducting fluid, and is used in astrophysics and geophysics; laser plasma physics; high energy physics (aiming to use plasma acceleration to reduce the size of particle accelerators). Furthermore, surface plasma is often found when dealing with negative index materials. As one can see, this subject is very big and very important. In this thesis, we show that, when treating the propagation of light though one-dimensional lattices containing plasmonic materials, the light excites a bulk plasmon in the lattice. The excited plasmonic mode excited is very important, as it is responsible for the creation of a region where the light propagation is forbidden (a photonic band gap, the plasmon-polariton gap) and considerably effects how to zero-$< n >$ gap behaves.

Plasma oscillations can be seemed as collective oscillations of the electron density. The fluctuations in the electron density can be split into two parts: one related to the thermal motion of each electron, which shows no collective behavior; other related to the organized oscillation of the whole system, the plasma oscillation. Normally studied in dense electron gases, these oscillations are also common in metals and semiconductors. The quanta of this oscillation are known as plasmons (KITTEL, 2005).

A very simple and crude model can be built to explain plasma oscillations(ASHCROFT; MERMIN, 1976). Imagine an electron gas being displaced a distance d with respect to a fixed positive background of ions (as in fig. 2). The result surface charge density creates a field inside the material that will make the electron gas oscillate between the charged surfaces. The solution of the motion of the electron gas is a function that oscillates exactly at the plasma frequency. The dispersion of such wave, a plasma wave, is $\omega(k) = \omega_p = const.$, ω being a constant independent of the wave number k. Moreover, in a plasma, the wave number can assume any value while the frequency is fixed to the plasma frequency.

These oscillations present themselves mostly when treating materials with negative epsilon. For example, if one cuts a metal wire in half, the two surfaces created will show surface plasmons: oscillations restrained to the surface of the metal whose frequency obeys:

$$\epsilon_1(\omega_s) + \epsilon_2(\omega_s) = 0; \tag{2.13}$$

where ϵ_1 is the permittivity of the metal and ϵ_2 is the permittivity of the surrounding medium. If we choose vacuum and a metal with Drude response one may find that the surface plasmon will have frequency $\omega_s = \omega_p/\sqrt{2}$. If one changes the surface to another shape a variety of other plasmonic surface modes appear.

Another example of plasma oscillation presents itself in the case of a medium where the magnetic permeability is given by a Drude like response. Consider an electromagnetic wave of the form $e^{i(\omega t - \mathbf{k} \cdot \mathbf{r})}$. Such magnetic wave, when travelling through a magnetizable medium, induces a magnetization that modifies the wave, coupling the electromagnetic wave with the medium. This is a hybrid mode, as it is the result of the interaction of the electromagnetic wave with the medium (the electromagnetic wave excites a plasmonic mode inside the medium that strongly interacts with the light beam). The dispersion relation of such wave can be obtained by noting that its wave number satisfies $k = \omega/c\sqrt{\mu\epsilon}$. Thus, its dispersion relation is found to be $\omega^2 k_0^2 = \omega k^2 + \omega_p k_0^2$, where ω_p is the plasma frequency. In fig. 3 one can see the dispersion curve of the bulk plasmon polariton. It shows that there is no longer a pure plasma wave, or a pure electromagnetic wave, the dispersion relation is a mix of the two. The strong interaction of the plasma wave with the light results in the bulk plasmon polariton. As one can easily see, when k tends to ∞ the bulk plasmon polariton has a light-like behavior, and as k gets smaller the line moves away from the light dispersion relation and reaches the cut-off plasma frequency.
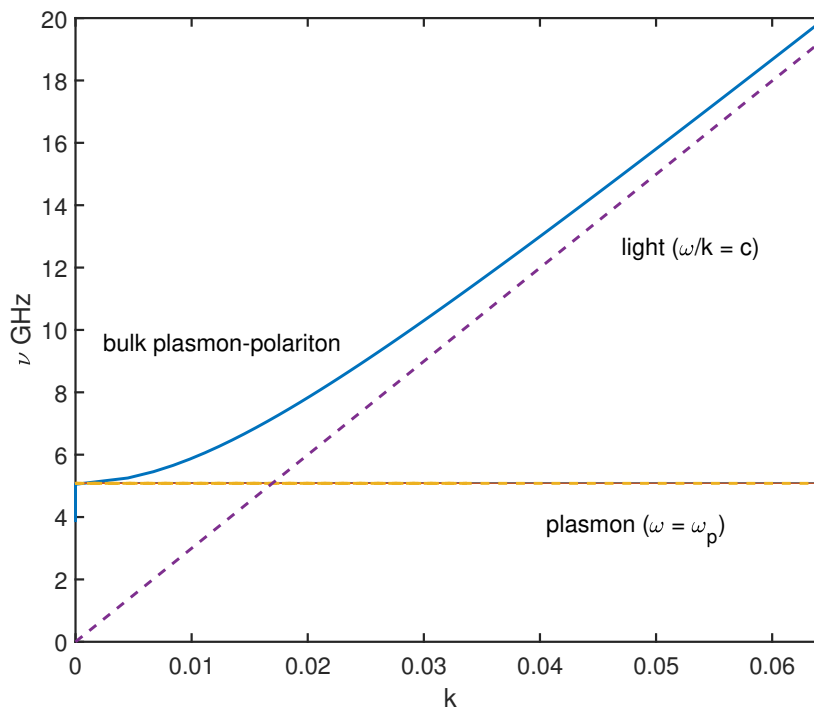
Figure 3 – The dispersion of a bulk plasmon-polariton is plotted in blue. The plasmon-polariton is a hybrid mode that stems from the coupling of the light beam (purple dashed line) with the plasmonic oscillation of the medium (orange dashed line).

2.3 Double negative materials
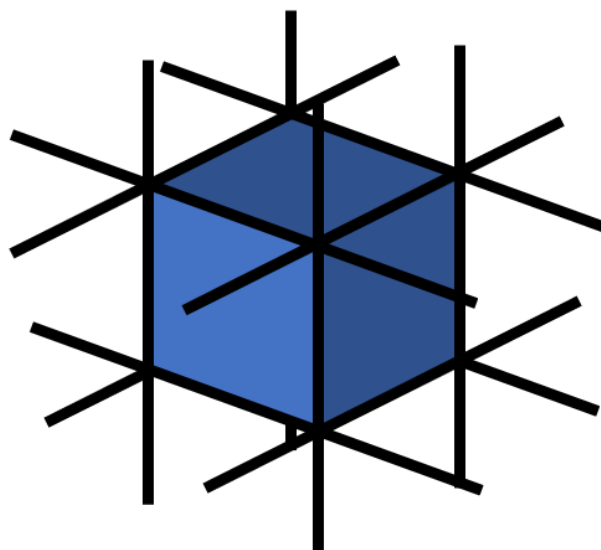
Figure 4 – Pictorial view of the material proposed by Pendry et al. in order to achieve negative electric permittivity. The material is a cubic lattice composed of nonmagnetic infinite wires (black lines). The unit cell of the material is in blue.

In 1968 Veselago published a paper where he suggested a hypothetical material

where both electric permittivity and magnetic permeability were simultaneously negative. He called the material a left-hand material as the wave vector, electric field and magnetic field makes a left-hand set in these materials. In studying this hypothetical material, he found a variety of new phenomena like the reversal of both the Doppler shift and Cherenkov radiation and anomalous refraction, all arising due to the reversal of the group velocity in the left-handed materials. Veselago's work remained in the hypothetical world for more than thirty years, when a material with both μ and ϵ negative was discovered in the 2000's by Smith et al. (SHELBY; SMITH; SCHULTZ, 2001; SHELBY et al., 2001; SMITH et al., 2000).
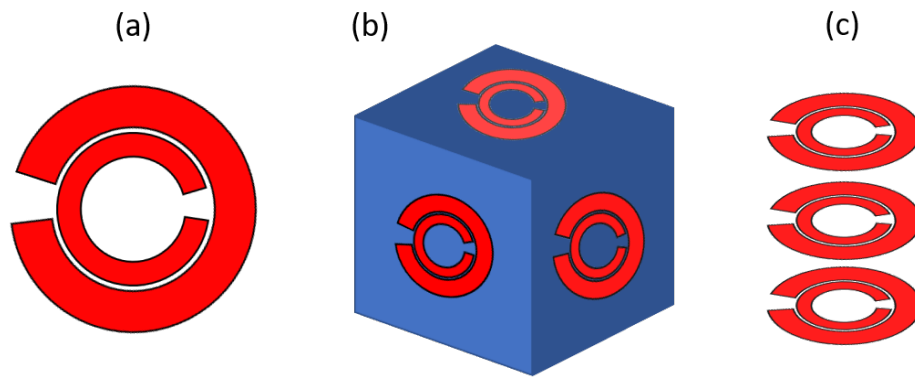
Figure 5 – Pictorial view of the material proposed by Pendry et al. in order to achieve negative magnetic permeability. The structure showed in (a) is called Split Ring Resonator (SRR), two concentric rings with smalls splits on them, placed with a very small distance from each other. (b) An array of SRR mimicking the behavior of a cylinder. Such structure would have an anisotropic behavior. (c) Unit cell of an isotropic material which exhibits negative permeability.

Up until Smiths work in the 2000's, it was known that a material consisting of metallic rods could produce negative ϵ, as demonstrated by Pendry et al. (PENDRY et al., 1996). To achieve such feat, it was proposed a periodic structure (fig. 4) composed of infinite very thin wires, with low magnetic response, arranged in a cubic lattice. The large self-inductance of the structure increases the electron momentum, mimicking the effect of a larger electron mass. Together with the much smaller electron density, due to the new packing, this greater effective mass is able to lower the plasmonic frequency considerably. This was quite an accomplishment as we can theoretically construct the wires of aluminum and end up with a plasmonic frequency of approximately 8.2 GHz, with practically no losses, in contrary to the naturally occurring epsilon negative materials (ENG) which have the plasmonic frequency in the THz range and losses so big that the material becomes unsuited for most of its applications. This structure was fabricated and experiments found it to have the predicted behavior, as it was shown latter by Pendry (PENDRY et al., 1998).

In a similar fashion, Pendry (PENDRY et al., 1999) designed a split ring resonator

(SRR), fig. 5, specifically to achieve negative permeability in a isotropic material. As a first try the article uses array of cylinders, but ends up with a highly anisotropic structure. To solve this problem the SRR is suggested 5(a). If one stacks the SRR only in the z direction, as in fig. 5(b), the response would still be the same as the cylinders. But if one stacks the SRR in a unit cell as in fig. 5(c), the response is isotropic. In short, the SRR act like a magnetic dipole, with a resonant response resulting from internal inductance and capacitance. Its magnetic response obeys a Lorentz type material, thus, near the resonance frequency the SRR produces a field that is opposite to the incident magnetic field. For copper the predicted resonance frequency is around 14 GHz. The SRRs are almost essential to the existence of negative permeability, being the basis of most metamaterials with such characteristic.

2.4 Plasmonic metamaterials
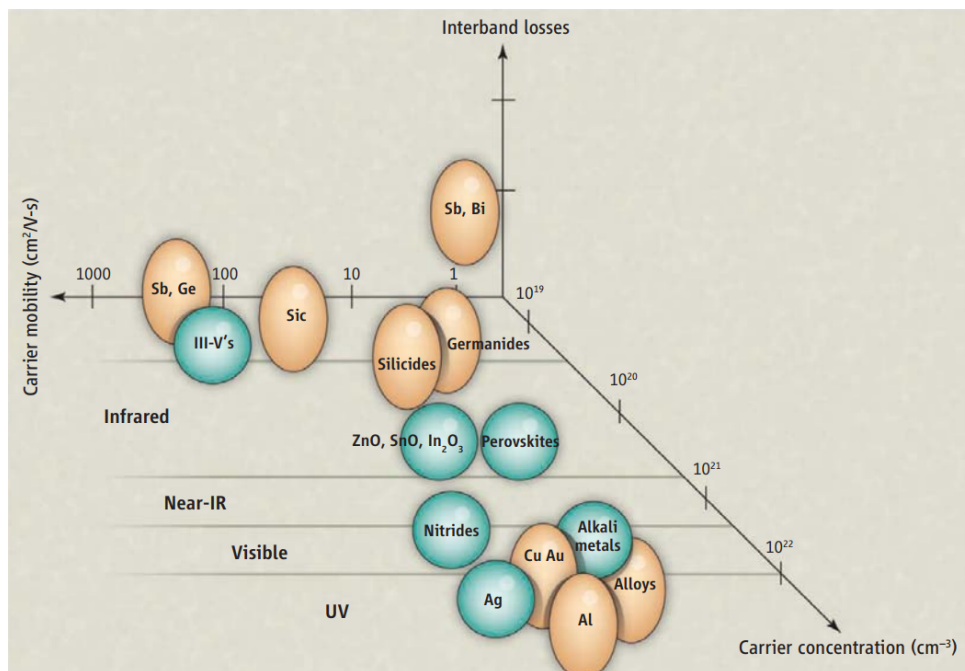
Figure 6 – Pictorial view of the classification of some materials in respect to their interband losses, carrier concentration and mobility. As the goal is to achieve negative permittivity with losses as small as possible one wants materials in the far right of the horizontal axis, i.e., high carrier mobility, zero interband losses and small carrier concentration. Source: (BOLTASSEVA; ATWATER, 2011)

When plasmonics and metamaterials are combined we can exploit problems in photonics where the features of photonics and electronics are mixed. In this case, the photon interacts with an excited plasmon in the medium, giving rise to propagating surface and bulk waves or localized excitations, depending on the problem. Plasmon-polaritons (the mixed mode arising from the interaction of the plasmonic modes with light) are normally

studied in materials formed of copper, silver, or gold because their plasmon frequency lies near the visible region. Furthermore, small noble metal particles, whose size is in the nanometers, also support localized plasmons, enables the interaction of plasma waves with light even in the nanoscale (LAL; LINK; HALAS, 2007). However, the integration of these particles to plasmonic materials and devices is still an open, and hot, topic.

Plasmonic metamaterials are still doomed by high losses, damping the plasmon-polariton oscillations. A workaround to this problem is to combine the plasmonic metamaterial with a gain medium, balancing the metallic losses. Xiao et al. (XIAO et al., 2010b) were able to create a metamaterial with a negative index of refraction of −1.017 in the visible wavelength range of 722 to 738 nm. Nonetheless, when approaching zero response (near zero values for permittivity or permeability) not even the gain from the highest gain materials are enough to balance the losses. An alternate approach to circumvent the problem of high losses is to investigate other elements to dope existing metallic structures (WEST et al., 2010). Moreover, a closer look to what makes a material a good candidate to build a plasmonic material is necessary. For this, the main properties we are looking for are: carrier mobility, carrier concentration and interband losses. To achieve negative permittivity one wants: the carrier concentration to be tunable and high; the carrier mobility to be high to offset losses; and the interband transitions to be as small as possible, as high interband transitions greatly increases the losses (KHURGIN; SUN, 2010). Figure 6 shows a materials map using this three categories (figure taken from (BOLTASSEVA; ATWATER, 2011)). These 'new' materials may enable new plasmonic materials with more interesting properties than low losses, providing a refreshing new take into the subject (BOLTASSEVA; ATWATER, 2011; KHURGIN; SUN, 2010).

2.4.1 Near zero refractive index structures

Another important characteristic that we are interested in (the first one being to find a metamaterial capable of achieving negative permeability and permittivity) is the actual realization of a zero-refractive index metamaterial. This has been a very hot topic in the literature, and continues to be a fertile field of research. Mostly three categories stems from near zero refractive index materials: metamaterials where the permittivity near zero (epsilon-near-zero (ENZ)); metamaterials where the permeability is near zero (mu-near-nezo (MNZ); and metamaterials where both the permittivity and the permeability are near zero (epsilon-and-mu-near-zero (EMNZ)). When any of these conditions is achieved the phase velocity v of the wave goes to infinity, recall that $v = 1/\sqrt{\epsilon\mu}$, making the wavelength approach very high values, effectively leading to small phase variation over large regions. Many interesting phenomena arises when dealing with these materials: supercoupling (SILVEIRINHA; ENGHETA, 2006; MARCOS; SILVEIRINHA; ENGHETA, 2015), the tunneling of a electromagnetic wave through a very narrow channel filled with ENZ or

MNZ metamaterial between two waveguides; and, as we shall see with more detail later, the opening of a non-Bragg gap around the frequency of ENZ or MNZ metamaterials, the plasmon-polariton gap (REYES-GÓMEZ et al., 2009).

These metamaterials are being designed and characterized experimentally in the last few years. Conducting oxides (indium-tin-oxide, aluminum-zinc-oxide and gallium-zinc-oxide (WEST et al., 2010)) have the real part of the permittivity approaching zero at telecommunications wavelength (1260 to 1675 nm). Eric Mazur et al. have been developing on-chip integrated metamaterials in the optical regime (LI et al., 2015), and recently (RESHEF et al., 2017) developed a waveguide with zero-crossing region around a wavelength of 1625 nm. A review of some advances in the experimental area can be found in (RAMAKRISHNA, 2005).

3 Linear optical lattices

The main goal of this chapter is to give the reader a brief overview on the subject of wave propagation in one-dimensional stratified medium composed of linear metamaterials. For that, a brief introduction of the theories involved must be given. The subject of wave propagation in linear layered media is extensively treated on the literature and the focus of some books (YEH, 2005; BORN; WOLF, 2013; SOLYMAR; SHAMONINA, 2009). Moreover, the contents of this chapter aims to make this work entirely reproducible by itself and to give a general overview of the topic. A detailed explanation of all the concepts treated here can be easily found in the literature and a more curious reader is encouraged to pursue it if he, or she, needs a more detailed approach.

3.1 Maxwell Equations

As a first remark we start stating that, throughout this thesis, we will work with the interaction of electromagnetic radiation with matter within a macroscopic framework, i.e., the spatial variation of the electromagnetic field is way larger than the size of the constituents of the material of interest. Under these assumptions, we may study the solutions of Maxwell's equations (in SI units):

$$\boldsymbol{\nabla} \cdot \mathbf{B} = 0, \tag{3.1}$$

$$\boldsymbol{\nabla} \cdot \mathbf{D} = 0, \tag{3.2}$$

$$\boldsymbol{\nabla} \times \mathbf{E} + \frac{\partial \mathbf{B}}{\partial t} = 0, \tag{3.3}$$

$$\boldsymbol{\nabla} \times \mathbf{H} - \frac{\partial \mathbf{D}}{\partial t} = 0; \tag{3.4}$$

where it was assumed that no sources are present, so the electric charge density $\rho = 0$ and the electric current density $\mathbf{J} = 0$.

3.2 Constitutive equations

To proceed, and to allow a unique determination of the field vectors, a set of constitutive relations must be given to describe the influence of the fields on the behavior of the media they propagate. Mathematically, one can show that there are only three independent equations in the Maxwell's equations, a number smaller than the number of unknowns, and thus, they are in an *indefinite* form. To obtain a *definite* set of equations, one must provide constitutive relations between the field quantities. In this thesis, it will

only be considered materials where (JACKSON, 1999):

$$\mathbf{D} = \epsilon_0 \mathbf{E} + \mathbf{P} \tag{3.5}$$

$$\mathbf{H} = \frac{1}{\mu_0} \mathbf{B} + \mathbf{M} \tag{3.6}$$

where ϵ_0 and μ_0 are the electric permittivity and magnetic permeability of the vacuum; $\mathbf{P}$ and $\mathbf{M}$ are the polarization and magnetization, respectively. The analysis presented from here on out will be restrained to the cases where the magnetization is related linearly to the magnetic field. This assumption holds true for isotropic diamagnetic and paramagnetic substances, and can be achieved by a relation of the form $\mathbf{B} = \mu_0 \mu \mathbf{H}$, where μ is the magnetic permeability of the material, and can be a function of the frequency.

For the electric part, it is customary to expand the polarization as a power series in the electric field (MILLS, 1998). This can be done because the fields of interest (applied to the substances) are small compared to the electric fields experienced by the electrons in the material, i.e., fields encountered in laboratories are of the order of 10^6 V/cm while the fields experienced by electrons due to the atoms or molecules are of the order of 10^9 V/cm. For a dispersionless and lossless system, with instantaneous response, one can obtain the polarization $P(t)$ as a power series in the field strength $E(t)$:

$$P(t) = \epsilon_0 \left[\chi^{(1)} E(t) + \chi^{(2)} E^2(t) + \chi^{(3)} E^3(t) + \cdots \right]. \tag{3.7}$$

When the field strength is small the linear relation $P(t) = \epsilon_0 \chi^{(1)} E(t)$, where $\chi^{(1)}$ is known as the linear susceptibility, is recovered. The term $\epsilon_0 \chi^{(2)} E^2(t)$ is often referred as the second-order nonlinear polarization $P^{(2)}(t)$ and $\epsilon_0 \chi^{(3)} E^3(t)$ as the third-order nonlinear polarization $P^{(3)}(t)$. In this expansion the Polarization $P(t)$ and the field strength $E(t)$ were treated as scalar quantities for simplicity. This is actually not true, and both $\chi^{(3)}$ and $\chi^{(2)}$ are n-rank tensor quantities, but treating the polarization, electric field and susceptibilities as scalar quantities is a valid approximation because of the nature of the problem it will be treated: the propagation of an electromagnetic wave in a one dimensional lattice.

A specific model is needed to obtain a more detailed understanding of both μ and $\chi^{(n)}$. The previous chapter gave us an overview of the different theories and which materials they describe. The Lorentz and Drude models are suitable to describe most of the metamaterials of interest, and will be the ones used in this thesis. With this in mind, we are able to determine both $\mathbf{D}$ and $\mathbf{H}$ and continue with the analysis of the Maxwell equations. Some calculations will be made in order to simplify the Maxwell equations for an one-dimensional layered system composed of alternate layers of dispersive metamaterials.

3.3   Maxwell equations for one-dimensional supperlattices

Assume time harmonic $e^{-i\omega t}$ dependence, from which an arbitrary solution by Fourier superposition can be built. Using $\mathbf{D}(\mathbf{r}, t) = \mathbf{D}(\mathbf{r})e^{-i\omega t}$ and $\mathbf{H}(\mathbf{r}, t) = \mathbf{H}(\mathbf{r})e^{-i\omega t}$ on the Maxwell's equations, one can obtain:

$$\boldsymbol{\nabla} \cdot \mathbf{B} = 0, \tag{3.8}$$

$$\boldsymbol{\nabla} \cdot \mathbf{D} = 0, \tag{3.9}$$

$$\boldsymbol{\nabla} \times \mathbf{E} - i\omega \mathbf{B} = 0, \tag{3.10}$$

$$\boldsymbol{\nabla} \times \mathbf{H} + i\omega \mathbf{D} = 0. \tag{3.11}$$

Using linear relations for both the electric displacement $\mathbf{D}$ and magnetic field $\mathbf{B}$, eqs. 3.1:3.4 can be written as:

$$\boldsymbol{\nabla} \cdot \mathbf{H} = 0, \tag{3.12}$$

$$\boldsymbol{\nabla} \cdot \mathbf{E} = 0, \tag{3.13}$$

$$\boldsymbol{\nabla} \times \mathbf{E} - i\omega \mu_0 \mu \mathbf{H}, = 0 \tag{3.14}$$

$$\boldsymbol{\nabla} \times \mathbf{H} + i\omega \epsilon_0 \epsilon \mathbf{E} = 0. \tag{3.15}$$

When studying reflected and transmitted waves on layered media one can show that every problem can be decomposed into two independent problems (BORN; WOLF, 2013), one where all components of the electric field are perpendicular to the plane of incidence, and one where all the components of the magnetic field are perpendicular to the plane of incidence. To the first kind of problem we shall refer as transverse E (TE) and to the latter transverse H (TM). Despite being independent, both problems are remarkably similar, to the point where just a simple swap in the electric permittivity and magnetic permeability is enough to find the reflection and transmission coefficients (to be defined latter) of both TE and TM configurations (BORN; WOLF, 2013). From here on out only the problem of a TE configuration will be treated as the differences between TE and TM configurations, from a mathematical viewpoint, are minor.

For a TE wave, in a configuration where the yz plane is the plane of incidence, z being the direction of stratification (fig. 3.3), $E_y = E_z = 0$, and $H_x = 0$. These

simplifications, when applied to the Maxwell equations, lead to:

$$\frac{\partial E_x}{\partial z} - i\omega\mu_0\mu H_y = 0, \tag{3.16}$$

$$\frac{\partial E_x}{\partial y} + i\omega\mu_0\mu H_z = 0, \tag{3.17}$$

$$\frac{\partial H_z}{\partial y} - \frac{\partial H_y}{\partial z} + i\omega\epsilon_0\epsilon E_x = 0, \tag{3.18}$$

$$\frac{\partial H_z}{\partial x} = 0, \tag{3.19}$$

$$\frac{\partial H_y}{\partial x} = 0. \tag{3.20}$$
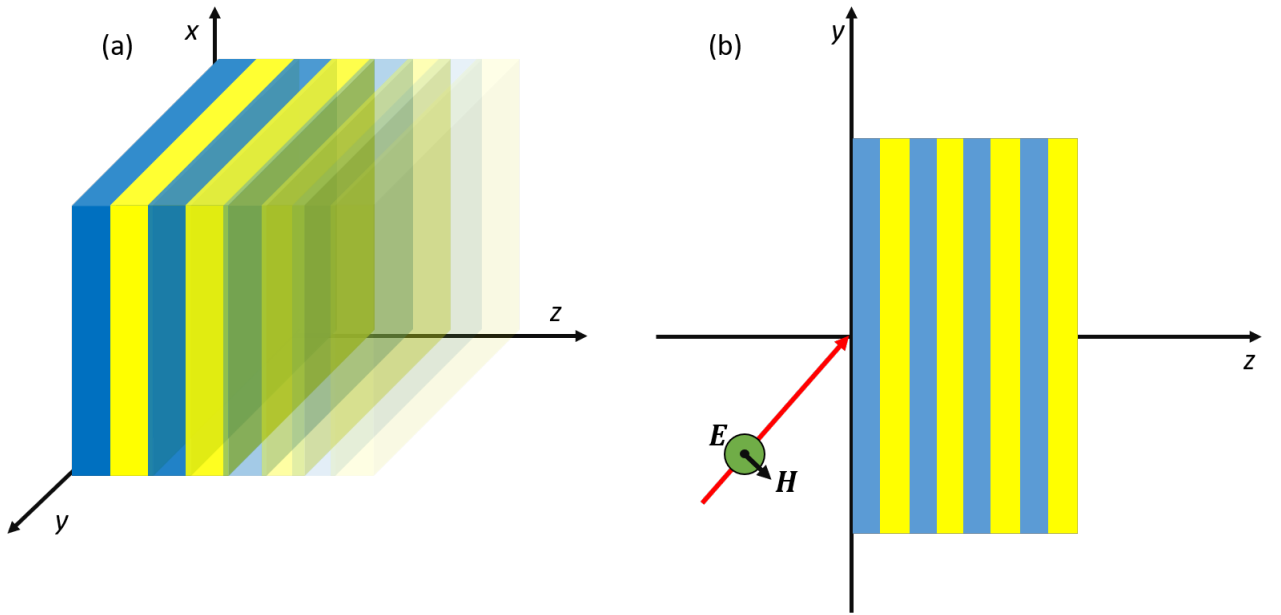
Figure 7 – Pictorial view of the configuration this thesis is dealing with. In (a) we show a three-dimensional view of the system, as an example of a periodic heterostructure composed of two types of materials (in blue and in yellow) was chosen. We have assumed that a TE wave is inciding upon a heterostructure with the z direction as the direction of the stratification, and the plane of incidence is the yz plane (figure (b)).

As the partial derivatives of H_y, H_z (eqs. 3.19,3.20) in relation to x are both 0, they are only functions of y and z, and as E_x is proportional to a function of y and z only (eq. 3.18), the same is valid for it. By differentiating 3.16 in relation to x and 3.17 in relation to y and replacing both in 3.18, we can eliminate both H_z and H_y:

$$\frac{\partial^2 E_x}{\partial y^2} + \frac{\partial^2 E_x}{\partial z^2} + \frac{\omega^2}{c^2}\epsilon\mu E_x = \frac{d\log\mu}{dz}\frac{\partial E_x}{\partial z}; \tag{3.21}$$

where ϵ and μ are functions of z, as shown in fig. 3.3. The solution of this equation can be found using the method of separation of variables. The product of two functions

$E_x(y, z) = Y(y)U(z)$, $Y(y)$ being a function of y only and $U(z)$ a function of z only, can be used as trial solution. Thus:

$$\frac{1}{Y}\frac{\partial^2 Y}{\partial y^2} = -\frac{1}{U}\frac{\partial^2 U}{\partial z^2} - \frac{\omega^2}{c^2}\epsilon\mu + \frac{d\log\mu}{dz}\frac{1}{U}\frac{\partial U}{\partial z}. \tag{3.22}$$

The term on the left depends only on y and the term on the right only on z. Hence the above equation can hold only if each side is equal to a constant (let's call it $-K^2$):

$$\frac{\partial^2 Y}{\partial y^2} = -K^2 Y; \tag{3.23}$$

$$\frac{\partial^2 U}{\partial z^2} - \frac{d\log\mu}{dz}\frac{\partial U}{\partial z} + \frac{\omega^2}{c^2}\epsilon\mu U = K^2 U. \tag{3.24}$$

Eq. 3.23 gives $Y(y) = const.e^{iKy}$, and consequently E_x is of the form:

$$E_x(y, z) = E_x(z)e^{iKy} \tag{3.25}$$

where $E_x(z) = const.U(z)$. For clarity, let's rewrite here the Maxwell equations for H_y, H_z and E_x:

$$\frac{\partial E_x}{\partial z} - i\omega\mu_0\mu H_y = 0; \tag{3.26}$$

$$\frac{\partial E_x}{\partial y} + i\omega\mu_0\mu H_z = 0; \tag{3.27}$$

$$\frac{\partial H_z}{\partial y} - \frac{\partial H_y}{\partial z} + i\omega\epsilon_0\epsilon E_x = 0. \tag{3.28}$$

From the above equations one can see that $H_y(y, z)$ and $H_z(y, z)$ are given by expressions of the same form:

$$H_y(y, z) = H_y(z)e^{iKy}; \tag{3.29}$$

$$H_z(y, z) = H_z(z)e^{iKy}. \tag{3.30}$$

By replacing the above equations into the Maxwell equations, one can obtain:

$$\frac{dH_y(z)}{dz} = iKH_z(z) + i\omega\epsilon_0\epsilon E_x(z), \tag{3.31}$$

$$\omega\mu_0\mu H_z(z) + KE_x(z) = 0, \tag{3.32}$$

$$\frac{dE_x(z)}{dz} = i\omega\mu_0\mu H_y(z). \tag{3.33}$$

Eliminating $H_z(z)$ from the equations above, we have a pair of simultaneous first-order differential equations for $E_x(z)$ and $H_y(z)$:

$$\frac{dE_x(z)}{dz} = i\omega\mu_0\mu H_y(z), \tag{3.34}$$

$$\frac{dH_y(z)}{dz} = \left(i\omega\epsilon_0\epsilon - \frac{iK^2}{\omega\mu_0\mu}\right)E_x(z).; \tag{3.35}$$

or, by replacing eq. 3.34 into 3.35, we find a differential equation for $E_x(z)$:

$$\frac{\partial^2 E_x(z)}{\partial z^2} + \frac{\omega^2}{c^2}\epsilon\mu E_x(z) = K^2 E_x(z). \tag{3.36}$$

This equation uniquely determines the problem of a wave propagating in a one-dimensional slab, being the slab any linear material (dispersive, metamaterial, etc...).

3.3.1   Generalized Snell's Law

To solve equation 3.36 we still need to determine its boundaries conditions and a way to determine K. The constant K can be determined by looking at eq. 3.23. This equation clearly shows that K is equal to the component of the wave vector of the incident plane wave in the y direction. Moreover, all the assumptions made up until now about the incident field can be resumed in the following statement:

$$\mathbf{E}(x, y, z, t) = E_x(z)e^{(ik_0\beta y - i\omega t)}\hat{\boldsymbol{x}}, \tag{3.37}$$

i.e., we are restricting the discussion to monochromatic TE-polarized fields. Despite the correct determination of K being already known, an important generalization of a fairly known law can be obtained with a little math.

The surfaces with constant phase of a plane wave, eq. 3.37, are:

$$F(z, y) = \phi(z) + Ky = constant; \tag{3.38}$$

where $\phi(z)$ is the phase of $E_x(z)$. The normal to this plane is given by the gradient of $F(z, y)$, i.e., $n = \frac{\partial \phi}{\partial z}\hat{\boldsymbol{z}} + K\hat{\boldsymbol{y}}$. Let θ be the angle that this normal makes with OZ, then:

$$\tan\theta = \frac{K}{\frac{\partial \phi}{\partial z}} \tag{3.39}$$

For a plane wave we have that $\phi = k_0 nz\cos\theta$, where $k_0 = \frac{\omega}{c}$, c is the light's speed in vacuum and ω is the frequency of the plane wave. This leads to $K = k_0 n\sin\theta$. As K is a constant, one can find that $\beta = n\sin\theta$ is also constant in every slab of a supperlattice, regardless of μ and ϵ. Hence the relation $K = const.$ may be regarded as a generalization of Snell's law of refraction to stratified media.

3.3.2   Normalized wave equation for one-dimensional supperlattices

Replacing $K = k_0 n\sin\theta$ into eq. 3.36 we have:

$$\frac{\partial^2 E_x(z)}{\partial z^2} + k_0^2 \left(\epsilon\mu - \epsilon\mu\sin^2\theta\right) E_x(z) = 0 \tag{3.40}$$

By introducing a dimensionless position ($\zeta = k_0 z$), the equation for the amplitude of the electric field may be rewritten as:

$$\frac{d^2}{d\zeta^2}E_x + (\epsilon\mu - \beta^2)E_x = 0; \tag{3.41}$$

this is the equation that will be used to model our problems. With it we can determine H_y and H_z and have a complete description of the electromagnetic phenomena inside the material (be it a metamaterial or a nonlinear Kerr material).

3.4   Transfer matrix

Equation 3.41 can be easily solved if no nonlinearities are present. The method normally used to solve this equation in the linear regime is the transfer matrix formulation (YEH, 2005). The deduction of the method will not be shown here, but if one has the values of both E_x and H_y at one interface (let's say at $z = 0$), the transfer matrix method allows you to find the values of E_x and H_y at any point of the slab by using:

$$\begin{pmatrix} E_x(z) \\ c\mu_0 H_y(z) \end{pmatrix} = \begin{pmatrix} \cos qz & \frac{i}{p}\sin qz \\ ip\sin qz & \cos qz \end{pmatrix} \begin{pmatrix} E_x(0) \\ c\mu_0 H_y(0) \end{pmatrix}$$

where $p = \frac{qc}{\omega\mu}$ and $q = \frac{\omega}{c}\sqrt{\epsilon\mu - \beta^2}$. The matrix

$$\mathbf{M}(z) = \begin{pmatrix} \cos qz & \frac{i}{p}\sin qz \\ ip\sin qz & \cos qz \end{pmatrix}$$

is called the transfer matrix. This procedure can be applied to find the field for multiple layers by multiplicating the matrix of each layer. For example, let's consider a stratified media composed of two adjacent slabs, the first one extending from $z = 0$ to $z = z_1$ and the second from $z = z_1$ to $z = z_2$. If $\mathbf{M}_1$ and $\mathbf{M}_2$ are the transfer matrix of the two media, respectively, then:

$$\begin{pmatrix} E_x(z_2) \\ c\mu_0 H_y(z_2) \end{pmatrix} = \mathbf{M}_2(z_2 - z_1)\mathbf{M}_1(z_1) \begin{pmatrix} E_x(0) \\ c\mu_0 H_y(0) \end{pmatrix}.$$

The transfer matrix formalism can also be used to find the dispersion relation of an infinite lattice composed of only linear materials (this is analogous to the Kronig-Penney model in quantum mechanics) . This will be quite useful because we can compare the results of a finite lattice with its infinite counterpart. The dispersion relation for an infinite lattice composed of two different materials, A and B, with widths a and b, magnetic permeability $\mu_{A,B}$ and electric permittivity $\epsilon_{A,B}$ for layers A, B, can be written as:

$$\cos(Sd) = \cos\left(q_A a\right)\cos\left(q_B b\right) - \frac{1}{2}\left(\frac{p_B}{p_A} + \frac{p_A}{p_B}\right)\sin\left(q_A a\right)\sin\left(q_B b\right) \tag{3.42}$$

where S is the Bloch wave vector along the z direction, $q_{A,B} = \frac{\omega}{c}\sqrt{\epsilon_{A,B}\mu_{A,B} - \beta^2}$ and $p_{A,B} = \frac{q_{A,B}c}{\omega\mu_{A,B}}$. The details of the algebra to find the dispersion relation of an infinite lattice composed of two linear metameterials can be find in appendix A.

3.5   Reflectance and Transmittance
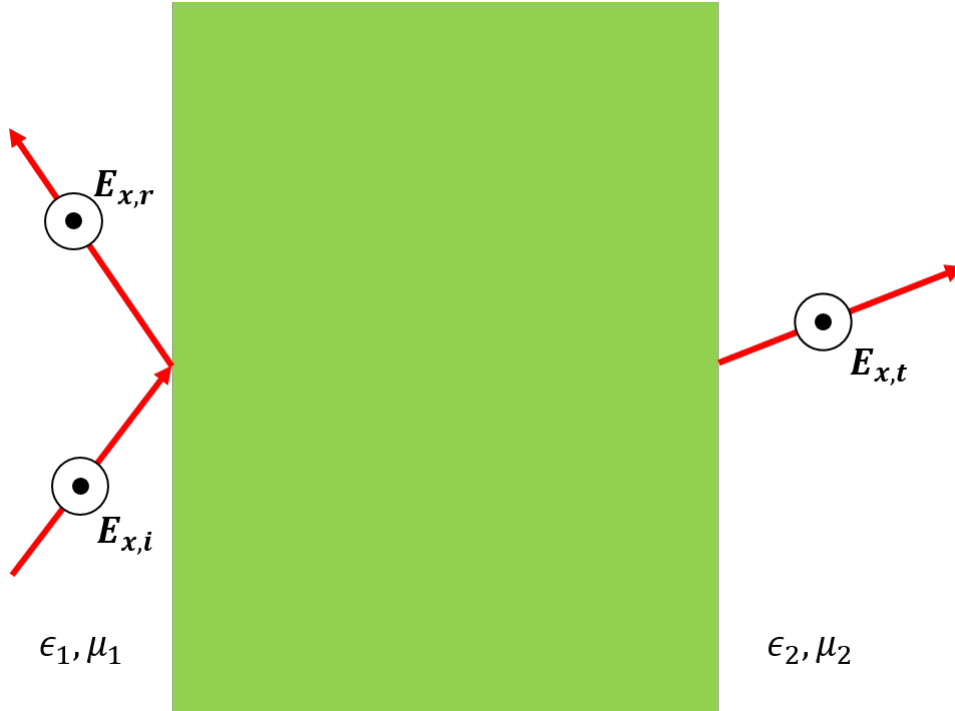
Figure 8 – View of the plane of incidence of a TE-wave upon an one-dimensional heterostructure (depicted in green) sandwiched between media with electric permittivity ϵ_1, ϵ_2 and magnetic permeability μ_1, μ_2 in the left and right, respectively; $E_{x,i}$ is the amplitude of the incident field, $E_{x,r}$ is the amplitude of the reflected field and $E_{x,t}$ is the amplitude of the transmitted field.

When treating the problem of wave propagation in one-dimensional lattices one usually wants to know, besides the field profile inside the structure, how much of the incident wave was reflected and how much was transmitted through the lattice. To find out how much of the incident wave energy is reflected from the boundary and transmitted to the second medium, the ratios of the Poynting power flow of the reflected and the transmitted waves to that of the incident wave must be considered. Again, the problem being the propagation of waves in a one-dimensional lattice allows a very good simplification: the power flow parallel to the boundary surface does not change through the lattice. Therefore, only the normal component of the time averaged Poynting's vector needs to be considered when the transmission and reflection are being calculated. Thus, reflectance and transmittance can be defined as:

$$R = \left| \frac{\hat{\boldsymbol{z}} \cdot \mathbf{S}_r}{\hat{\boldsymbol{z}} \cdot \mathbf{S}_i} , \right|, \tag{3.43}$$

$$T = \left| \frac{\hat{\boldsymbol{z}} \cdot \mathbf{S}_t}{\hat{\boldsymbol{z}} \cdot \mathbf{S}_i} \right|, \tag{3.44}$$

where the time averaged Poynting's vector is:

$$\mathbf{S} = \frac{1}{2}\mathbf{E} \times \mathbf{H}^*. \tag{3.45}$$

For the problem proposed (a one-dimensional lattice, as show in fig. 3.5):

$$\mathbf{S}_i = \frac{1}{2}\frac{\sqrt{\epsilon_1}}{\sqrt{\mu_1}}\left|E_{x,i}\right|^2 n_{z,1}\hat{\mathbf{z}} \tag{3.46}$$

$$\mathbf{S}_r = \frac{1}{2}\frac{\sqrt{\epsilon_1}}{\sqrt{\mu_1}}\left|E_{x,r}\right|^2 n_{z,1}\hat{\mathbf{z}} \tag{3.47}$$

$$\mathbf{S}_t = \frac{1}{2}\frac{\sqrt{\epsilon_2}}{\sqrt{\mu_2}}\left|E_{x,t}\right|^2 n_{z,2}\hat{\mathbf{z}} \tag{3.48}$$

where $n_{z,1}$ and $n_{z,2}$ are the z components of the normalized wave vector $\mathbf{k}$ in the first medium and in the medium immediately after the last slab, respectively; ϵ_1 and μ_1 are the electric permittivity and magnetic permeability in the first medium; ϵ_2 and μ_2 are the electric permittivity and magnetic permeability in the last medium.

Moreover, the transmittance T and reflectivity R are given by:

$$R = \frac{\left|E_{x,r}\right|^2}{\left|E_{x,i}\right|^2}; \tag{3.49}$$

$$T = \frac{\sqrt{\epsilon_2}\sqrt{\mu_1}n_{z,2}}{\sqrt{\epsilon_1}\sqrt{\mu_2}n_{z,1}}\frac{\left|E_{x,t}\right|^2}{\left|E_{x,i}\right|^2}. \tag{3.50}$$

The formulas given here for the transmittance and reflectivity are general, and can be used independently of the nature of the material of the slabs, with the only constraint being that the medium that in which the lattice is embedded is linear. This is useful because these formulas are unaffected by the inclusion of nonlinear layers (independent of the kind of the nonlinearity).

3.6   Numerical calculations of the Incident and Transmitted fields

A procedure to solve eq. 3.41 has already been pointed out, the transfer matrix formalism. However, this method, while exact, can't solve the problem when a nonlinear material is present. As the main goal of this thesis is to simulate the wave propagation in supperlatticies composed of linear dispersive metamaterials and Kerr materials, a way to solve the eq. 3.41 that accounts for nonlinear terms is necessary. In order to do so, we resort to a Runge-Kutta integration scheme, specifically we use the Dormand-Prince pair formulas. This single-step solver uses a fifth and a fourth order Runge-Kutta (BUTCHER, 2016) integration scheme to create an adaptive algorithm. We will not describe in detail here this integration method, as a very detailed description of the algorithm is given in (DORMAND; PRINCE, 1980). The Dromand-Prince pair formulas are implemented in

MATLAB via the *ode45* function and in Fortran via the *DOPRI15* package. The results obtained here were made with our own implementation of the algorithm in C++ and in MATLAB.

3.6.1 Boundary Conditions

The mathematical equations presented up until now (eq. 3.41 in conjunction with the specific mathematical formulas for the permittivity and permeability for all the layers) are sufficient to solve the problem wave propagation in an electromagnetic media. To extend this formalism to a layered system one must use the boundary conditions at interfaces between different media derived from the Maxwell equations (JACKSON, 1999). The boundary conditions necessary for a one-dimensional layered system are simply the continuity of the tangential components of **E** and **H** across each interface. This means that we have to guarantee the continuity of E_x and $\frac{1}{\mu}\frac{\partial E_x}{\partial z}$ in every interface between two different materials.

3.6.2 Integration scheme for the supperlattice

The procedure outlined here for the numerical integration of Eq. 3.41 is an extension of the work of Trutschel and Lederer (TRUTSCHEL; LEDERER, 1988) and Peschel *et al.* (PESCHEL et al., 1988). While they numerically solve Eq. 3.41 for nonmagnetic media, we proceed by showing the calculations for materials where $\mu \neq 1$. Normally one would provide the algorithm with an incident field, integrate eq. 3.41 and find the transmitted and reflected fields. By integrating from the incident field to the transmitted field one would hinder bistability, as most of the unstable branches would not be shown by using this approach. Because of this, we choose to integrate the problem in a inverse way. We provide the fields at the slab were the transmitted field is measured, and integrate this value up to the media where the incident and transmitted fields are encountered. The integration we mention here is the use of the Dormant-Prince pair scheme to solve eq. 3.41.

Begin by choosing $E(k_0 L_i)$ and its derivative $\frac{d}{d\zeta}E(k_0 L_i)$, and integrating Eq. 3.41 using the Dormant-Prince integration formulas from $\zeta = k_0 L_i$ to $\zeta = k_0(L_i - d_i)$, where L_i is the position of the outer surface of the i-th layer. At the end of the integration we end up with $E(k_0(L_i - d_i))$ and $\frac{d}{d\zeta}E(k_0(L_i - d_i))$. The field in the remaining layers are integrated in a similar fashion, but the initial values E and $\frac{d}{d\zeta}E$, for each new integration, are now obtained by ensuring the continuity of both E and $\frac{1}{\mu}\frac{d}{d\zeta}E$ through each interface.

To obtain reflection and transmission coefficients, one needs to calculate the incident E_i, reflected E_r and transmitted E_t electric fields, which are obtained by the imposition of boundary conditions at the surfaces between the lattice and the embedded medium regions. The electric field for $\zeta < 0$ is formed by a superposition of the incident and the

reflected field whereas the electric field for $\zeta > k_0 L$ is given by the transmitted field:

$$E(\zeta) = \begin{cases} E_i e^{iQ_1\zeta} + E_r e^{-iQ_1\zeta} & \text{if } \zeta < 0 \\ E_t e^{iQ_2(\zeta - k_0 L)} & \text{if } \zeta > k_0 L \end{cases} \tag{3.51}$$

where $Q_i = \sqrt{\epsilon_j \mu_j - \beta^2}$, with $j = 1, 2$ if $\zeta < 0$ or $\zeta > k_0 L$ respectively. By assuring the continuity of both E and $\frac{1}{\mu}\frac{dE}{d\zeta}$ at $\zeta = k_0 L$, one may assign a value for the electric-field amplitude E_t in the outer interface and obtain the values of both $E(k_0 L) = E_t$ and $\frac{d}{d\zeta}E(k_0 L) = iQ\mu_B E_t/\mu_2$. Then, by integrating equation 3.41 for each internal layer, as described before, one may find $E(0)$ and $\frac{d}{d\zeta}E(0)$. By imposing the continuity of both E and $\frac{1}{\mu}\frac{dE}{d\zeta}$ in $\zeta = 0$ one may find the incident and reflected fields as a function of $E(0)$ and $\frac{dE(0)}{d\zeta}$,

$$E_i = \frac{1}{2}\left[E(0) - \frac{i\mu_1}{Q\mu_A}\frac{dE(0)}{d\zeta} \right] \tag{3.52}$$

$$E_r = \frac{1}{2}\left[E(0) + \frac{i\mu_1}{Q\mu_A}\frac{dE(0)}{d\zeta} \right] \tag{3.53}$$

Moreover, the transmittance T and reflectivity R are given by

$$T = \frac{\sqrt{\epsilon_2}\sqrt{\mu_1}n_{z,2}}{\sqrt{\epsilon_1}\sqrt{\mu_2}n_{z,1}}\left| \frac{E_t}{E_i} \right|^2 \tag{3.54}$$

$$R = \left| \frac{E_r}{E_i} \right|^2. \tag{3.55}$$

3.7 Photonic Crystals

The type of structure we have been talking about in this chapter, the superlattices, are very well known and have some properties that are encountered when studying the propagation of electrons in solids or crystals. While the propagation of electrons is governed by the Schroedinger's equation, photons obeys the Maxwell equations. Although different, when studying the propagation of light through periodic structures (with varying permittivity and permeability) one may cast the Maxwell's equations in a form very similar to the Schroedinger equation. Following this parallel, a periodic array of dielectrics can be described in terms of a band structure, as it is the case for electrons propagating in a Bravais lattice. Furthermore, the appearance of band gaps is also expected for the propagation of light beams, i.e., forbidden frequency bands in which light cannot propagation in any direction. Usually the structures studied are not isotropic, allowing one direction of propagation to reflect all incident light while other directions still transmit light.

An extensive review of naturally occurring photonic crystals, as an analysis of their band-gaps, was published by Simonis and Vigneron (VIGNERON; SIMONIS, 2012). They show that insects, spiders, birds, fishes, plants and some marine animals have some kind

of natural photonic crystal-type structure that is highly optimized. These structures can be used as inspiration to the fabrication of artificial photonic crystals. One of the first band gaps was observed by Yablonovitch (YABLONOVITCH, 1993) in a silicon crystal with tetrahedral geometry and millimetric holes drilled on it. New techniques are being continuously developed to build better photonic crystals (INOUE; OHTAKA, 2013).

3.7.1 Photonic Band Gaps

The band-gaps presented by photonic crystals can be divided into three categories: Bragg gaps, the zero-<n> gap and the plasmon-polariton gap. These gaps have different natures and react differently to varying parameters (lattice size, incidence angle, frequency).

3.7.1.1 Bragg gap
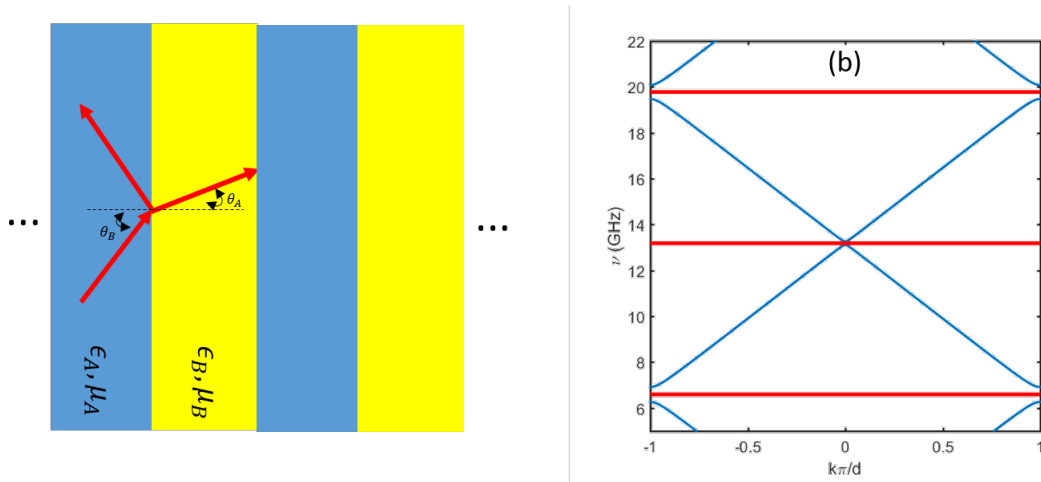
Figure 9 – (a) Pictorial view of the photonic crystal under consideration. The crystal is composed of unit cells consisting of layers A with refractive index $n_a = 1.4142$ and layers B with refractive index $n_b = 1.2649$. (b) Band diagram for the photonic crystal depicted in (a). The red lines are the frequencies where the theory predicts the opening of the Bragg gap (integer multiples of the 6.59 GHz frequency), and as one can see there is no intersection between the red and blue lines, meaning that there is no allowed states around the Bragg resonances given by eq. 3.56.

Bragg gaps are formed by interference of the reflected wave from different layers of the system, much like the Bragg reflections occurs in a metal (as explained earlier). When these reflections combine constructively they act as a reflector (which is why the name Bragg reflector was coined to these structures), creating a forbidden region of propagation of light. One single structure may have many different gaps due to these reflections. The Bragg gap occur under the following condition (LIANG; HE; CHEN, 2003) for an optical

crystal composed of two materials A and B stacked along the z direction (fig. 9(a)):

$$\frac{2\pi\nu}{c}\left(\cos(\theta_A)n_A d_A + \cos(\theta_B)n_B d_B\right) = p\pi. \tag{3.56}$$

where $\theta_{A,B}$, is the angle in which the wave propagates through layers A, B; ν is the frequency of the wave; $n_{A,B}$ is the index of refraction of media A, B and $d_{A,B}$ is the size of layer A, B. To exemplify this gap we plot (fig. 9(b)) the band diagram of a crystal composed of one material with $n_A = 1.4142$, $n_B = 1.2649$ and incidence angle equal to $\pi/6$. As it's expected, we have the Bragg gap opening up for frequencies obeying eq. 3.56 (integer multiples of 6.59 GHz) .

3.7.1.2 Zero-$< n >$ Gap
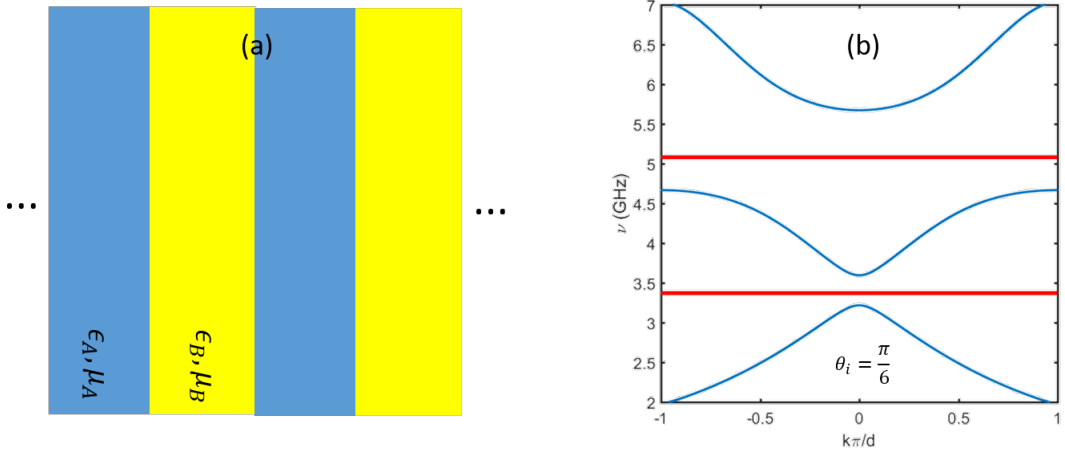
Figure 10 – (a) Pictorial view of the photonic crystal under consideration. The crystal is composed of unit cells consisting of layers A (a linear ordinary nondispersive material) with permittivity $\epsilon_A = 3$ and permeability $\mu_A = 1$, and layers B (a linear dispersive metamaterial) with permittivity and permeability given by eqs. 3.58, 3.59. (b) Band diagram for the photonic crystal described in (a). In blue are the allowed states of the crystal. The red line in 3.37 GHz is where eq. 3.57 predicts the opening up of the zero-$< n >$ gap. The second red line, in 5.08 GHz, corresponds to the magnetic plasmonic frequency. As the theory predicts, a band gap also opens up around this frequency.

Another important gap appears when the crystal is composed of regular materials (with both permittivity and permeability having positive values) and left-hand materials (materials exhibiting a negative index of refraction). The mechanism that opens this gap is completely different from the Bragg reflections. While the regular material propagates the phase of the wave in one direction, the negative material propagates it in the opposite direction, effectively making the phase velocity equal to zero inside the crystal, hindering the propagation. Differently from the Bragg gap, the zero-$< n >$ gap is invariant upon

change of scale length and to disorder. The mathematical condition for this gap to open up is to equate the volumetric average of the index of refraction to zero (LI et al., 2003):

$$n_A(\omega)d_A + n_B(\omega)d_B = 0; \tag{3.57}$$

where $n_{A,B}$ is the index of refraction of layers A, B and $d_{A,B}$ is the size of layers A, B. To exemplify this gap, consider a photonic lattice (fig. 10(a)) composed of a right-hand A material where $\epsilon_A = 3$, $\mu_A = 1$ and a left-hand B metamaterial

$$\epsilon_B = 1.6 + \frac{40}{0.81 - \nu^2}; \tag{3.58}$$

$$\mu_B = 1.0 + \frac{25}{0.814 - \nu^2}. \tag{3.59}$$

As it is predicted by eq. 3.57 the zero-$< n >$ gap opens up around the frequency 3.37 GHz.

3.7.1.3   Plasmon Polariton Gap

The last gap we will talk about is the Plasmon Polariton Gap. In a TE configuration, and for oblique incidence, there is a component of the magnetic field in the direction of the stratification, which couples to the bulk-like longitudinal magnetic plasmon mode, giving origin to the PP gap (CARVALHO et al., 2011; REYES-GÓMEZ et al., 2009), the zero-transmittance region around the magnetic plasma frequency. The same is true for the TM configuration, but instead the gap opens up around the electric plasma frequency. This plasmon-polariton is a hybrid mode resulted from the coupling of light with the matter oscillation. As the electromagnetic wave propagates through the polarizable medium, the induced polarization modifies the wave, coupling it to the plasmonic induced mode, hindering the propagation around the plasmonic frequency. This gap can be seen in the same system studied in the previous section (the zero-$< n >$ gap). If one looks in the magnetic plasmon frequency $\mu_p^m = 5.08$ GHz in fig. 10(b) there's a gap due to the plasmonic interaction with the light wave, as predicted by theory. This gap can be seen as a property of the plasmonic material rather than of the layered system as it exists even when there is only one plasmonic material slab.

4 Light propagation in centrosymmetric media

All the math presented up to here is valid when the wave propagation in matter is independent of the intensity of the electromagnetic field, i.e., we restrained ourselves to the linear theory. In this chapter we will provide an introduction to the topic of light propagation in nonlinear centrosymmetric media, in other words, we will study isotropic linear materials where the Polarization can be written as the sum of two terms: one linear in the electric field and another one proportional to the cubic power of the electric field.

4.1 Third order nonlinear susceptibility

In a previous chapter we showed how to calculate the linear susceptibility using the Lorentz model. The nonlinear susceptibilities are found on a similar fashion, but with $N(x)$ arranged accordingly. As in this thesis only third order nonlinearities will be considered, the analysis presented here will be resumed and limited to centrosymmetric media because no second order nonlinearities can exist in such materials. In media with a center of symmetry the potential energy of the system described by eq. 2.2 has to be symmetric under the operation $x \to -x$. This means that no second order nonlinearity can exist, otherwise $\int N(x)dx$ will result in an odd function and the potential given by eq. 2.3 will not describe a centrosymmetric material. A more detailed approach explaining the different phenomena caused by second and third order nonlinearities using the Lorentz model, as well the explanation for the origin of $\chi^{(3)}$ using first principles, can be found in (OWYOUNG, 1972) and we will not engage in such detailed explanation here. Instead, we will focus on the effects that the system this thesis is proposing to study exhibits.

The response studied here, $\chi^{(3)}$, is not particularly large when studying the interaction of dielectrics with optical fields, but it is very important because it is presented in all dielectric materials. The nonlinear response is usually nonresonant (meaning that optical frequencies are normally very small compared to the resonant frequency of dielectrics), and are typically approximately $\chi^{(3)} \approx 10^{-22} m^2/V^2$. However recent works have shown third-order susceptibilities as large as $10^{-17} m^2/V^2$, and by using epsilon-near zero materials Argyropoulos et al. (ARGYROPOULOS et al., 2012) were able to boost nonlinear effects far beyond the traditional Fabry-Pérot resonant gratings. Moreover, by boosting the intensity of the field inside the material one can mimic a material with a higher $\chi^{(3)}$ as the increase of the material nonlinearity and the increase of field strength leads to the same problem aside from a multiplicative constant. This seems to be the trend in some

recent works, as for them the nature of the nonlinearity is less important than the effects it causes.

Consider the third-order nonlinear polarization $P^{(3)}(t) = \epsilon_0 \chi^{(3)} E(t)^3$. In general, $E(t)$ is made up of several frequency components, however this work is interested in an effect presented when the electric field is monochromatic and is given by:

$$E(t) = E \cos \omega t. \tag{4.1}$$

Using the identity $\cos^3 \omega t = \frac{1}{4} \cos 3\omega t + \frac{3}{4} \cos \omega t$ one can find the following expression for the third-order nonlinear polarization:

$$P^{(3)}(t) = \frac{1}{4}\epsilon_0 \chi^{(3)} E^3 \cos 3\omega t + \frac{3}{4}\epsilon_0 \chi^{(3)} E^3 \cos \omega t. \tag{4.2}$$

The first term corresponds to a frequency generation, more specifically the third-harmonic generation. The second term describes a contribution at the same frequency of the incident field. A contribution that can be seen as a nonlinear contribution to the refractive index. This is the contribution we are interested in studying.

4.2 Optical Kerr effect

As just discussed, a third order nonlinearity causes a nonlinear contribution in the refractive index. Thus, we can write the refractive index of such materials (with a third-order nonlinearity) as:

$$n = n_0 + \bar{n}_2 \left\langle E(t)^2 \right\rangle \tag{4.3}$$

where n_0 is the usual linear refractive index, $\bar{n}_2$ the second-order index of refraction, $E(t)$ is the optical field and $\langle \cdot \rangle$ means a time average. The second-order index of refraction can be seen as the rate which the refractive index varies with the optical intensity. Let's suppose that the optical field is monochromatic, we can write it as $E(t) = E(\omega)e^{-i\omega t}$, then:

$$\left\langle E(t)^2 \right\rangle = 2E(\omega)E(\omega)^* = 2|E(\omega)|^2, \tag{4.4}$$

and

$$n = n_0 + 2\bar{n}_2 |E(\omega)|^2. \tag{4.5}$$

The effect of the change in the refractive index in response to the electric field is called the optical Kerr effect and the material that possess this effect is often called a Kerr material. In this thesis we use the term Kerr material to describe a material where the refractive index depends on the intensity of the electric field.

This effect can also be seen in terms of the electric permittivity. One can write the electric permittivity of a nonlinear Kerr medium as

$$\epsilon_{NL} = \epsilon(\omega) + a|E|^2 \tag{4.6}$$

where ϵ_0 is a constant (the linear electric permittivity), and a is a nonlinear parameter that characterizes the Kerr medium (related to the third-order susceptibility). This relation, eq. 4.6, is the one we are going to use to describe a Kerr medium. We are assuming that in a Kerr medium the magnetic permeability is given by a constant, thus, it doesn't depend on the frequency of the incident wave or on the intensity of the magnetic field.

4.2.1 Self-focusing and self-defocusing

When an intense beam of light is propagating in a medium with a third-order nonlinearity, the medium modifies the index of refraction of the material in a way that the beam comes to a focus within the material. Think of this in terms of the beam intensity, the refractive index will be larger at the center of the beam than at its periphery (for this to happen we are assuming that $\bar{n}_2$, or a, is positive). In this case, the rays of the light beam propagating inside the material curves towards each other, focusing on a point inside the material. This is equivalent to say that the material acts as a positive lens. The beam of light modifies the medium, making the medium a positive lens, and focusing itself, hence the name self-focusing attributed to this effect. The beam is modifying the medium that modifies the beam itself, so the light modifies its own propagation trough the nonlinear response of the material. An interesting consequence of the self-focusing is the self-trapping effect, an effect that occurs when the beam of light propagates with constant diameter due to a balance between self-focusing and diffraction.

While self-focusing occurs when $\bar{n}_2$, or a, is positive, self-defocusing occurs when $\bar{n}_2$, or a, is negative. The same line of thought can be used here. The medium now acts as a negative lens, making the rays of light to repel each other, defocusing the beam. The beam modifies the medium, transforming in in a negative lens, that modifies the beam itself, hence the name self-defocusing.

4.2.2 Optical bistability

Another important effect due to a third-order nonlinearity is bistability, or multistability. These nonlinear effects refer to systems where a single input state is linked to more than one output state. Thus, optical bistability happens when two different transmitted waves are possible for the same incident wave (when considering the case of a wave propagating through a nonlinear slab).

The relation between the input intensity and the output intensity when bistability occurs is better shown by looking at fig. 4.2.2. A good explanation of the behavior of a system presenting multistable behavior is given by Boyd (BOYD, 2008). The dashed portion of the curve shows that in this branch the output intensity increases as the input intensity decreases. This branch is unstable, meaning that if the system is initially in this

state, point g, a perturbation will make it rapidly switch to one of the two other possible solutions. If one blocks (momentarily) the light the system will transit to the lower part of the curve. For clarity, let's call I_b and I_f the intensity on points b and f, respectively. To obtain a transition to the upper part of the curve one needs to probe a pulse of light making the intensity of the incident field bigger than I_b. An experiment that possess this behavior can be seem as displaying hysteresis: if one increases the intensity input from 0 to I_b the result obtained would be the segment going from a to b. If the intensity is now increased to a value greater than I_b the system will jump to the point c and follow the segment labelled c-d. Now, if the intensity is lowered, the system will remain in the upper branch of the curve, the segment c-e, and when the intensity is lowered to values smaller than I_f the system will make a jump to the lower end of the curve, the segment f-a. Gibbs and Lugiato offer some insightful explanation of mulstistable behavior (GIBBS, 2012) and (LUGIATO, 1984).
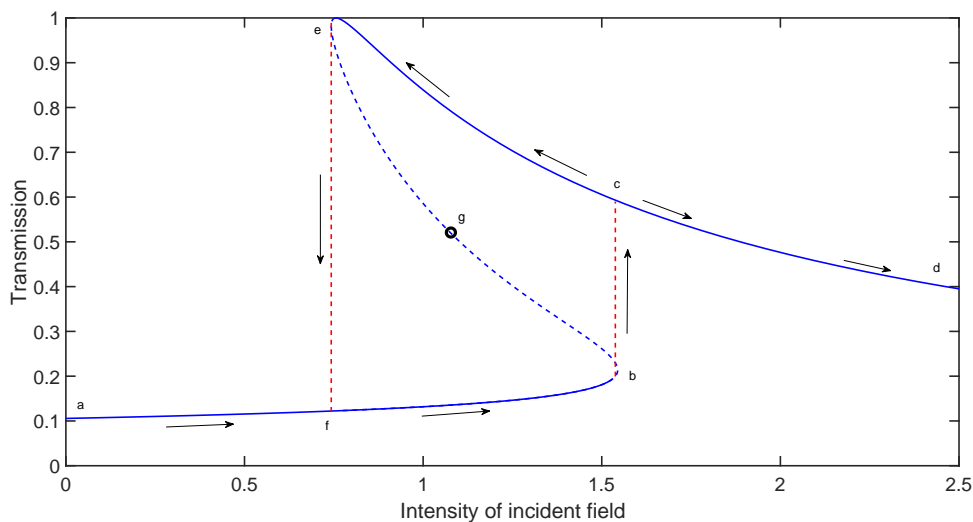
Figure 11 – Pictorial view of bistability. This graph shows the transmission as a function of the incident field intensity, showing hysteresis. The solid blue lines correspond to stable branches of the system under consideration, while the blue dashed line corresponds to an unstable region. The arrows show the direction of the transmission as one varies the intensity field and a more detailed explanation can be found in text.

4.2.3 Optical switching

Another important effect that is observed because of a refractive index that is a function of the intensity of the light is optical switching. The incident beam intensity can change the refractive index from a zero-transmission state to a full transparency mode, by adding a nonlinear phase shift around π radians (with the higher contrast happening when the nonlinear phase shift is exactly π radians).

4.2.4   Solitons

To give a proper explanation about solitons it is important to have the concept of diffraction fresh. When a beam of light travels through air, or a crystal, it broadens with the distance traveled, this is the diffraction. Diffraction occurs even in the absence of dissipation and it's the analogous of the dispersion phenomenon seen in waves traveling in water. The thing is, in 1834 Scott Russell observed a wave that did not disperse. Here is his description of the phenomenon:

> I was observing the motion of a boat which was rapidly drawn along a narrow channel by a pair of horses, when the boat suddenly stopped - not so the mass of water in the channel which it had put in motion; it accumulated round the prow of the vessel in a state of violent agitation, then suddenly leaving it behind, rolled forward with great velocity, assuming the form of a large solitary elevation, a rounded, smooth, and well-defined heap of water, which continued its course along the channel apparently without change of form or diminution of speed. I followed it on horseback, and overtook it still rolling on at a rate of some eight or nine miles an hour, preserving its original figure some thirty feet long and a foot to a foot and a half in height. Its height gradually diminished, and after a chase of one or two miles I lost it in the windings of the channel. Such, in the month of August 1834, was my first chance interview with that singular and beautiful phenomenon which I have called the Wave of Translation. (RUSSELL, 1844)

This effect puzzled scientists for a long time because it can't be explained by the linear theory. In fact, it wasn't until 1895 that Korteweg and Gustav de Vries explained it. They theorized that while dispersion causes a wave to spread, nonlinear effects (specifically self-focusing) may cause it to steepen. When these effects balance each other, this solitary wave propagates with no change in its shape (the wave of translation Russel talked about).

Solitons are encountered in photonic systems as well (Russel observed them in water). Let's describe a case where solitons are encountered in optical media. When considering propagation of light in a nonmagnetic medium with a Kerr nonlinearity, in a steady-state, the paraxial wave equation can be written as (BOYD, 2008):

$$2ik_0\frac{\partial E}{\partial z} + \frac{\partial^2 E}{\partial x^2} = -3\chi^{(3)}\frac{\omega^2}{c^2}|E|^2 E, \tag{4.7}$$

where E is the electric field profile inside the medium, a function of z and x only, and we have considered that the medium is allowed to vary in only one transverse dimension (a wave propagating in a planar wave-guide); ω is the frequency of the incident wave, c is the speed of light and $k_0 = \omega/c$. This equation possesses a solution of the form:

$$E(x, z) = E_0 \operatorname{sech}(x/x_0)e^{i\bar{\gamma}z}; \tag{4.8}$$

where x_0, the width of the field, is given by:

$$x_0 = \frac{1}{k_0}\sqrt{n_0/2\bar{n}_2|E_0|^2};$$ (4.9)

and

$$\bar{\gamma} = k_0\bar{n}_2|E_0|^2/n_0.$$ (4.10)

This solution, eq. 4.8, is the one that is normally referred as spatial soliton. It describes a field that propagates with an invariant transverse profile. This solution describes a first order soliton. Higher order solitons are also known as soliton trains in the literature and can be seen as the sum of various out of phase first order solitons added. These soliton trains are a characteristic of optical lattices containing a Kerr nonlinearity and can be observed for almost all frequencies, as we will show in the results of this thesis.

4.3   Maxwell equations for Kerr materials

The Maxwell equations doesn't change much when adding a nonlinear term in the polarization. The nonlinear polarization has to be added to the constitutive equation of **D**, in this case $\mathbf{D} = \epsilon_0\epsilon\mathbf{E} + \epsilon_0\mathbf{P}^{(3)}$. If one carries out the calculation, the only difference between the linear and the nonlinear case is that eq. 3.40 has a new term added (the second time derivative of the nonlinear polarization $P^{(3)} = a|E|^2E$ multiplied by $\frac{\mu}{\epsilon_0 c^2}$) on the right side. As before, assume that the nonlinear polarization is time-harmonic, as the electric field, which yields:

$$\frac{\partial^2 E_x(z)}{\partial z^2} + k_0^2\left(\epsilon\mu - K^2\right)E_x(z) = -\mu k_0^2 a|E_x|^2 E_x(z);$$ (4.11)

in which some algebra leads to:

$$\frac{\partial^2 E_x(z)}{\partial z^2} + k_0^2\left(\epsilon_{NL}\mu - K^2\right)E_x(z) = 0.$$ (4.12)

The constant K was defined in last chapter when discussing the generalized Snell's law for stratified media. This law, as shown before, is still valid for nonlinear media, thus one may write $K^2 = k_0^2\beta^2$. After the introduction of a dimensionless position $\zeta = k_0 z$ we end up with the same equation as eq. 3.41:

$$\frac{d^2}{d\zeta^2}E_x + (\epsilon_{NL}\mu - \beta^2)E_x = 0;$$ (4.13)

but with the linear epsilon replaced by its nonlinear counterpart. To simulate an linear medium one just needs to set $a = 0$ and the results of eq. 3.41 for linear media are recovered. It is important to notice that the same boundary conditions are applied here and the same integrator used for the linear equation can be used here too. Thus, when dealing with superlattices composed of Kerr materials and linear dispersive metamaterials one can still use the same procedure outlined in section 3.6. Furthermore, there is no need to repeat ourselves here. The same algorithm is used, but now the electric permittivity is set to be a function of the intensity of the electric field.

5 Gap-Solitons Materials

It has been a trend in telecommunications to try to replace the electronics for its optical counterparts. Electronics has been the groundstone of information processing for a long time, and has been experiencing tremendous advances in the past several years, managing to follow Moore's law to this day (which states that the transistor density on a chip doubles approximately every two years). However, as electronics gets closer to its physical limitations (power dissipation, heating, problems processing at high frequencies) photonics is getting more attention. Unfortunately, photonics is still not suitable to replace electronics because of its inherent limitations that make manipulation of signals in the optical domain unfeasible. Photonic crystals have since emerged as a promising solution for these problems. With the addition of nonlinear media into the photonic crystals they can enhance nonlinearities, extend phase-matching abilities aid in the design of optical diodes and switches, compact pulse compressors and frequency converters.

Light pulses propagating in nonlinear photonic crystals can result in sum and difference frequency generation, soliton formation, harmonic generation, parametric oscillation, etc. In particular, we are interested in the soliton formation process in one-dimensional nonlinear photonic lattices where the nonlinear material is Kerr like. These systems exhibit bistable behavior that can be explained by the nonlinear phase-shift modulation of the light beam (GIBBS, 2012). Furthermore, transparency switching is observed and these modes are linked with the solitonic structures found in the system. Transparency-switching phenomenon is observed even in frequencies where the band diagram of the system predicts a gap to exist, coining the name of the solitons found in these regions as gap solitons.

This chapter aims to give a brief historical background of gap solitons, overviewing the seminal works of Mills and Chen (CHEN; MILLS, 1987) and Winful et al. (WINFUL; MARBURGER; GARMIRE, 1979), and explaining the gap-soliton phenomenon in one-dimensional lattices.

5.1 Historical Background

The field of light propagation in nonlinear photonic crystals emerged from the experimental (GIBBS; MCCALL; VENKATESAN, 1976) and theoretical (MARBURGER; FELBER, 1978) demonstration of bistability and hysteresis in a Fabry-Perot interferometer. When filled with a nonlinear material, whose refractive index depends on the intensity, the Fabry-Perot interferometer can be used as an optical transistor, pulse shaper, memory element and differential amplifier. Following these results Winful et al. (WINFUL; MARBURGER; GARMIRE, 1979) showed that the bistable behavior and hysteresis presented

in the Fabry-Perot resonator can be replicated by *distributed feedback structures*, the name given to what we now call photonic lattice. Winful explained that the mechanism behind bistability is related to changes in the Bragg conditions due to the nonlinearity, modifying the wavelength of the waves, which alters the frequencies for the Bragg resonances when one varies the intensity of the electromagnetic field. The same is true for the other gaps, despite the reasoning not being the change in Bragg conditions, but the nonlinear phase shift and the nonlinear dependence of the refractive index.

In 1987 Chen and Mills (CHEN; MILLS, 1987) published a seminal work on gap solitons. Normally, when a dielectric is illuminated with light whose frequency lies within a stop gap, the amplitude of the light will decay exponentially with increasing distance. Chen and Mills have theoretically shown that if one illuminates a finite superlattice consisting of unit cells composed of a linear dielectric and a Kerr material a Bragg gap will partially close with increasing power. This superlattice will exhibit transparency switching, i.e., the system switches from very low transmitting state to a completely transparent state. The powers that allows transparency switch are linked to a partial close of the band gap, shifting the band edge to a previously forbidden frequency. These transparency switching points are always linked to resonant states of the electric field inside the structure, though the specific power needed to achieve the switching varies with frequency. The resonant modes of the electric field are actually soliton-like structures, and they exist for frequencies where the linear theory predicts a band-gap. Chen and Mills coined the term gap solitons to describe these resonant modes of the electric field. Mills and Trullinger have shown in (MILLS; TRULLINGER, 1987), by analytical methods, that when treating frequencies near the band edge the envelope function of the electric field obeys a double-sine Gordon equation (with some considerations made about the index of refraction and the wavelength of the incident field). The sine-Gordon equation allows soliton solutions and they are readily available in the literature. Thus, the soliton-like modes found in superlattices are actually finite representations of the real solitons predicted for the infinite superlattice analog.

The study of the nonlinear response of nonlinear one-dimensional superlattices continued showing significant progress, finding, for example: multistability and optical solitons (KAHN; ALMEIDA; MILLS, 1988), defect modes in nonlinear lattices(LIDORIKIS et al., 1997) and soliton formation and transparency switch in quasiperiodic superlattices (KAHN; HUANG; MILLS, 1989). Trustchel and Lederer (TRUTSCHEL; LEDERER, 1988) studied the effects of a saturable nonlinearity into a superlattice, showing that it hinders bistability and the formation of solitons for high input powers. When considered together with absorption, the saturable nonlinearity makes the hysteresis like behavior of the system to practically vanish. To obtain their results they used a standard Runge-Cutta procedure, similar to the one used in this paper [1].

---

[1]   All the methods used in previous researches to solve equation 4.13 presented some kind of problem: too

A new theory was developed in 1996 by Soukoulis et al. (LI et al., 1996) where an analytical solution for the transmission spectra of a superlattice consisting of unit cells (linear/Kerr) provided that the size of the Kerr layers are infinitesimal and that the impedance is near infinity. These simplifications allowed the numerical calculations of the transmission via a nonlinear map, giving the behavior of the gap-edges with increasing incident power (despite only one of the sides of the gap being studied, as one of them is always locked due to errors inherent to their proposed method).

Discrete solitons is another class of nonlinear phenomena that has received attention in the last few years (SUKHORUKOV; KIVSHAR, 2002; CHRISTODOULIDES; JOSEPH, 1988). In fact, the field of optical solitons has increased dramatically from the one-dimensional photonic crystals we described. Aceves and Wabnitz (ACEVES; WABNITZ, 1989) extended the gap solitons to a more general traveling wave form. Seven years later Eggleton et al. (EGGLETON et al., 1996) experimentally demonstrated the Bragg gap solitons, by propagating a nonlinear optical pulse in a Bragg grating. This soliton arises from the balancing of the high dispersion of the lattice and the self-phase modulation induced by the Kerr type nonlinearity. A good survey of the latest accomplishments in the field of optical gap solitons is presented in (ACEVES, 2000).

5.2   Bragg and Zero-$< n >$ Gap Solitons

The solitons we talked about in the last section were all found in Bragg gaps. When studying a superlattice composed of bilayers (Kerr/dispersive linear metamaterial), one encounter soliton formation near the edges of the Bragg gap. These solitons have the interesting property of having the minima of the electric field nearly zero in the surface of each bilayer. This happens because of the Bragg condition of interference, the phase traveled across each bilayer has to be π. An example of Bragg soliton can be seen in fig. 12.

In 2005 Hedge and Winful (HEGDE; WINFUL, 2005b) showed that gap solitons are also found around the edges of the zero-$< n >$ gap. This gap has different behavior than the Brag gap soliton. For starters, the electric profile for the solitonic solution does not goes to zero, instead local maxima and minima occurs at the interface between the layers. Moreover, this soliton is robust in relation to the angle of incidence, while the Brag gap soliton is very sensitive to the angle of incidence (the change in the incidence angle, changes the position of the Bragg gap, which changes the position of the Brag gap soliton).

computationally expensive to present a complete analysis; not enough accuracy to study the desired effects and simplifications in the formulation handicapping the study. The numerical method proposed in this thesis makes no simplification to eq. 4.13, has the advantage of using computers way faster than the ones available to the previous authors, and is accurate enough to show all the relevant effects presented in the problem.
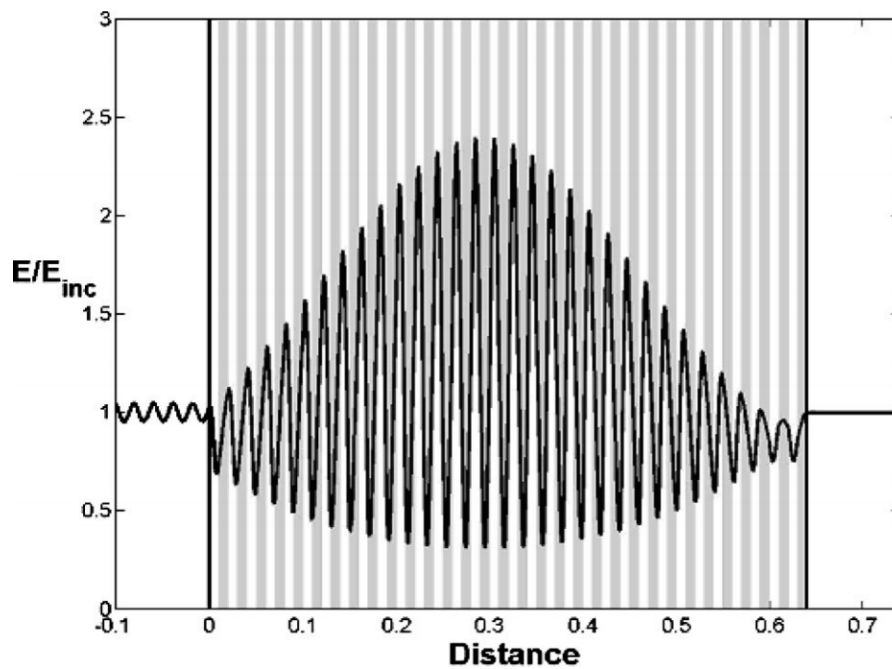
Figure 12 – The Bragg gap soliton observed in a lattice consisting of 32 bilayers of a Kerr material and a dispersive linear metamaterial for normal incidence. The electric field minima is nearly zero because of the phase shift of approximately π across each bilayer. Source: (HEGDE; WINFUL, 2005b)

A more detailed characterization of both gap solitons, as well the transparency switching phenomenon is in progress and partial results are shown in another chapter.

5.3 PP Gap Soliton

The formation of gap solitons are also observed for frequencies in the vicinity of the PP gap, as shown in (CAVALCANTI et al., 2014). These solitons are very robust and will be the subject of study in chapter 8.
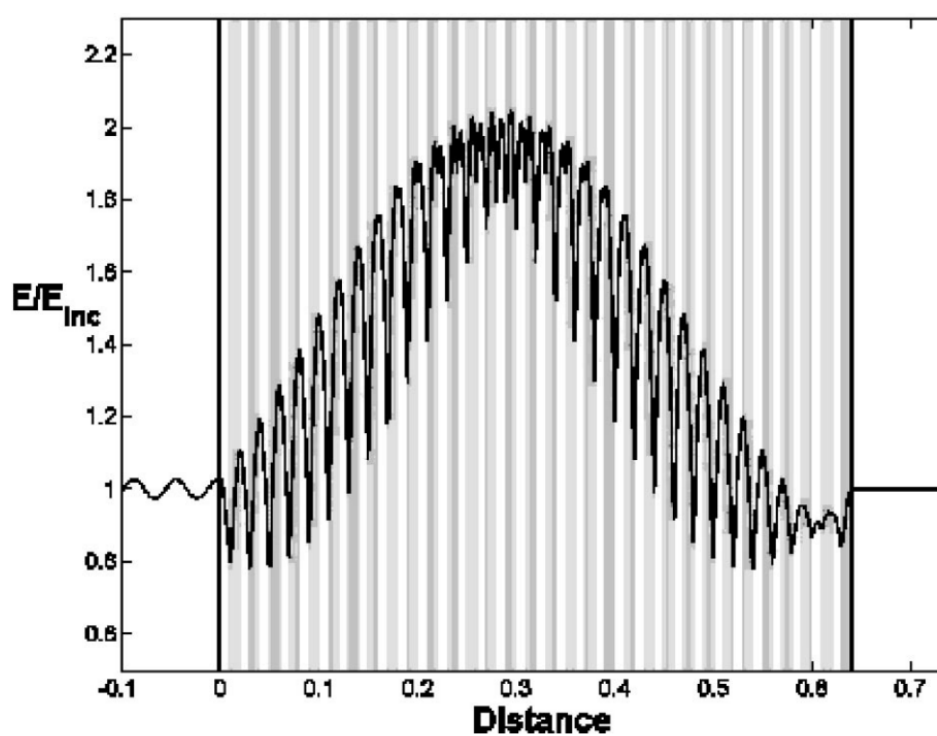
Figure 13 – The zero-$< n >$ gap soliton observed in a lattice consisting of 32 bilayers of a Kerr material and a dispersive linear metamaterial for normal incidence. For this soliton, each bilayer advances the phase of the electric field for a value of approximately 0 (as the average refractive index is near 0). Source: (HEGDE; WINFUL, 2005b)

6 Computational system

To solve the problem of wave propagation in a multilayered system a computer program was developed using MATLAB (MATLAB, 2017). The program uses an adaptive Runge-Kutta formula, the Dormant-Prince pair, to integrate equation 4.13 through the lattice. The lattice can be composed of any number of layers, with each layer having its own material with any equation for the magnetic permeability and electric permittivity. Moreover, the program is also able to have slabs of a nonlinear Kerr material with magnetic permeability and electric permittivity as described in equation 4.6. Due to the nature of the numerical method used, it is straightforward to study nonlinear wave propagation through one-dimensional lattices composed of other types of materials (polaritonic materials, materials with a second-order nonlinearity, etc.) than the ones this thesis aims to study.

The program developed receives as input the embedded material parameters, the number of different materials the layered system has and their respective equations (their magnetic permeability and electric permittivity can be any function of the frequency or a Kerr metamaterial); and the positions of the layers. With these (the initial conditions), the program can give a variety of results (fig. 14): transmittance, reflectivity or the band diagram of its respective linear problem; transmittance or reflectivity versus nonlinear power; electric field profile versus distance versus nonlinear power; transmittance or reflectivity versus nonlinear power versus frequency. Thus, the mathematical formalism and the program developed here can be used to run a variety of other cases, leaving room to contributions beyond the ones presented here.

The program was developed both in MATLAB and in C++. Despite MATLAB's own implementation of the Dormant-Price integration scheme (the *ode45* function), some optimizations were needed to tailor the program to our specific problem.

One problem with our integration procedure arises when the frequencies get closer to the gap center. When approaching such frequencies, the transmission becomes a very rapidly varying function of the nonlinear power. In conjunction with the unevenly distribution of the nonlinear power, this creates a sampling problem. To integrate eq. 4.13 we provide the value of both the transmitted field and it's derivative, and then calculate the incident and the reflected fields. This uncertainty in the incident field creates a somewhat random distribution for the nonlinear power $a|E_i|^2$ as a is linearly spaced and $|E_i|$ is a function of a (for our integrator). Furthermore, the increments of a have to be carefully chosen as a small increase in its value can lead to a loss of information of the nonlinear power. This problem is still being tackled and the workaround used in this thesis was to manually check the continuity of $a|E_i|^2$ and to set the values of a accordingly. Despite exhibiting
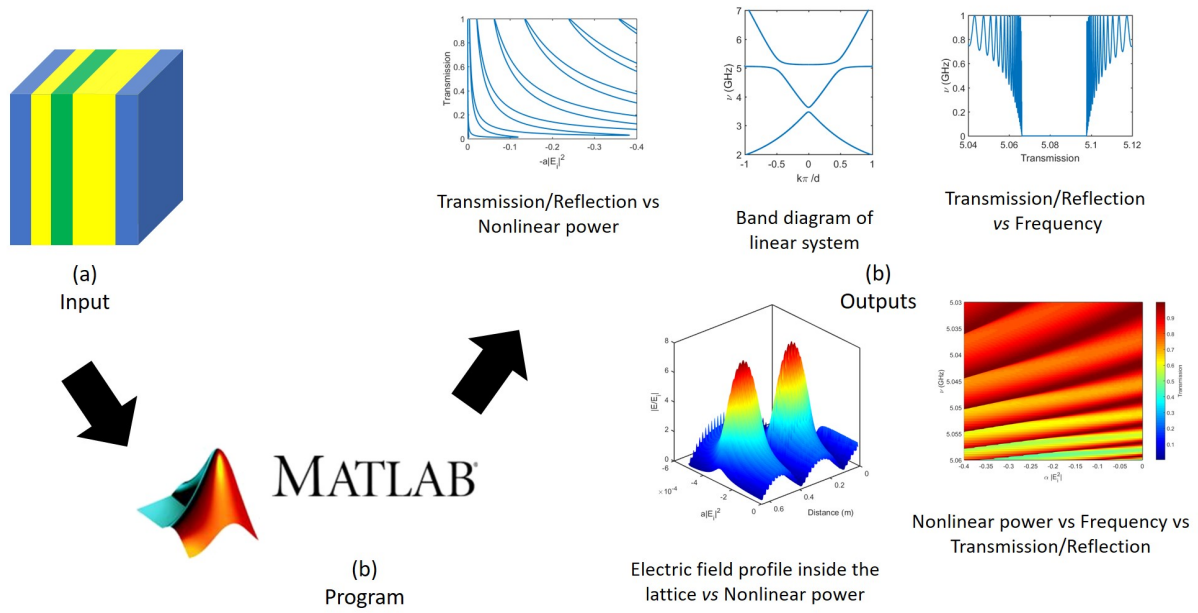
Figure 14 – Schematic of the computer program. The program, coded in matlab (b), uses a input file containing the information about the lattice (a) and is capable of providing the outputs in (c). In particular, the outputs wanted are outlined in the input file (a).

good results, this methodology is not suitable to deal with big frequency discretizations, as for each value of the frequency the values of *a* have to be adjusted. One strategy we believe will be suitable is to use an adaptive integration algorithm to choose the values of *a*, but as we do not have an equivalent of the Courant-Frederichs-Lewys condition (as *a* is not really an integration parameter, it just behaves like one), it is still a challenge to pinpoint the increment of *a* in order to obtain a continuous nonlinear power function and to not lose any information with the discretization. More work is still needed to find a methodology able to overcome this limitation.

We also build three dimensional surfaces in our results. To the best of our knowledge, this type of visualization technique was yet to be applied to show the multistable behavior of the transmission (fig. 15). Because of the multistable behaviour, and the quasi chaotic nature of the function near the center of the gaps, the 3D surface we want to plot is normally not convex, making usual triangulation techniques, like Delaunay, to not depict the real surface (hiding multistability, different solitonic modes are merged, noise, etc.). Instead, we changed the way the data was stored and the triangulation. To create a 3D plot we first determine the axis of the plot. Consider the case of a transmission *vs* nonlinear power *vs* frequency plot, as in fig. 15. The code will fix a value for frequency and calculate the transmission and nonlinear power for such value. Consider that the frequency assume discrete values $\nu = nd\nu$, where n is the discretization parameter and $d\nu$ is the frequency increment. We then proceed to calculate the transmission function $T(\nu_n, a_j|E_i(a_j)|^2)$ for
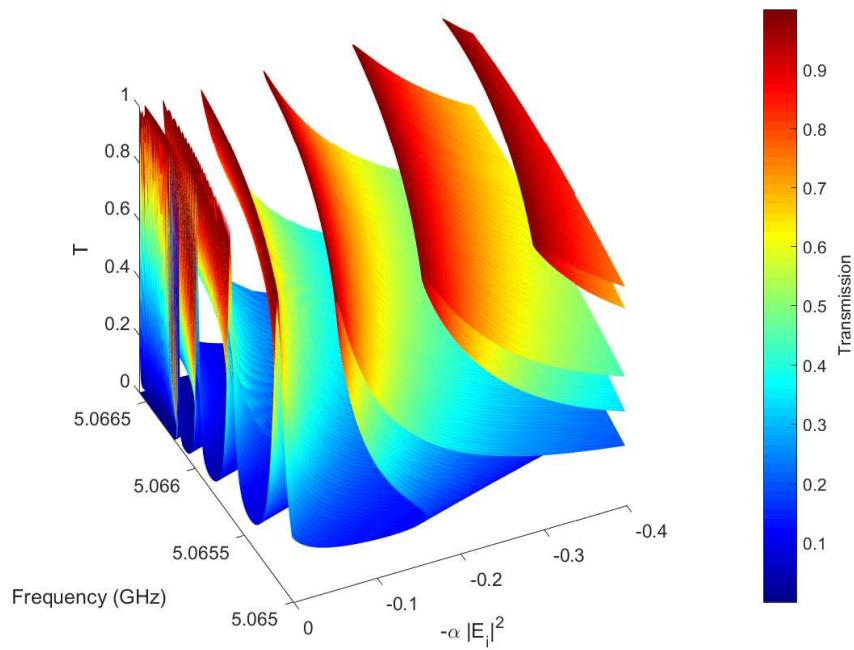
Figure 15 – Pictorial view of the types of 3-dimensional graphics we construct. One can observe a multistable behavior, nonconvex surfaces and very high curvatures (leading to bigger point densities).
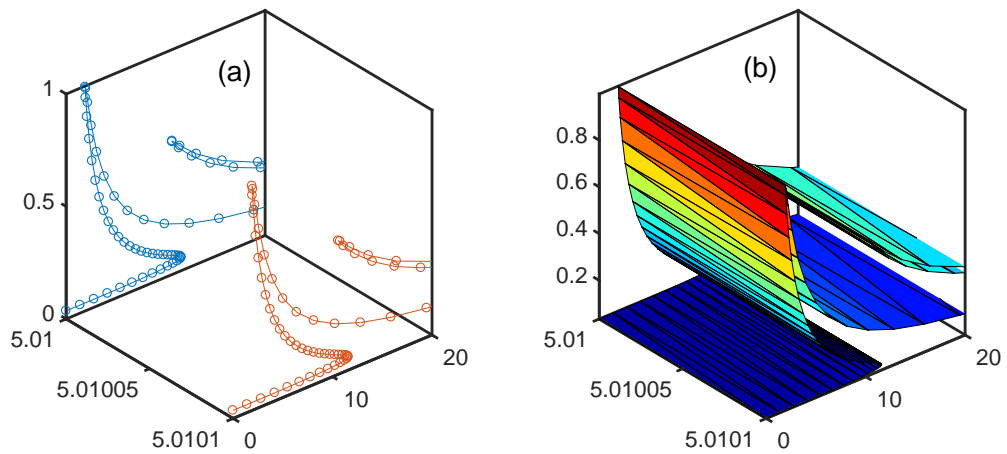
Figure 16 – Schematic of the triangulation procedure used to generate surfaces: (a) shows two functions that are going to form a surface. These functions have to be similar to each other; (b) shows the triangulated surface between the curves, with a procedure explained in the text.

varying nonlinear power (with a fixed n we vary j and store T), considering that a_j is now a discrete variable. To generate the surface we get two consecutive values of n ($n+1$, $n+2$) and plot the curves for these parameters ($T(\nu_{n+1}, a_j|E_i(a_j)|^2$ for all j) as in fig. 16(a). The next step is to create the surface that these curves spans. The building blocks of the surface were chosen as triangles. The procedure to create the triangles is as follows: the first two points of the $n+1$ curve and the second point of the $n+2$ curve are linked to form a triangle, then the third and fourth points are linked to the fourth point of the $n+2$ curve forming another triangle. This procedure is repeated and the same is done for the second curve: the first and second points of this curve ($n+2$) is linked to the first point of the $n+1$ curve. In the end, we end up with a surface as in fig 16(b). The same algorithm is applied to the construction of the electric field as a function of the lattice and the nonlinear power.

In conclusion, we created a program that is capable of dealing with the highly varying nature of the transmission when one sweeps frequencies closer to the center of a band gap. Our program has an error that is sufficiently small to deal with these variations and is capable of extracting huge amounts of data and present them correctly. Some of the 3D surfaces shown in this thesis are composed of more than one million triangles and some of the 2D curves have more than 100000 points. The increasing performance encountered in today computers allowed the numerical simulation of eq. 4.13 to be done without major trade-offs and to run the analysis of complete frequency bands rather than a specific values of frequency (as this is the common procedure encountered in the literature).

7 Defect modes in a nonlinear strip

The study of light propagation in photonic lattices are a hot topic these days due to the advances in the development of metamaterials. Being able to create photonic lattices composed of plasmonic materials, regular materials and negative refractive index materials enabled the creation of better waveguides (BROENG et al., 1999), light-emitting diodes (BORODITSKY et al., 1999) and 3D mirrors (CHENG; SCHERER, 1995). Moreover, these periodic structures exhibit frequency regions where no light can pass, the photonic band-gaps. As shown in earlier chapters, different band gaps may appear when considering linear lattices composed of alternate layers of different linear dispersive metamaterials. The addition of a defect layer into these lattices creates localized resonant modes inside the photonic band gap. These resonant modes can be interpreted as the creation of a pass band inside a previously forbidden frequency band and are usually called defect modes. The study of these defect modes are important because it enables the custom design of optical devices such as witches, filters, and modulators.

In the linear regime, the study of defect modes in lattices composed of single-negative (permittivity or permeability negative) with multiple single-negative defects were carried out by Chen (CHEN, 2008). Similar studies were realized in (CHEN, 2009; OUCHANI et al., 2009; LU, 2011) and proved to be of great importance in the design of optical filters. Moreover, even systems composed of just three layers were shown to present resonant modes depending of the size of the middle layer (KANG et al., 2013; COJOCARU, 2011; BROVENKO et al., 2009). Inspired by these works, Costa et al. (COSTA; MEJÍA-SALAZAR; CAVALCANTI, 2016) showed that defect modes in superlattices can be seem as tunneling resonances in trilayers structures.

Nonlinear defects were also studied by the literature. The response of a single nonlinear dielectric layer sandwiched between two linear dielectric structures were studied by Soukoulis et al. (LIDORIKIS et al., 1997). He used the Kronig-Penney δ-function model to model the problem and found gap soliton formation, multistability and showed that the defect mode changes parity with increasing nonlienarity. Mejia-Salazar (GÓMEZ; MEJÍA-SALAZAR, 2015) studied the formation of gap solitons in the defect mode inside the PP-gap, concluding that the transparency switching phenomenon does not occur for a increasing defosucing nonlinearity if the lattice is asymmetric.

This chapter aims to study the effects of a linear defect mode in a nonlinear strip. As a starting point we consider a reduced system as in fig. 17. Layers B are a Kerr material:

$$\epsilon_B = 2 + a|E|^2; \tag{7.1}$$

$$\mu_B = 1. \tag{7.2}$$
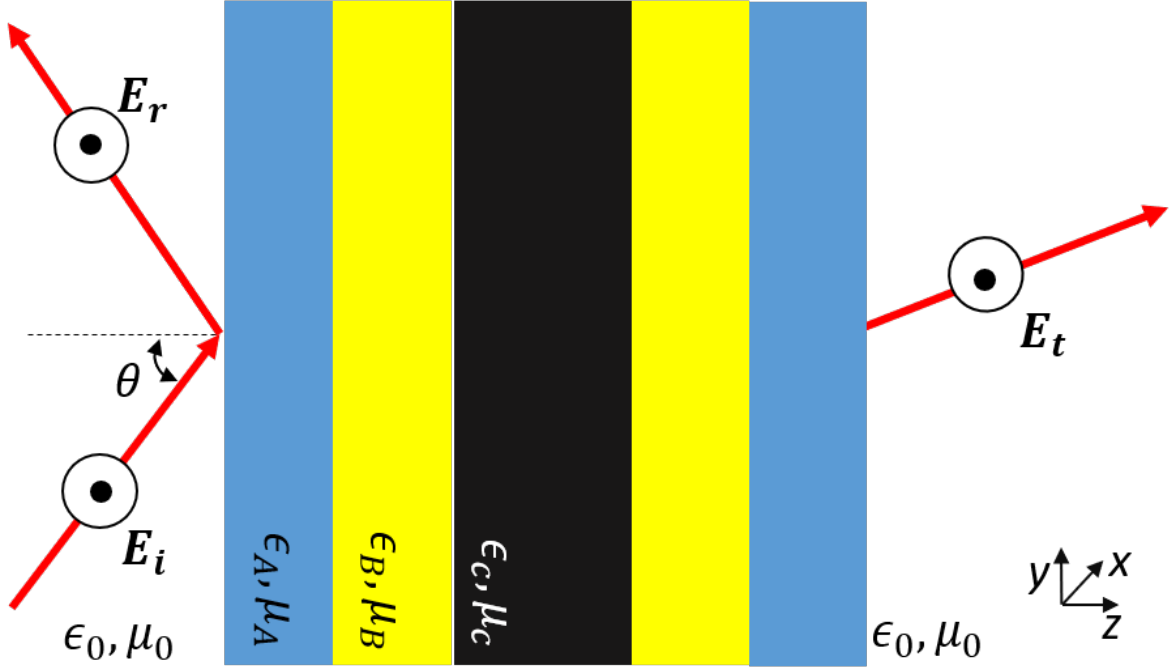
Figure 17 – Pictorial view of the lattice under consideration.

Layers A are a dispersive linear metamaterial:

$$\epsilon_A = 1.6 + \frac{40}{0.81 - \nu^2 - i\nu\gamma} \tag{7.3}$$

$$\mu_A = 1.0 + \frac{25}{0.814 - \nu^2 - i\nu\gamma} \tag{7.4}$$

where ν is the frequency in GHz and γ accounts for absorption. Layers C are a linear nondispersive material where:

$$\epsilon_C = 3; \tag{7.5}$$

$$\mu_C = 1. \tag{7.6}$$

We chose the dimensions of layers A and B to be $d_A = d_B = 0.01$ m. Layer C size, d_C, will be a parameter studied in this article. We aim here to study the effect of a defect layer into a lattice composed of a nonlinear Kerr material and a linear dispersive metamaterial embedded by vacuum.

7.1 Defect modes in the plasmon polariton gap in the absence of nonlinearity

As a starting point we choose the defect layer size d_C equal to the size of layers A and B, 0.01 m, and study the effects of the incidence angle θ_i into the transmission
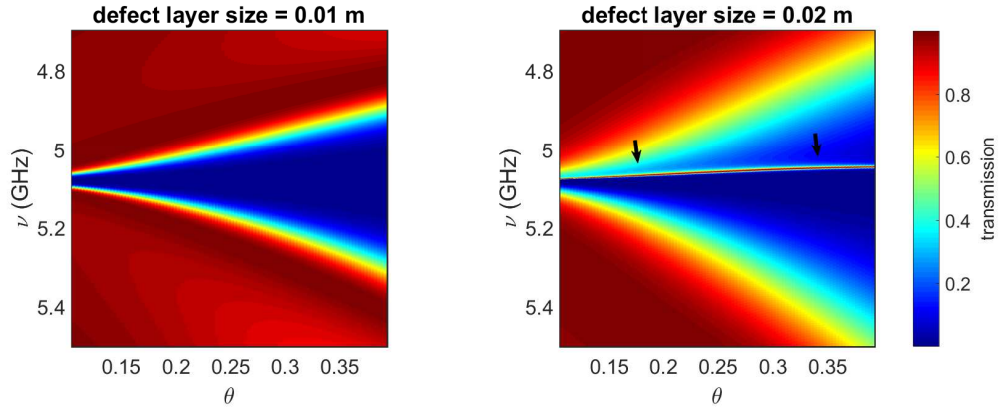
Figure 18 – Transmission as a function of frequency and incidence angle in the absence of nonlinearity, $a = 0$, and absorption, $\gamma = 0$. We chose d_C to be equal $0.01, 0.02$ m for (a) and (b), respectively. One can see that depending on the size of d_c a defect mode may appear inside the bandgap.
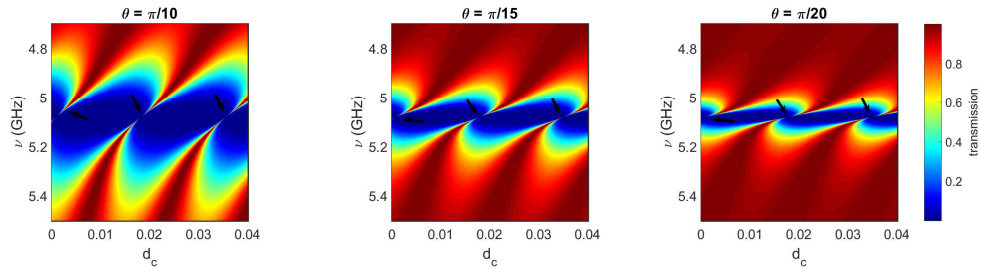
Figure 19 – Transmission as a function of frequency and defect layer size in the absence of nonlinearity, $a = 0$, and absorption, $\gamma = 0$ for three different incidence angles: (a) $\theta = \pi/10$; (b) $\theta = \pi/15$ and (c) $\theta = \pi/20$. Black arrows indicates the defect modes in each figure.

properties of the lattice in the absence of nonlinearity ($a = 0$). Figure 18(a) shows the transmission of the lattice as a function of the incidence angle θ_i and frequency ν in the absence of nonlinearity. The plasmon-polariton (PP) gap opens up with increasing θ_i, as its expected. By increasing the defect layer size, d_C, to twice the size of the layers A and B one can see the creation of a defect mode inside the PP gap, as shown in fig. 18(b). The creation of this mode, indicated by arrows in fig. 18(b), is not specific to a single value of the defect layer size. By sweeping the frequencies around the plasmonic frequency $\nu_p = 5.08$ GHz for any $\theta_i > 0$ one can show that these defect modes occurs for specific values of (θ_i, ν, d_C). If fig. 19(a), we plot the transmission as a function of frequency and defect size for $\theta_i = \pi/10$. Defect modes appear for every value of frequency inside the PP gap, and the same occurs for different values of θ_i, as seen in figs. 19(b) and (c). Costa et al. (COSTA; MEJÍA-SALAZAR; CAVALCANTI, 2016) have shown this periodic characteristic of the defect mode for normal incidence on a Bragg gap. To
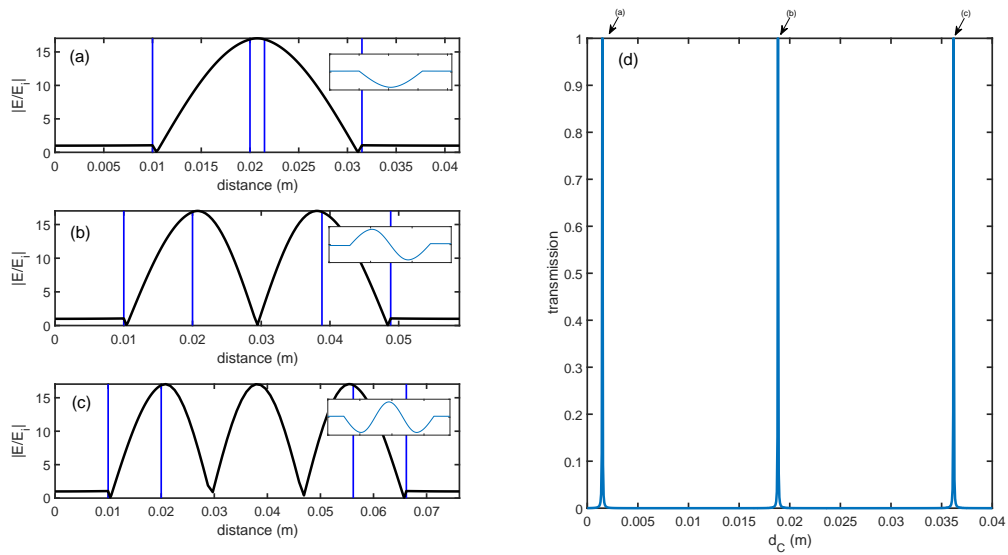
Figure 20 – (d) Transmission as a function of defect layer size d_C, in the absence of nonlinearity ($a = 0$), and absorption, ($\gamma = 0$) for $\theta = \pi/10$ and $\nu = 5.07$ GHz. Three transparency points are found ($d_C = 0.0014, 0.018, 0.036$). The transparency points are periodic (with period 0.0173) and more can be obtained by expanding the defect layer size axis. (a), (b) and (c) show the normalized electric field profile for the transparency points ($T = 1$) shown in (d). Each transparency point is linked to a *n*-peak electric profile, and as one increases the defect layer size, one can see the switching in the parity of the functions, as shown by the insets.

do so, they used the effective medium theory to treat each lattice surrounding the defect as a single layer when the incidence angle is zero. Furthermore, they have compared the problem of light propagation through a trilayer to the quantum problem of a particle in a finite potential. Using the bound state model, they have shown that the resonant states in the quantum problem are equivalent to the defect modes found in the photonic lattices. However, the oblique incidence problem has not yet been addressed in the literature, as far as we know. We believe that the only change between oblique and normal incidence in the bound state model is a normalization constant, and that the incidence angle plays no role in the period of the defect mode. In fig. 19 we plot the transmission as a function of frequency and defect layer size in the absence of nonlinearity and absorption for three different incidence angles. As one can see the period of the defect mode is not affected by the change in the incidence angle. The main difference between figures (a), (b) and (c) is the gap size. The PP gap shrinks in size with decreasing incidence angle, and this behavior is expected due to the nature of the plasmon polariton gap. As the incidence angle increases there is a greater component of the magnetic field in the direction of the stratification, inducing a stronger plasmon, and increasing the PP gap size.

Figure 20(d) shows the transmission as a function of the defect size for a $\nu = 5.07$
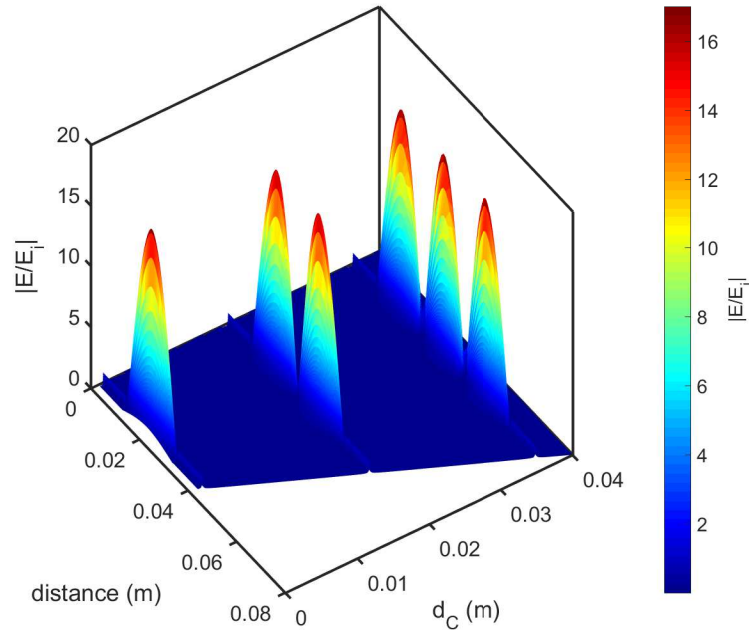
Figure 21 – Electric filed profile as a function of defect layer size (d_C). The axis labeled as distance is the z distance inside the strip.

GHz. One can clearly see that the transparency points ($T = 1$) are periodic, as discussed earlier, with a period of 0.0173 m. Each transparency point is linked to a resonant mode of the lattice under consideration, being the first defect mode linked to the one peak electric field profile shown in fig. 20(a), the second to the two peak electric field profile (fig. 20(b)) and the third linked to the three peak electric field profile shown in fig. 20(c). Furthermore, the resonant modes exhibit a definite parity, that is switched as one choose consecutive resonant modes, as shown in the insets of the figures. The one- and three-peak modes are even, while the two-peak mode is odd. This trend continuous for higher values of the defect layer size: as one chooses the immediately next defect mode the electric field profile will undergo a parity switch and have its number of peaks increased by one. Another characteristic is that these modes are highly localized around one value of the defect layer size. As one chooses values of the frequency closer to the center of the plasmon polariton gap the peaks on the transmission approaches a delta function, as one can see from figs. 20(d). In addition, the electric field profile decays very rapidly for values of the defect layer moving away of the resonant mode, and increases very rapidly for values of the defect layer approaching the resonant mode (fig. 21).
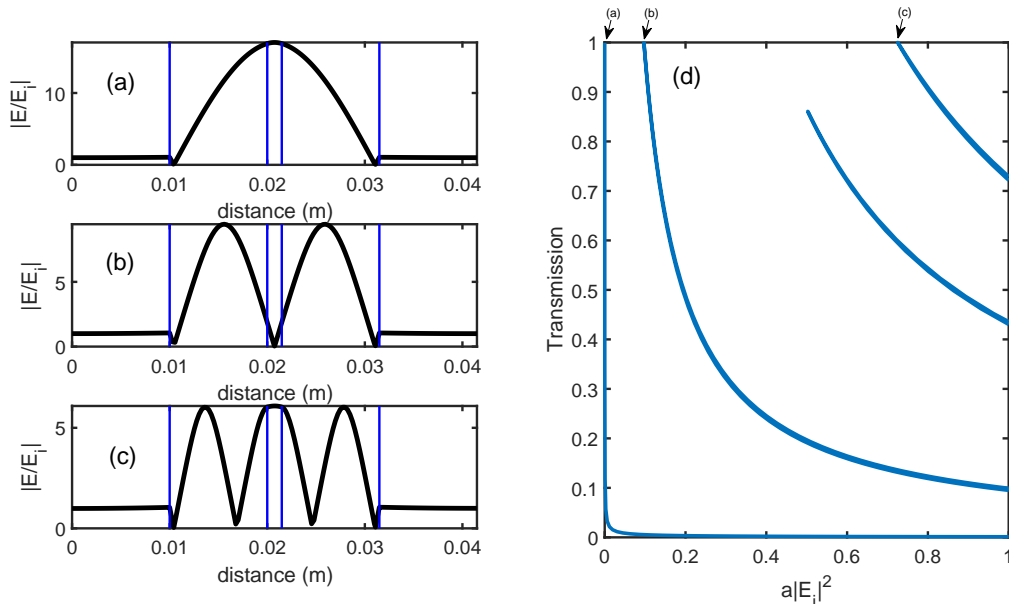
Figure 22 – (d) Transmission as a function of an increasing focusing nonlinearity for $d_C = 0.0014$ m in the absence of absorption for $\theta = \pi/10$ and $\nu = 5.07$ GHz. Three transparency points are found ($a|E_i|^2 = 0, 0.097$ and 0.725) and one resonant mode not linked to a transparency point is found between the peaks indicated by the arrows (b) and (c). Plots (a), (b) and (c) show the normalized electric field profile for the transparency points ($T = 1$) shown in (d). Each transparency point is linked to a n-peak electric profile, and as one increases the nonlinear power, each consecutive transparency point gets its electric field solution number of peaks increased by 1.

7.2   Defect modes in the presence of nonlinearities

We will now proceed to study the effects of an increasing focusing ($a > 0$) nonlinearity in the defect modes of the system. Before sweeping all values of the defect layer size, it is necessary to study more carefully the defect modes for a fixed frequency. We here choose $\nu = 5.07$ GHz as this system was already studied last section in the absence of nonlinearity (fig. 20), and now the effects of a focusing nonlinearity will be studied in the defect modes (the peaks indicated by the arrows in fig. 20). The first defect mode occurs when $d_C = 0.0014$ m, and fig. 22(d) presents the transmission of the system as a function of a focusing nonlinearity. One can see that we observe full transparency ($T = 1$) for specific values of nonlinear power ($a|E_i|^2| = 0.000$, 0.097 and 0.725). The system also shows multistable behavior, as it is expected for a Kerr material. Each transparency point is connected to a resonant state of the system. Figure 22(a) is connected to the first transparency point (0.000) and presents a single peak in the electric field profile; figure 22(b) is connected to the second transparency point ($a|E_i|^2 = 0.097$), presenting two peaks in this mode; and figure 22(c) is connected to the third transparency point ($a|E_i|^2 = 0.725$), presenting three peaks. This shows that increasing the intensity of the
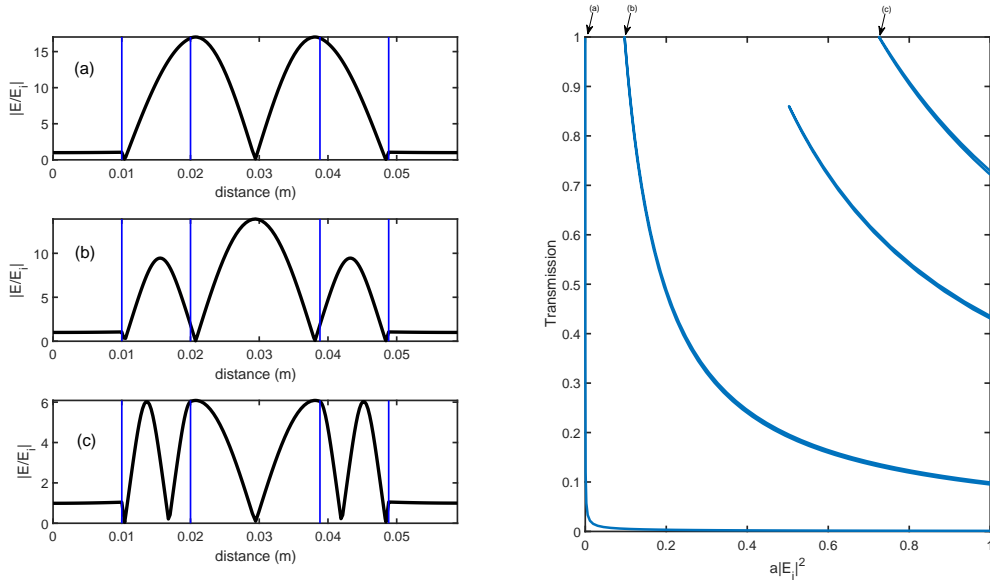
Figure 23 – (d) Transmission as a function of an increasing focusing nonlinearity for $d_C = 0.018$ m in the absence of absorption for $\theta = \pi/10$ and $\nu = 5.07$ GHz. Three transparency points are found ($a|E_i|^2 = 0, 0.097$ and 0.725) and one resonant mode not linked to a transparency point is found between the peaks indicated by the arrows (b) and (c). Plots (a), (b) and (c) show the normalized electric field profile for the transparency points ($T = 1$) shown in (d). Each transparency point is linked to a n-peak electric profile, and as one increases the nonlinear power, each consecutive transparency point gets its electric field solution number of peaks increased by 1.

incident beam causes the number of peaks in the electric field profile to increase. This happens because as we increase the nonlinear power the electric permittivity of the system also increases, effectively increasing the index of refraction of the layers (and consequently, of the system). This increase in the index of refraction effectively extends the optical path length, allowing resonant modes of higher order to be achieved for the same linear parameters of the system, including the size of the defect layer.

For the second defect mode ($d_C = 0.018$) shown in fig. 20(d), we plot the effects of a focusing nonlinearity in its transmission properties and electric field profile in fig. 23. We observe full transparency ($T = 1$) for specific values of nonlinear power ($a|E_i|^2| = 0.000$, 0.097 and 0.725), the exact same values of the first defect mode (fig. 22). In fact, the whole transmission function is identical, and this will be addressed latter. The main difference between the two defect modes shown (figs. 22 and 23) is the electric field profile for the transparency points. While for the first defect mode ($d_C = 0.0014$ m) the first, second and third transparency points are linked to the one, two and three peaks electric field profile, the second defect mode ($d_C = 0.018$ m) has no one peak electric field profile. Instead the first transparency point is linked to the two peak electric profile mode (fig.
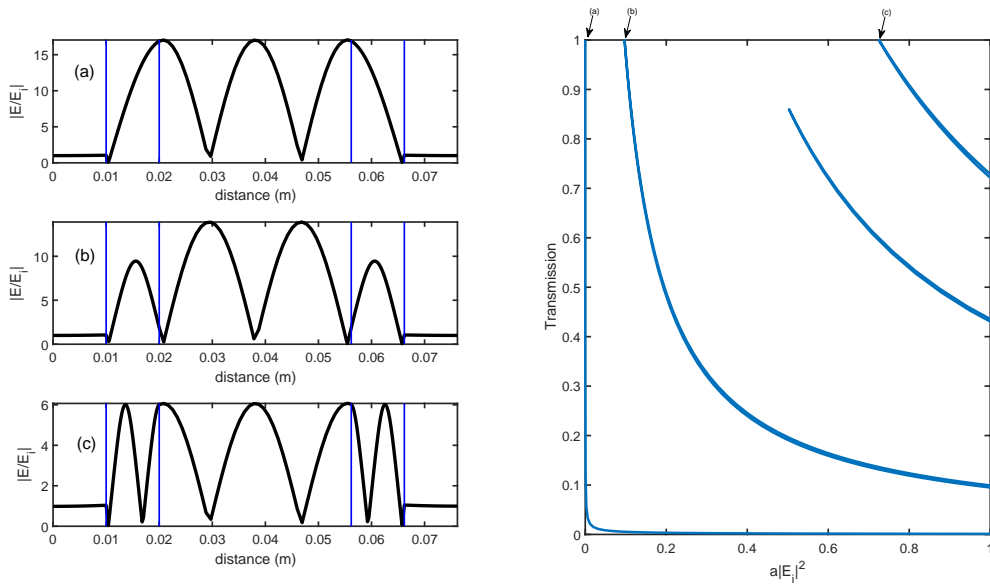
Figure 24 – (d) Transmission as a function of an increasing focusing nonlinearity for $d_C = 0.036$ m in the absence of absorption for $\theta = \pi/10$ and $\nu = 5.07$ GHz. Three transparency points are found ($a|E_i|^2 = 0, 0.097$ and 0.725) and one resonant mode not linked to a transparency point is found between the peaks indicated by the arrows (b) and (c). Plots (a), (b) and (c) show the normalized electric field profile for the transparency points ($T = 1$) shown in (d). Each transparency point is linked to a n-peak electric profile, and as one increases the nonlinear power, each consecutive transparency point gets its electric field solution number of peaks increased by 1.

23(a)), the second transparency point is linked to the three peak electric profile mode (fig. 23(b)) and the third transparency point is linked to the four peak electric profile mode (fig. 23(c)). The lack of one peak electric profile mode is explained in the linear theory, which shows that for this size of the defect layer the electric profile solution has two peaks. The obvious place to look for the one peak solution would be in negative values of nonlinear power (a defocusing nonlinearity). Unfortunately, the transmission decays exponentially for negative values of nonlinear power, and no one peak solution is excited. Furthermore, the same explanation as before can be given for the increase in the number of peaks with nonlinear power, the increase in the optical path length: as the nonlinear power increases, the transparency points associated with the defect mode will have a bigger mean optical path length, allowing more peaks to exist in the electric profile. Figure 24 shows the behavior of the third defect mode shown in fig. 20(d). As expected, each transparency point is linked to a n-peak electric profile, starting from three (as this is the solution of the linear case). Again, the transparency points are exactly the same as the previous two defect modes, as is the whole transmission as a function of the nonlinear power.

In short, an increasing focusing nonlinearity increases the number of peaks in the
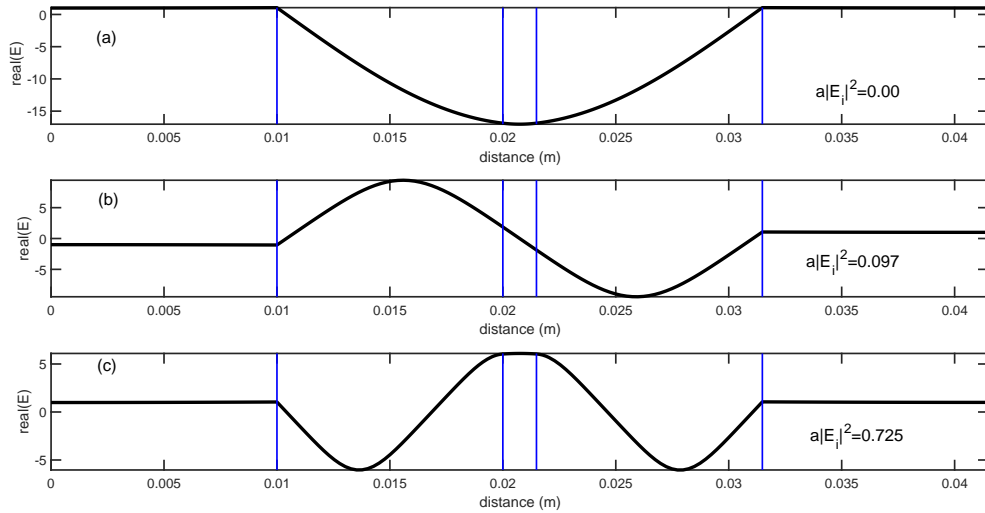
Figure 25 – The real part of the electric profile for $\nu = 5.07$ GHz, $d_C = 0.0014$ m and $a|E_i|^2 = 0.00, 0.097$ and 0.725, for figures (a), (b) and (c), respectively. Figure (a) corresponds to the real part of the electric field profile depicted in fig. 22(a), (b) corresponds to 22(b) and (c) corresponds to 22(c). One can clearly see the parity of each function just by looking at these graphics.
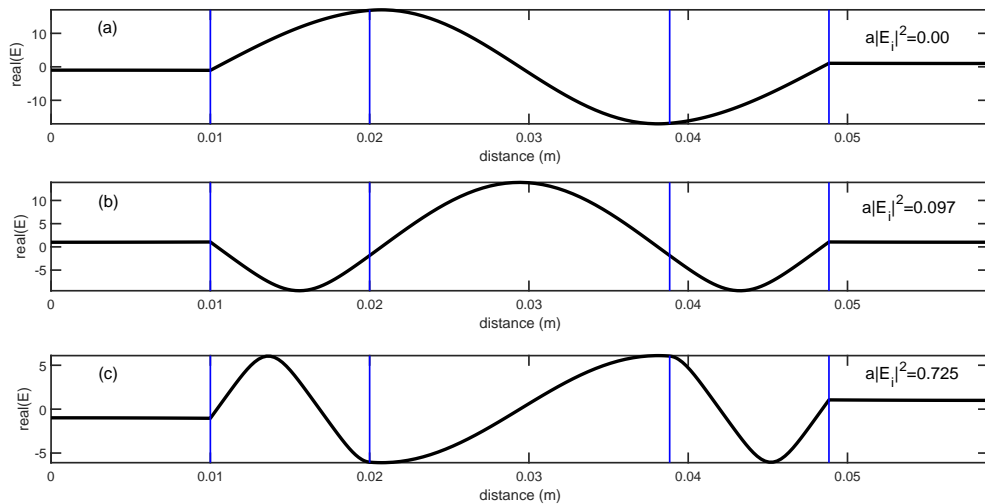
Figure 26 – The real part of the electric profile for $\nu = 5.07$ GHz, $d_C = 0.018$ m and $a|E_i|^2 = 0.00, 0.097$ and 0.725, for figures (a), (b) and (c), respectively. Figure (a) corresponds to the real part of the electric field profile depicted in fig. 23(a), (b) corresponds to 23(b) and (c) corresponds to 23(c). One can clearly see the parity of each function just by looking at these graphics.

electric field profile of the defect modes, mimicking the effect of a larger defect layer. With a higher intensity one can achieve a similar result as one would achieve by increasing the defect layer size (disregarding the multistable behavior exhibited by the nonlinear strip, a signature of nonlienarity). This analogy is very accurate, as it also predicts the change in parity of the electric profile. In the linear case, as the defect layer size increases, the parity of the functions associated with each consecutive defect mode switches (as shown in the insets of figs. 20(a), (b) and (c)). The same is valid for the resonant modes found when we increase the nonlinear power (depicted by the arrows in figs. 22, 23 and 24). Each consecutive transmission point for a specific defect mode changes its respective electric field profile parity. In fig. 25 we plot the real part of the electric field profile associated with each arrow of fig. 22. As one can see, the first and third peaks (figs. 25(a) and (c)) are associated with pair electric profiles while the second peak (fig. 25(b)) is even. This parity change can also be seem in for the second defect mode ($d_C = 0.018$), shown in fig. 26, and for the third defect mode ($d_C = 0.036$), not shown here to avoid redundancy.

In the previous analysis we also encountered periodicity in the transmission functions with increasing nonlinear power. Figures 22(d), 23(d) and 24(d) have the same exact values (as checked by subtracting their values). To investigate this further we plot the transmission as a function of nonlinear power and defect layer size (for $\nu = 5.07$ GHz) in fig. 27. This figure shows that the transmission is periodic even for values of nonlinear power different from zero (the linear case). The black line corresponds to the defect mode associated with the size $d_C = 0.014$ m. This result suggests that the resonant modes of the bound state model are still present even in the presence of nonlinearity (and the addition of a nonlinearity in the system doesn't change the periodicity of occurrence of the resonant modes). Moreover, one can probably still define an effective permittivity and effective permeability even in the presence of a nonlinearity, possibly allowing a nonlinear lattice to be viewed as a linear lattice with adjusted permeability and permittivity (now functions of the nonlinear power and frequency), although the mathematical formalism to do so is still unclear.

The red lines in fig. 27 represent the n-peak electron profile solutions (the resonant modes). These modes exist for every value of d_C and vanishes for a specific values of the defect layer size d_C^n. The vanishing values d_C^n corresponds to the defect modes in the absence of nonlinearity. In this case $d_C^2 = 0.018$m, $d_C^3 = 0.036$ m, and so forth. The arrows in fig. 27 shows the number of peaks that the electric profile associated with that line have. Another interesting phenomenon occurs, and we highlight it in fig. 28. The defect modes in this lattice presents a resonant mode that is not linked to a transparency point. This resonant mode was shown in the previous figures as a peak on the intensity between the second and third peaks of the transmission in figures 22(d), 23(d) and 24(d). This resonant mode merges with the full transparency point mode for a specific value of nonlinear power and defect layer size, forming a pattern reminding a fork (as shown if fig.
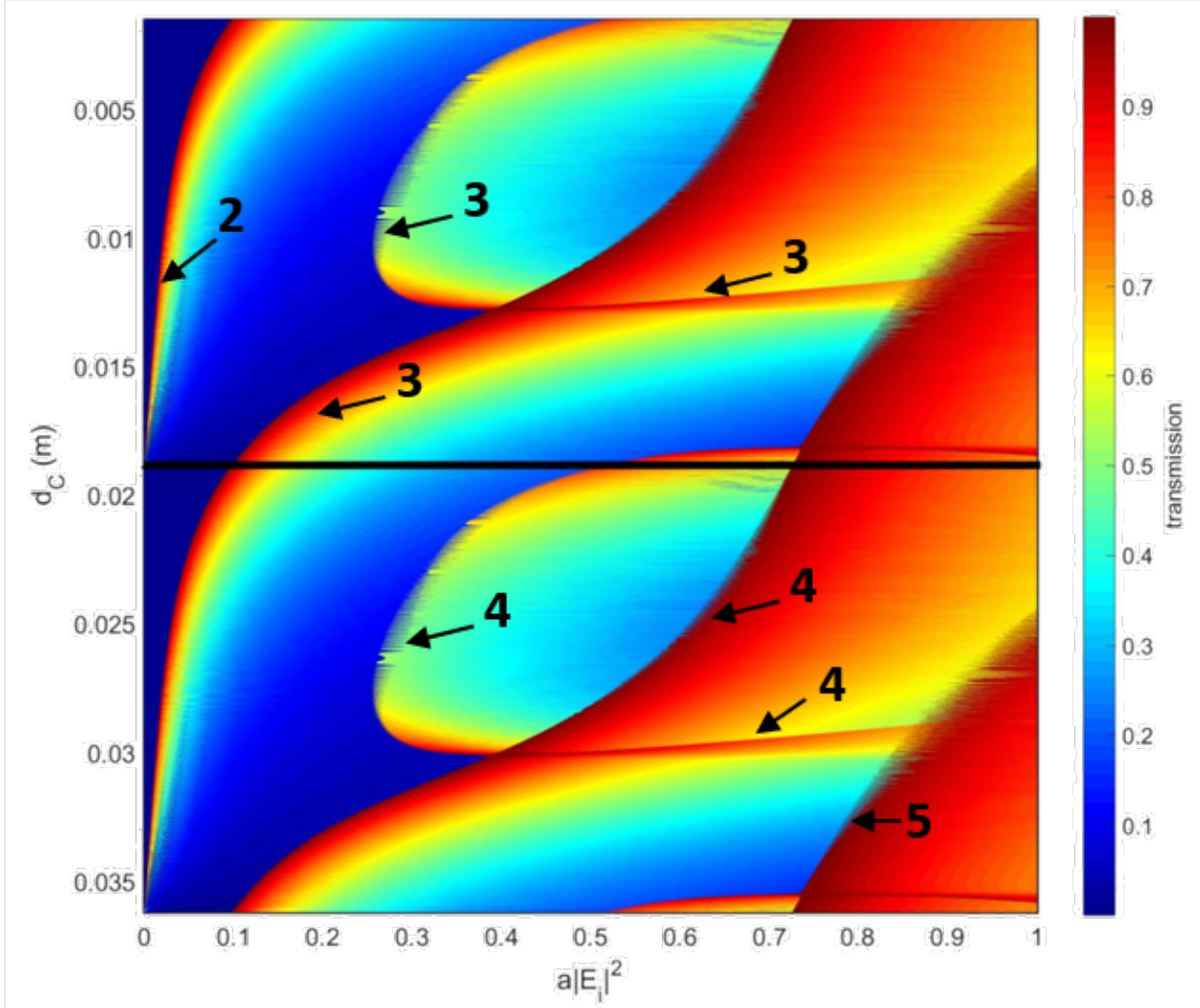
Figure 27 – Transmission as a function of nonlinear power and defect layer size. The black line indicates the defect mode ($d_C = 0.018$ m) encountered in the linear problem. Each transparency curve (in red) corresponds to a n-peak electric profile solution, as indicated by the arrows (where the number in the top of each arrow corresponds to the n in the n-peak electric profile).

28). This behavior is repeated for every defect mode, and this fork appears twice for each resonant mode (for the 4 electric field profile mode one can see one fork around $d_C = 0.03$ m and another one for $d_C = 0.019$ m. As of now, we have no explanation for this fork shape, nor for the merging (or splitting) behavior.

We proceed to study the behavior of one the transmission for a specific value of defect layer size ($d_C = 0.014$ m), varying frequency and nonlinear power (fig. 29). Figure 29 shows that the defect mode is excited for smaller frequencies as one increases the nonlinear power, and vanishes at a specific value of frequency ($\nu = 5.07$ GHz, corresponding to the defect mode observed in the linear regime).

In conclusion, we have observed that a strip consisted of a regular right handed
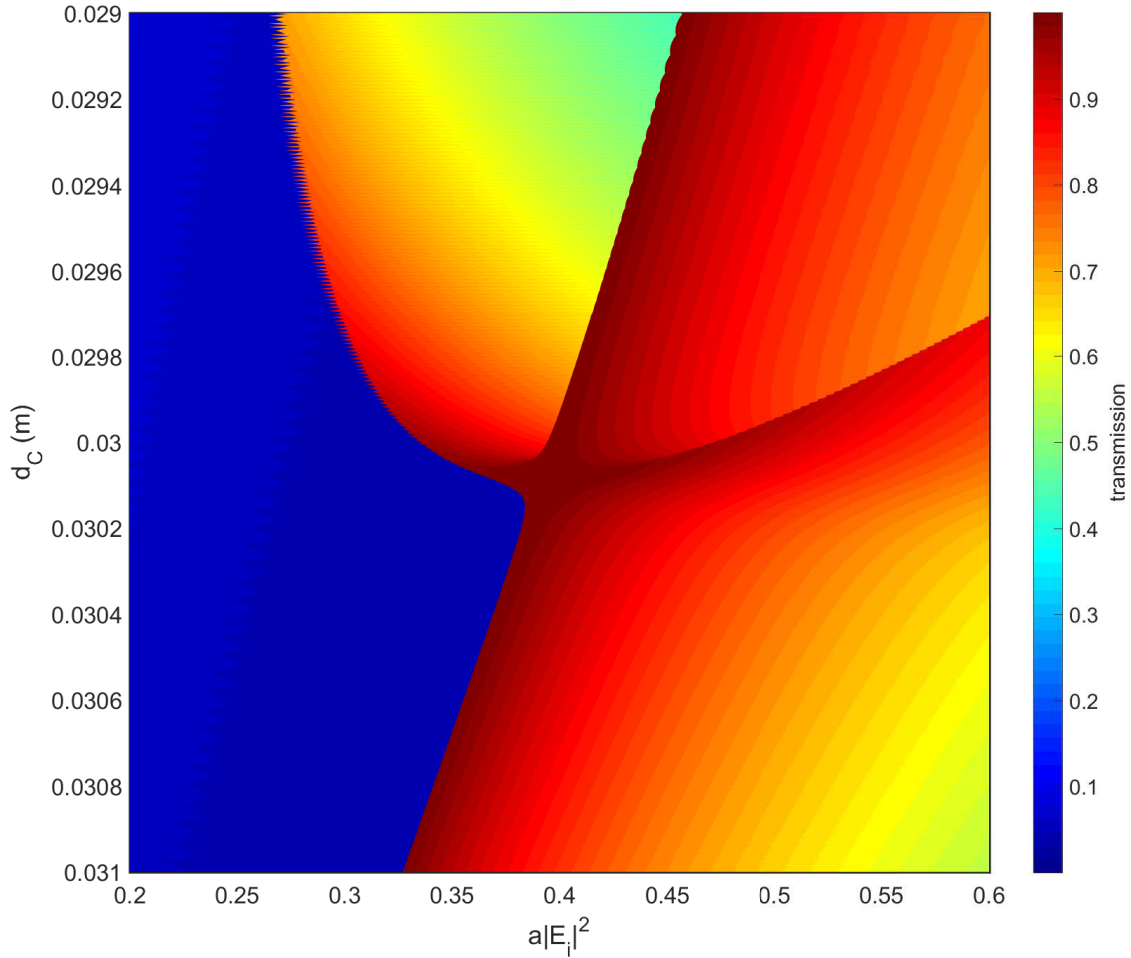
Figure 28 – Detail of the fork like curve obtained for all the *n*-peak electric profile solutions of the system discussed in figure 27.

material (RHM) sandwiched between bilayers Kerr/metamaterial presents somewhat similar results in the nonlinear and linear regime. In the linear regime, there are several transparency states (defect modes) of the system that are periodic with the size of the RHM layer size. By studying consecutive defect modes of the system, one observes parity switch and an increase in the number of peaks in the electric profile of that mode. Furthermore, a focusing nonlinearity excites finite transparency points that presents a similar behavior. Consecutive resonant modes in the nonlinear power presents parity switch and an increase in the number of peaks in the electric filed profile of that mode. Moreover, we believe that the results outlined here are still present when the number of bilayers embedding the RHM layer is increased.
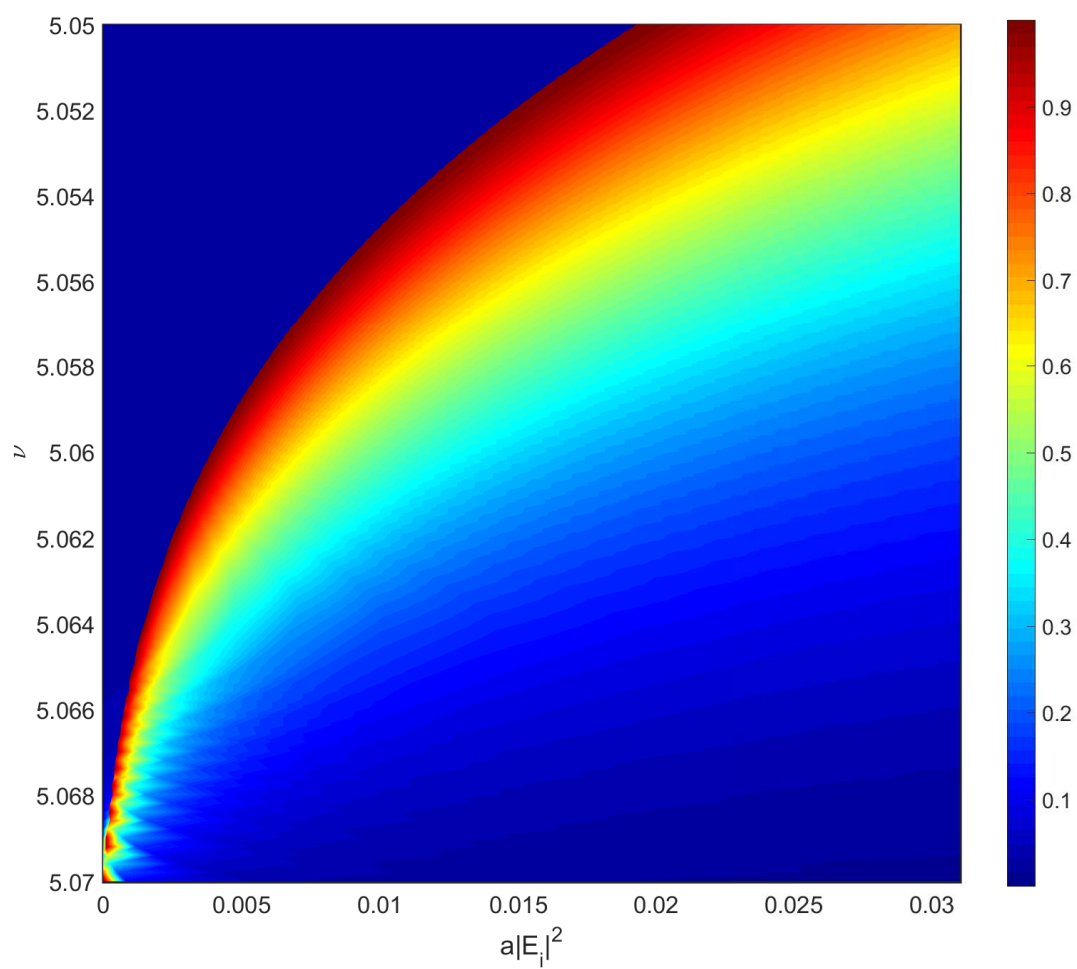
Figure 29 – Transmission as a function of frequency and nonlienar power for a fixed value of defect layer size $d_C = 0.014$ m.

8 Gap soliton transparency switch in one-dimensional Kerr-metamaterial superlattices

8.1 Kerr-Metamaterial superlattice

The geometry of the problem discussed in this chapter is shown in fig. 30, where the z-direction is chosen as the stacking direction of the lattice. The heterostructure, with length L, is sandwiched between vacuum on the left and right side, and is composed of $N = 32$ unit cells AB formed by a Kerr medium (layers A) and a metamaterial (layers B) whose widths are $d_A = 10$ mm and $d_B = 10$ mm, respectively. In this study, layers A are characterized by a magnetic permeability μ_A and an electric permittivity $\epsilon_A = \epsilon_A^0 + a|E|^2$, where $E = E(z)$ is the electric-field amplitude of the electromagnetic field inside the superlattice. The slabs B are characterized by a metamaterial with magnetic permeability and electric permittivity defined as in (HEGDE; WINFUL, 2005a):

$$\epsilon_B = 1.6 + \frac{40}{0.81 - \nu^2 - i\nu\gamma} \tag{8.1}$$

$$\mu_B = 1.0 + \frac{25}{0.814 - \nu^2 - i\nu\gamma} \tag{8.2}$$

where ν is the frequency in GHz and γ accounts for absorption. Despite having the possibility of choosing any desired absorption in the metamaterial considered, we set $\gamma = 0$ as a first approximation.

The PP-gap, the one we are most interested in, and the zero-$< n >$ gap have already been proved to exist in any frequency range. We choose materials with GHz plasma frequency because it is the easier to find in the literature for materials achieving negative refraction. Even a naturally occurring material was proved to have a negative refraction response in the GHz regime (PIMENOV et al., 2007). Nonlinear materials are also reported in the literature, for example Shih et al. (SHIH et al., 1990) measured n_2 (the nonlinear index of refraction) equal to 2.6×10^{-4} at 94 GHz in a liquid suspension of elongated microparticles. The advances in the construction of plasmonic materials has also boosted the values of n_2 and we believe that the materials proposed here are possible to be reproduced in an experiment.

We begin by discussing the transmission of the heterostructure in the absence of absorption ($\gamma = 0$) and nonlinearity ($a = 0$). In Figs. 31(a) and (d) we show the transmission as a function of the incoming wave frequency for normal incidence ($\theta = 0$) and oblique incidence ($\theta = \pi/24$), respectively. The first band gap one sees is the gap -
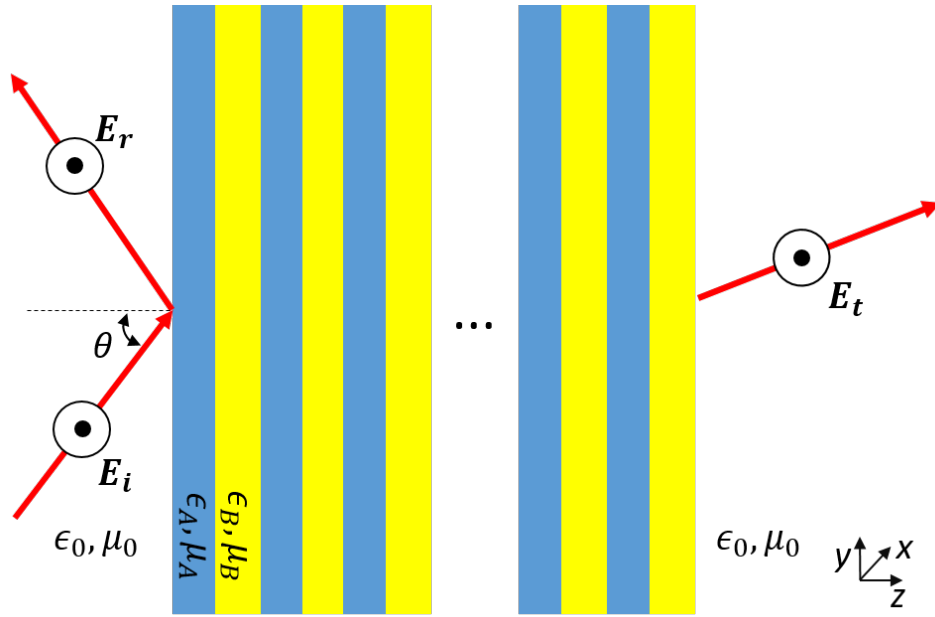
Figure 30 – Pictorial view of the z-growth photonic superlattice with A and B alternated layers in a periodic arrangement, for TE-like incident electromagnetic waves. The following parameters were chosen: both layers have the same size $a = b = 10$ mm; for the linear RHM layer $\epsilon_A^0 = \epsilon_A = 2, \mu_A = 1$, and, for the linear LHM, the parameters are the same as given by Eqs. (8.1) and (8.2).

$< n >= 0$, a photonic band bag corresponding to zero volume averaged refractive index. This gap was first discovered by Li in 2003 (LI et al., 2003). In their paper they show that this gap only exists in structures composed of materials with both positive refractive index and negative refractive index. The gap is inherently different from the Bragg gaps, as it is invariant with respect to the length scale and insensitive to randomness of the lattice (as long the averaged volume refractive index continues to be zero). For the lattice we are working with, described in fig. 30, the gap appears around $\nu = 3.5518$ GHz (both for oblique and normal incidence, as shown in figs. 31(a) and (d)), as the average value of the refractive index is 0 for this frequency because $n_A = 1.4142$ and $n_B = -1.4142$, and both materials slabs have the same size (eq.3.57).

When the magnetic permeability is given by eq. 8.2 and an electromagnetic wave of the form $e^{i(\omega t - \mathbf{k} \cdot \mathbf{r})}$ travels to it the electromagnetic wave induces a magnetization on the medium that modifies itself, coupling the electromagnetic wave with the medium. This is a hybrid mode, as it is the result of the interaction of the electromagnetic wave with the medium (the electromagnetic wave excites a plasmonic mode inside the medium that strongly interacts with the light beam). There is no longer a pure plasma wave or a pure electromagnetic wave inside the material, the dispersion relation is a mixture of the two. The strong interaction of the plasma wave with the light results in the bulk plasmon polariton. The second band gap we see only shows itself in fig. 31(d) when the incidence is oblique. When the frequency is near ν_m^p, the bulk-like longitudinal plasmon frequency
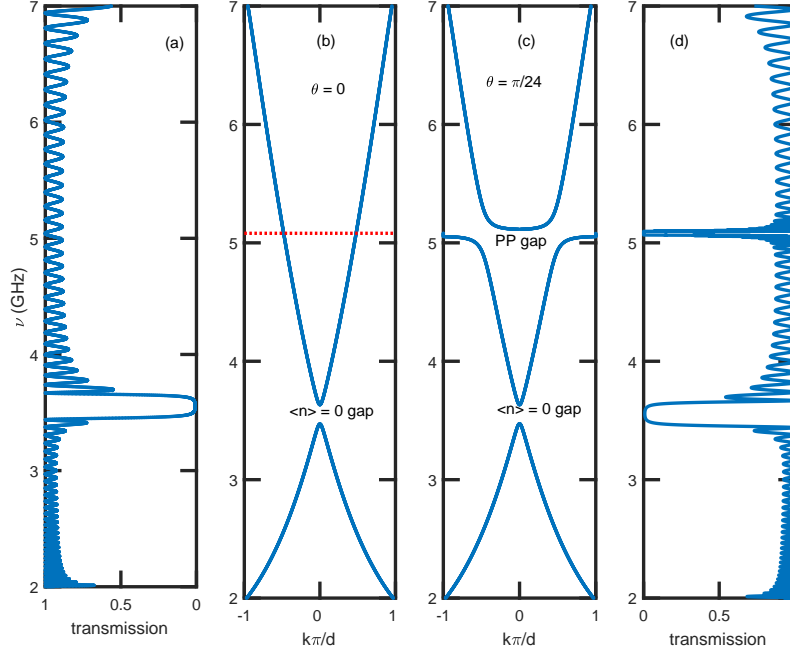
Figure 31 – Transmission coefficient as a function of the wave frequency in a heterostructure composed of 32 AB layers in the absence of absorption and nonlinearity ($\gamma = 0$ and $a = 0$ respectively), for (a) normal, $\theta = 0$, and (d) TE oblique incidence, $\theta = \pi/24$. Panels (b) and (c) depict the dispersion relation corresponding to the infinite heterostructure for normal ($\theta = 0$) and oblique ($\theta = \pi/24$) incidence, respectively. The following parameters were chosen: for the linear RHM layer $\epsilon_A^0 = \epsilon_A = 2, \mu_A = 1$, and, for the linear LHM, the parameters are the same as given by Eqs. (8.1) and (8.2). In panel (b) we also indicate by a dotted line the $\nu_m^p = 5.08$ GHz bulk-like longitudinal magnetic plasmon frequency.

($\mu_B = 0$ at $\nu = \nu_m^p = 5.0807$ GHz), there is a region of zero-transmittance when treating the case of oblique incidence, the plasmon-polariton (PP) gap. In a TE configuration, and for oblique incidence, there is a component of the magnetic field in the direction of the stratification, which couples to the bulk-like longitudinal magnetic plasmon mode, giving origin to the PP gap (CARVALHO et al., 2011), (REYES-GÓMEZ et al., 2009), the zero-transmittance region around ν_m^p.

We also plot the dispersion relation for an infinite-layered system (Figs. 31(b) and (c)), and one may observe that the PP gap opens up around the magnetic plasmon frequency ν_m^p for the case of oblique incidence, predicting the behavior of the finite superlattice used in Fig. 31(c). It should be noted that the system studied in this work ($N = 32$) also shows good agreement with the infinite-layered superlattice (Figs. 31(b) and (c)) with respect to the zero-n gap.
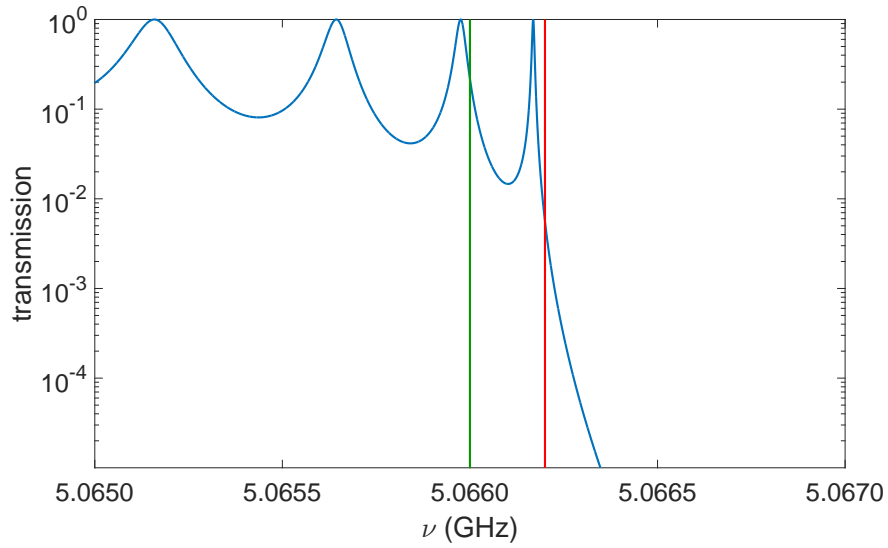
Figure 32 – Transmission through the same structure and linear parameters as in Fig 31, for $\theta = \pi/24$, in the case of TE incidence in the vicinity of the lower edge of the PP gap. The red vertical line is at $\nu = 5.0662$ GHz, for which $T \approx 0.0056$, and the green vertical line is at $\nu = 5.0660$ GHz, for which $T \approx 0.2174$.

8.2 PP gap solitons
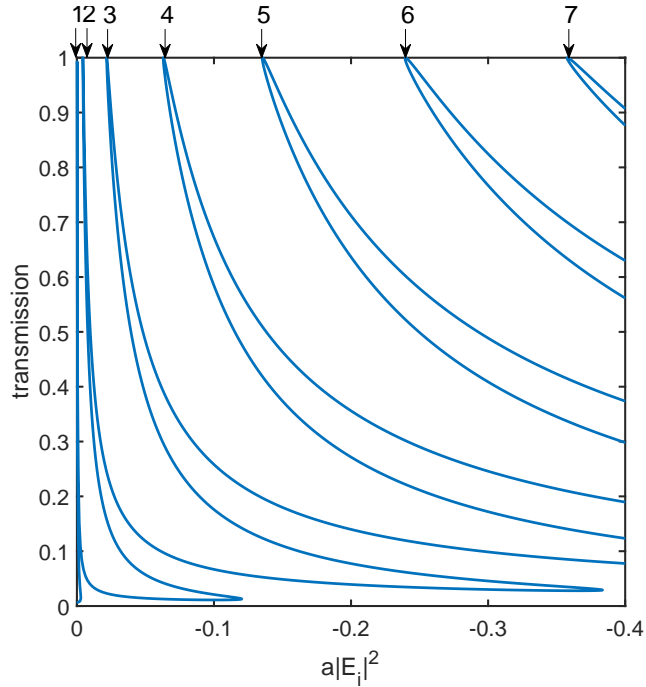
Figure 33 – Transmission as a function of increasing power of a defocusing nonlinearity for $\theta = \pi/24$ in the case of TE incidence. We show several transparency (transmission $T = 1$) points for $\nu = 5.0662$ GHz, for values (see arrows) of $a|E_i|^2$ equal to $-0.0002, -0.0044, -0.022, -0.063, -0.1354, -0.2397$ and -0.3579. The results were calculated for the same structure and linear parameters as in Fig 31.
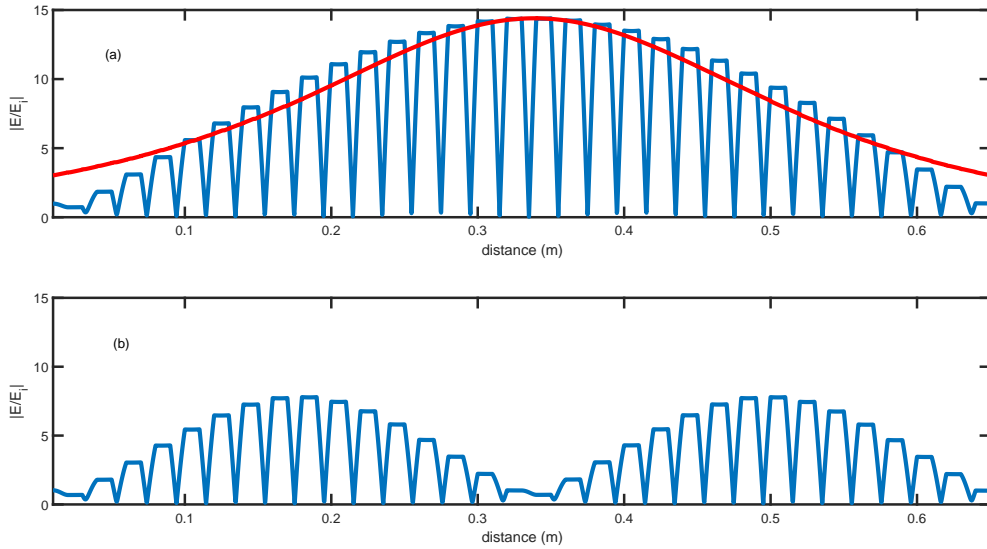
Figure 34 – Spatial profile for the electric field for $\theta = \pi/24$ and $\nu = 0.5662$ GHz in the case of TE incidence. Figure (a) shows that $a|E_i|^2$ equal to -0.0002, the first arrow in fig. 33, corresponds to the one-soliton mode. Similarly, (b) shows that $a|E_i|^2$ equal to -0.0044, the second arrow in fig. 33, corresponds to the two-soliton mode. Also, we illustrated in (a), the red line, the fitting of a one-soliton mode envelope to a sech(αz) function (α being a fitting parametter).

We now proceed to study the influence of the nonlinearity in the properties of the lattice described in fig. 30, specifically on the behavior of the transmission and the electromagnetic field profile inside the lattice. To do so, we will analyze these quantities when submitted to different values of the nonlinear power $a|E_i|^2$. In Fig. 32 we plot the transmission of the structure for $\theta = \pi/24$ at the lower edge of the PP gap and absence of nonlinearity ($a = 0$). Before swiping all the frequencies around the band gap lets choose two frequencies to get an idea of how a defocusing nonlinearity affects the transmission of the system. As a starting point we choose $\nu = 5.0660$ GHz and $\nu = 5.0662$ GHz and study the influence of a defocusing nonlinearity ($a < 0$) on the electric field profile inside the structure and in its transmission properties. For $\nu = 5.0662$ GHz one finds $T \approx 0.0056$ when $a = 0$. A defocusing nonlinearity gives rise to a multistable behavior of the transmission (Fig. 33) and there are seven transparency ($T = 1$) points in the nonlinear power range shown. Specifically, one obtains $T = 1$ when $a|E_i|^2 = -0.0002, -0.0044, -0.022, -0.063, -0.1354, -0.2397, -0.3579$. In Fig. 34 we plot the spatial profile for the electric field for $a|E_i|^2 = -0.0002$ (a) and $a|E_i|^2 = -0.0044$ (b) revealing that the transparency points are connected to stable branches of the electric field. In addition, the envelope function of the one mode branch is fitted accurately by the function $f(x) = E^M(\text{sech } \alpha x)$ (as seen in 34(a)), where E^M is the maximum value of E and α is a fitting parameter, which suggests that these modes mimic the behavior of true

Figure 35 – Spatial profile for the electric field versus the nonlinear power, with $\nu = 5.0662$ GHz. Outlined in black and highlighted by the arrows are the places where full transparency is found (T=1). There are (see arrows) one-soliton, two-soliton and three-soliton modes in the nonlinear power range shown that corresponds to the arrows shown in Fig. 33. The results were calculated for the same structure and linear parameters as in Fig 31.

solitons despite being located in finite lattices, as commented by Chen (CHEN; MILLS, 1987).

In fig. 35 we plot the spatial profile for the electric field versus the nonlinear power, revealing that each transparency point is connected to a stable branch of the electric field, as shown by the arrows. One might find strange that the nonlinear power range shown in this figure is significantly smaller than in fig. 33. The cutoff in the nonlinear power axis happens because as the nonlinear power increases, the maximum value of the electric field gets smaller. Thus, the graphic tends to get a very high contrast in its height, making almost impossible to spot in it the profiles corresponding to the higher order soliton-like modes. For example: the one mode branch has a maximum value of $|E/E_i|$ of 15, while the four mode branch has a maximum value of 0.1. Thus, it's better to visualize a small range of the nonlinear power than to visualize a big range. In addition, the behavior is repeated, each transparency point is connected to a n-mode branch of the electric field, where n is the position of the peak. Figure 34 can be seen as slices of the surface showed in 35, specifically arrows 1 and 2 correspond to Figs. 35 (a) and (b), respectively.

For $\nu = 5.0660$ GHz we have $T \approx 0.2174$ when $a = 0$ and Fig. 36 shows that
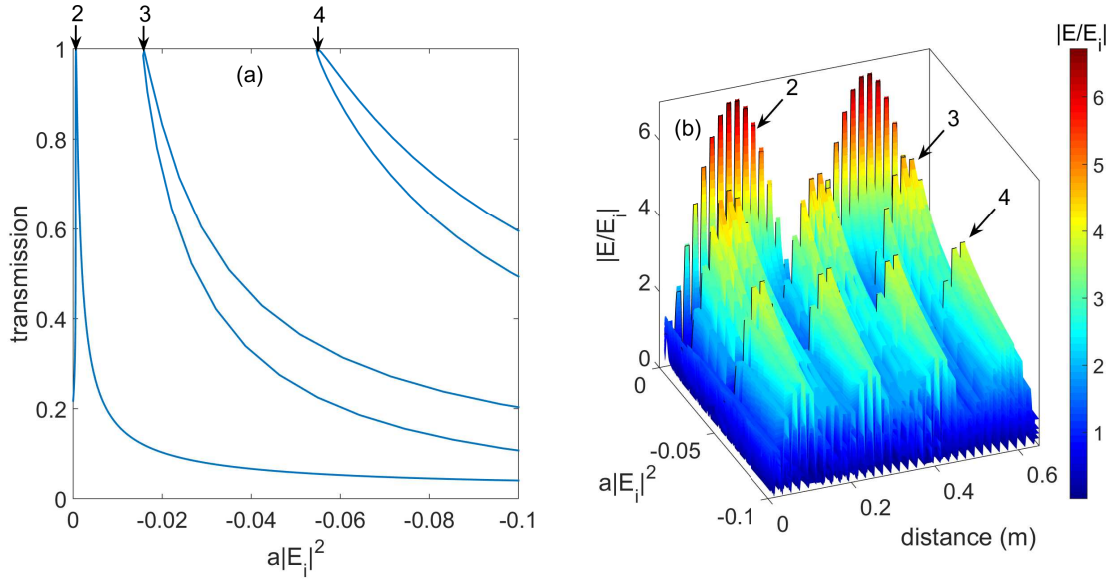
Figure 36 – Calculated results for the same structure and linear parameters as in Fig 31:
(a) Transmission as a function of increasing power of a defocusing nonlinearity
for $\theta = \pi/24$ in the case of TE incidence. We show several transparency
(transmission $T = 1$) points for $\nu = 5.0660$ GHz, for values (see arrows)
of $a|E_i|^2$ equal to $-0.00062, -0.016$ and -0.055; (b) Corresponding spatial
profile for the electric field versus the nonlinear power, with $\nu = 5.0660$ GHz.
Outlined in black and highlighted by the arrows are the places where full
transparency is found (T=1). There are (see arrows) two-soliton, three-soliton
and four-soliton modes in the nonlinear power range shown.

the nonlinearity creates three transparency points in the nonlinear power range shown
$(a|E_i|^2 = -0.00062, -0.016, -0.055)$. The electric field versus the nonlinear power plot
[cf. Fig. 36(b)] shows that each transparency point is connected to a stable branch of the
electric field, as shown by the arrows, the same behavior encountered for $\nu = 5.06624$
GHz. However, there is no one-mode soliton branch for this frequency, i.e, no value of
the nonlinear power, for a defocusing nonlinearity, is associated with a one-soliton like
profile of the electric field. This stems from the fact that as we consider smaller frequencies,
driving away from the PP gap lower frequency edge, in the nonlinear regime, the otherwise
stable soliton-like modes disappear. There is a cut-off frequency value ν_1 below which
there is no fundamental soliton mode and the same occurs for each of the n-soliton modes
observed, as they disappear for frequencies smaller than ν_n. In Fig. 37(b) we plot the
transmission as a function of the nonlinear power and frequency, to illustrate this fact.
Each $T = 1$ curve is associated with a n-soliton like mode, where n is outlined by numbers
and arrows. Note that these curves appear around the edge of the PP gap and vanish for
specific values ν_n of the frequency. Figure 37(a) shows the same data as 37(b) but viewed
from a different angle, showing that even these plots are capable of accounting for the
whole behavior of the system (showing multistability and transparency switching).
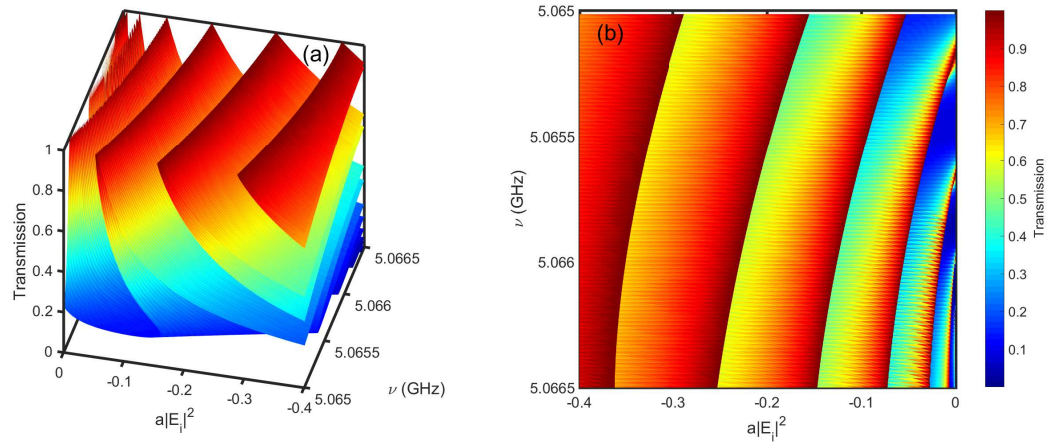
Figure 37 – Color plot of the transmission coefficient for different values of the nonlinear power and frequencies in the vicinity of the lower edge of the PP gap, for the system considered in Fig. 31, and $\theta = \pi/24$ in the TE configuration. (a) A view of the full plot in a tilted angle, showing that the multistability is still found, even for frequencies far away of the PP gap. (b) The same plot as (a) but viewed from the top. In red are the regions where we find transparency and soliton modes (see arrows). The n = 1,2,...,7 arrow numbers indicate the n-soliton modes in the nonlinear power range shown.
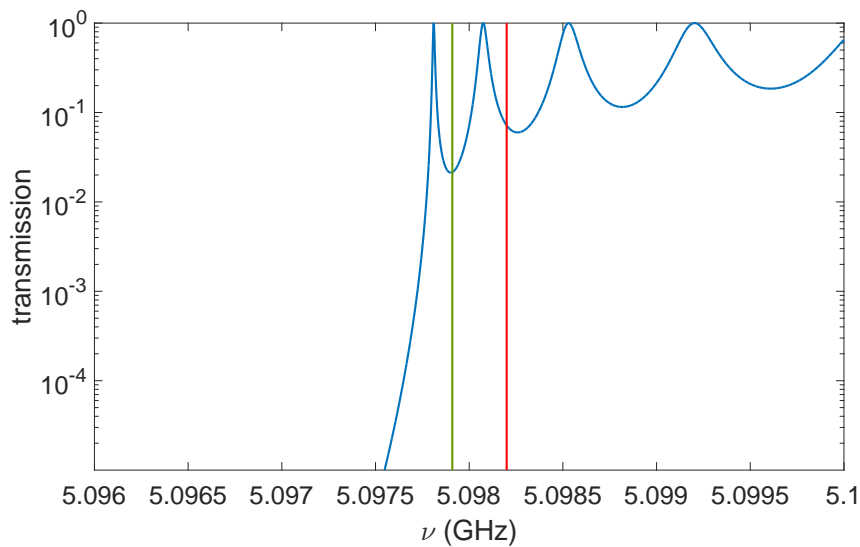
Figure 38 – TE Transmission through the same structure and linear parameter as in Fig 31, for $\theta = \pi/24$, and for frequencies in the vicinity of the top edge of the PP gap. The green vertical line is at $\nu = 5.09820$ GHz, for which $T \approx 0.07$, and the red vertical line is at $\nu = 5.09791$ GHz, for which $T \approx 0.02$.
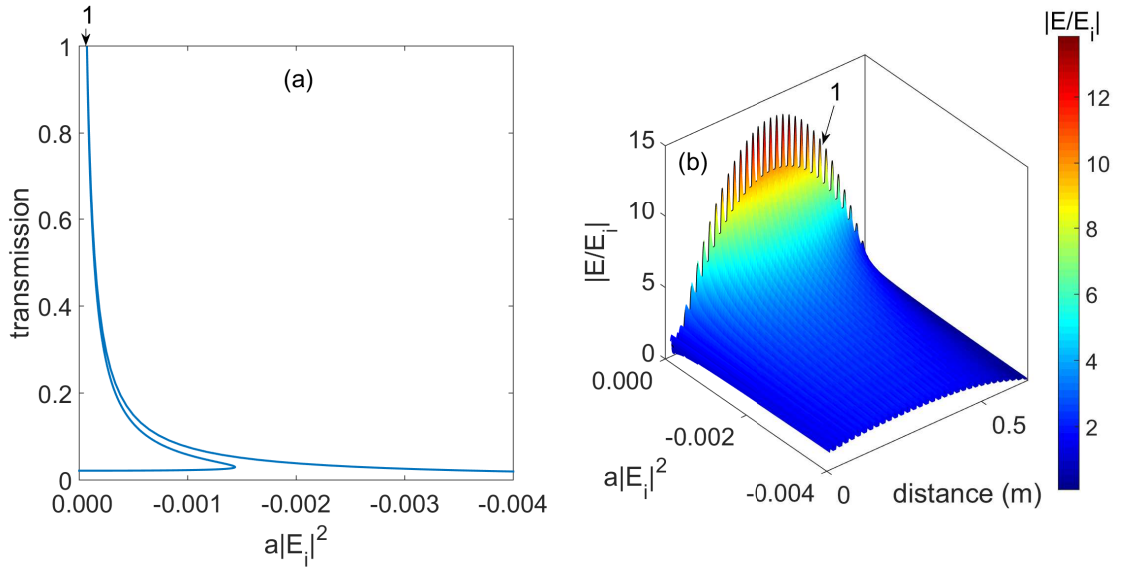
Figure 39 – Calculated results for the same structure and linear parameters as in Fig 31: (a) Transmission as a function of increasing power of a defocusing nonlinearity for $\theta = \pi/24$ in the case of TE incidence. Only one transparency ($T = 1$) point is found for $\nu = 5.09791$ GHz, at a value of $a|E_i|^2$ (see arrow) equal to -0.00007; (b) Correspond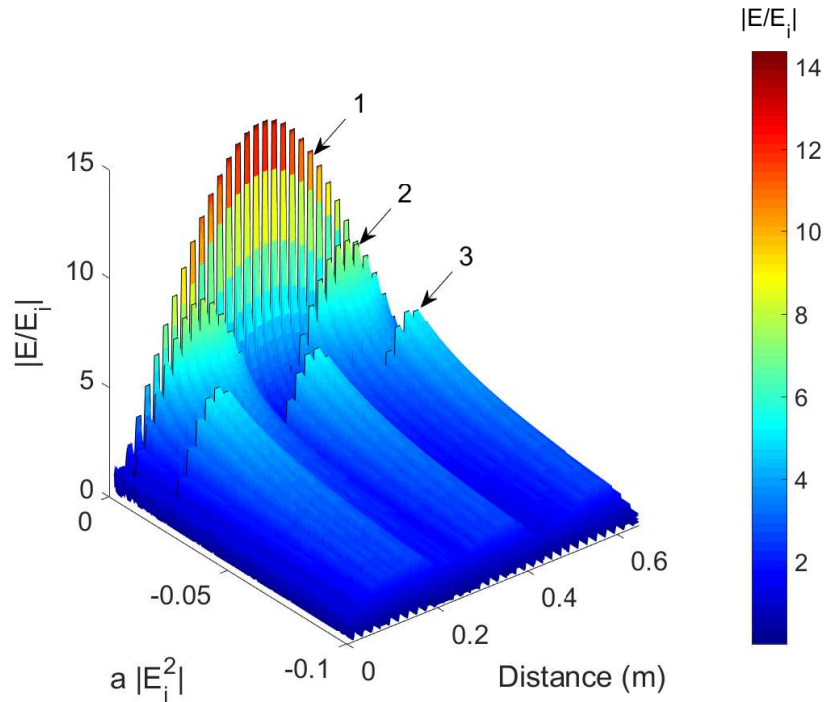ing spatial profile for the electric field versus the nonlinear power. Outlined in black and highlighted by the arrow is the place where full transparency is found ($T = 1$), at a value of $a|E_i|^2$ equal to -0.00007. There are (see arrow) only one-soliton like modes in the nonlinear power range shown.
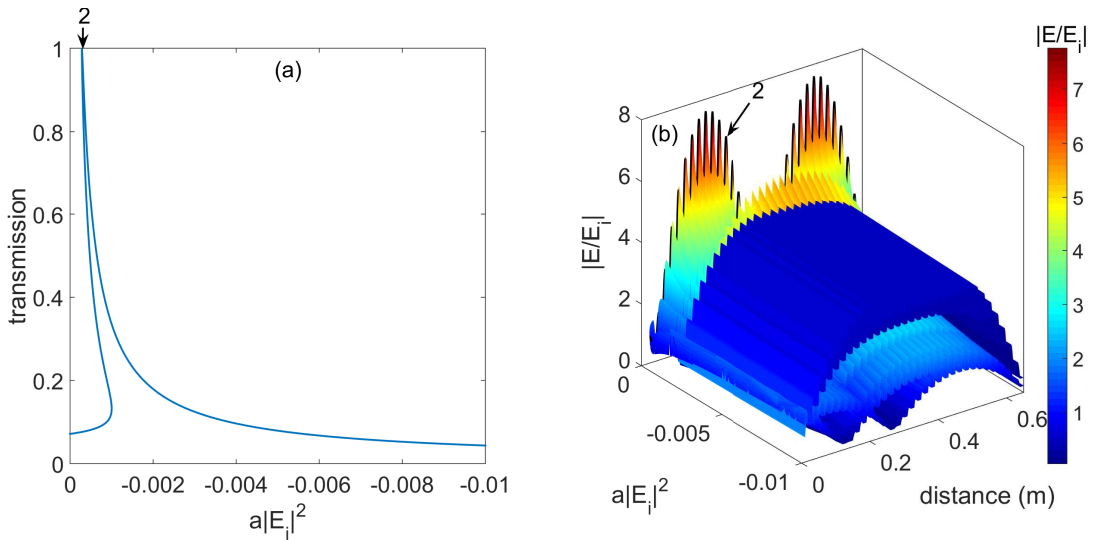
Figure 40 – (Color online) Calculated results for the same structure and linear parameters as in Fig 31: (a) Transmission as a function of increasing power of a defocusing nonlinearity for $\theta = \pi/24$ in the case of TE incidence. Only one transparency ($T = 1$) point is found for $\nu = 5.0982$ GHz, at a value of $a|E_i|^2$ (see arrow) equal to -0.00028.; (b) Corresponding spatial profile for the electric field for the two-soliton like mode.
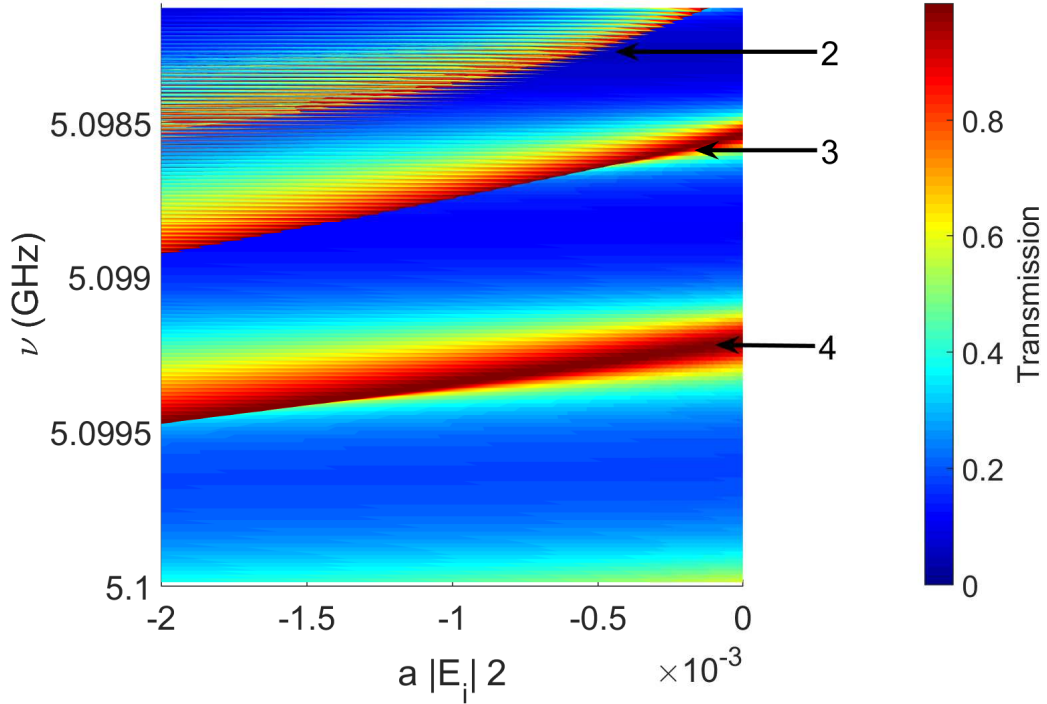
Figure 41 – Color plot of the transmission coefficient for different values of the nonlinear power and frequencies in the vicinity of the top edge of the PP gap, for the system considered in Fig. 31, with $\theta = \pi/24$ and TE incidence. In red are the regions where we find transparency and soliton modes (see arrows). The n = 2,3,4 arrow numbers indicate the n-soliton modes in the nonlinear power range shown.

We proceed by extending the study to the top edge of the TE PP gap, turning to Fig. 38 which shows the transmission as a function of the incident frequency when there is no nonlinearity ($a = 0$), with $\theta = \pi/24$. We choose two frequency points ($\nu = 5.0982$ GHz, 5.09791 GHz) to observe the effects of an increasing defocusing nonlinearity in the transmission properties and electric field profiles inside the structure. The effects on the transmission properties due to a defocusing nonlinearity are depicted in Figs. 39(a) and 40(a), for $\nu = 5.09791$ GHz and $\nu = 5.0982$ GHz, respectively. Transparency switching is observed for both frequencies but while for $\nu = 5.09791$ GHz the first transparency point is associated with the one-soliton mode [cf. Fig. 39(a)], we observe that the first transparency point for $\nu = 5.0982$ GHz is associated with a two-soliton mode and no one-soliton mode is observed for this frequency. As shown before for frequencies near the lower edge of the PP gap, Fig. 41 indicates that by choosing frequencies deviating from the top edge of the PP gap, the $T = 1$ curves associated with the n-soliton branch (as illustrated by the arrows) vanish for a frequency ν_n. However, the behavior of the system is dramatically different when comparing the transmission around the lower edge or top edge of the PP gap, as shown in Fig. 42. The top PP gap edge moves to higher frequencies as the nonlinear power
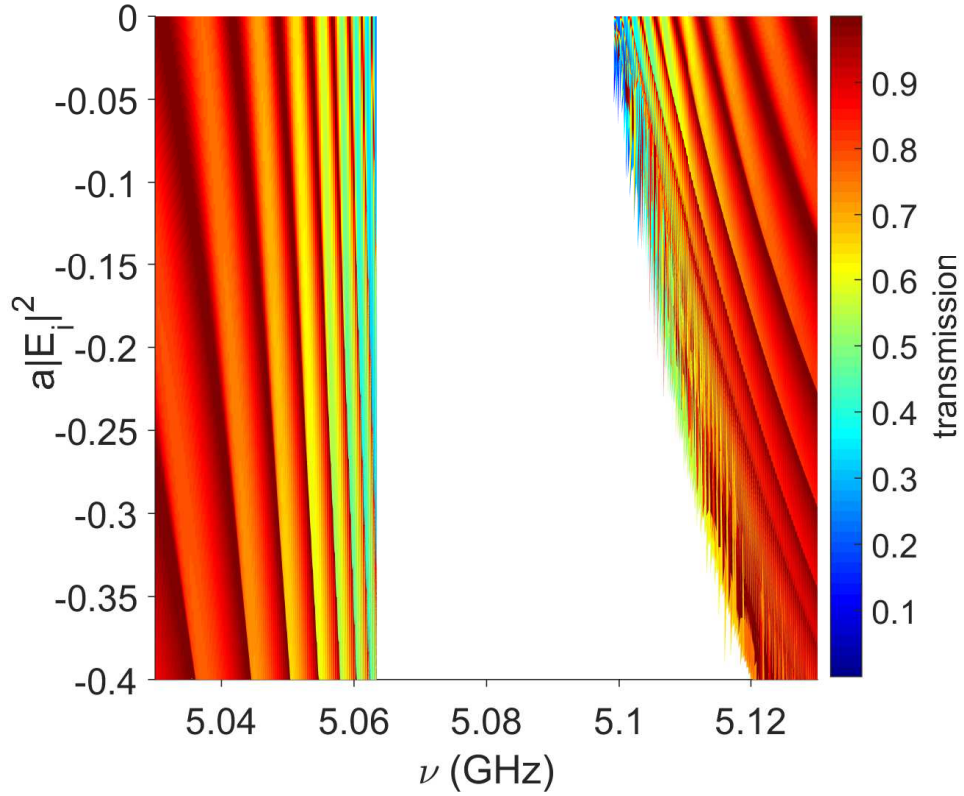
Figure 42 – Color plot for the transmission coefficient for different values of nonlinear power and frequency for the system considered in Fig. 31, for $\theta = \pi/24$ and TE incidence. For greater clarity, the $T = 0$ gap region is shown in white.

increases whereas the bottom PP edge remains essentially unchanged and, therefore, the 'nonlinear gap' becomes larger with increasing self-defocusing nonlinearity. We suspect that the reason for this interesting phenomenon to be due to a combination of the Kerr material and the dispersive metamaterial. If we overlook the spatial variation of the light intensity inside the nonlinear slabs, we can define an average permittivity for the nonlinear slabs as $\bar{\epsilon}_B = 2 + a|\bar{E}|^2$, where $\bar{E}$ is the average value of the electric field inside the slab. A defocusing nonlinearity would then reduce the permittivity of the Kerr material, decreasing its refractive index. The resulting system would have a smaller optical path and a smaller average refractive index. Then, we can compare the nonlinear system with a linear one where the permittivity of the layers B are getting smaller. If one define layers B to have ordinary values permittivity and permeability and use layers A as before (given by eqs. 8.1 and 8.2), we can plot the transmission properties of this system for varying frequency and varying permittivity of layers B (fig. 43). This shows excellent agreement with our nonlinear system, showing that our analogy is, at least, in the right path. While the top edge of the PP gap shifts to higher frequencies, the bottom edge of the PP gap can not do the same because the PP gap is not a property of the lattice, it is a property of the
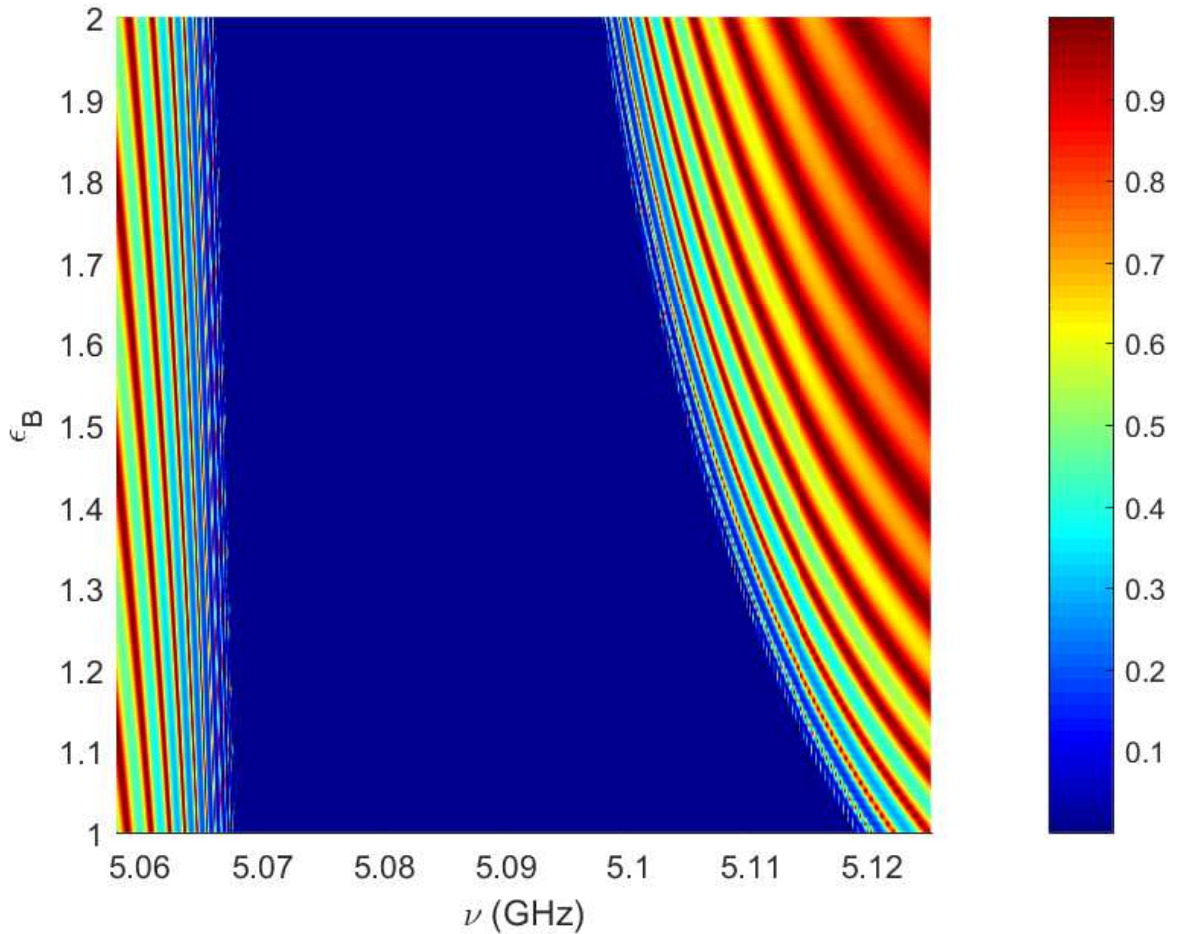
Figure 43 – Color plot of the transmission for a system described as in fig. 30, but with $a = 0$. We vary the values of the permittivity of layers B to compare the effects of a defocusing nonlinearity in the system, to the effects of a varying permittivity in a linear system.

dispersive plasmonic metamaterial. The plasmonic metamaterial induces a plasma wave inside itself that blocks the flow of light. Thus, a shift of the bottom edge of the PP gap to higher frequencies is not allowed due to the plasmonic material, making the bottom edge of the PP-gap independent of the intensity of the field (for a defocusing nonlinearity).

The line of thought used to explain the different behavior between the top and bottom edges of the PP gap, predicts that the bottom and top edge of the PP gap for a focusing nonlinearity will behave in a similar manner. The top edge would remain pratically constant due to the plasmonic material, while the bottom edge would shift to smaller frequencies. The linear analog is showed in fig. 44. Despite having its linear counterpart, to simulate the nonlinear problem with the focusing nonlinearity is still a challenge. The transmission as a function of a focusing nonlinearity needs more than 1 million points per frequency value to have a continuous representation, add to this the lack of an adaptive
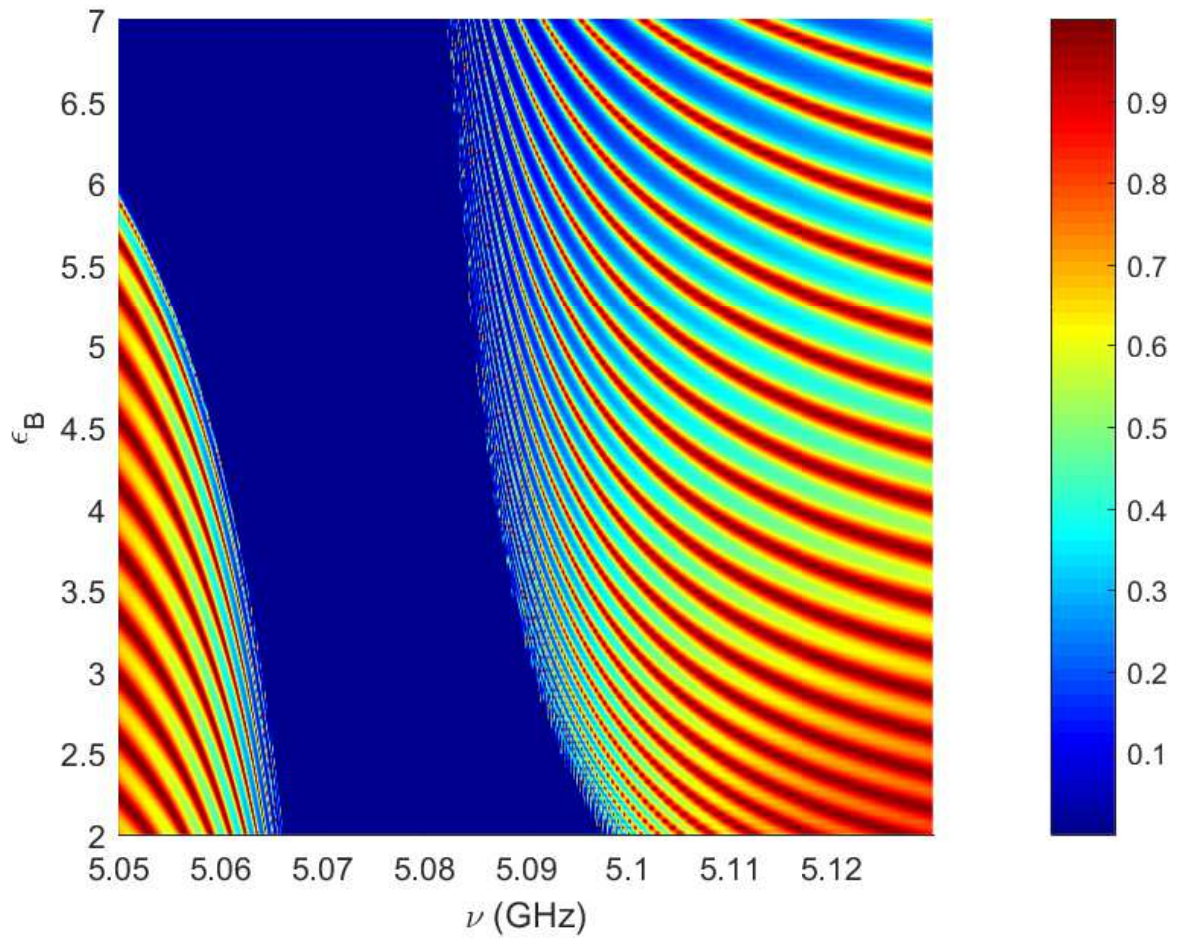
Figure 44 – Color plot of the transmission for a system described as in fig. 30, but with $a = 0$. We vary the values of the permittivity of layers B to compare the effects of a focusing nonlinearity in the system, to the effects of a varying permittivity in a linear system.

algorithm to increase the values of nonlinear power continuously and the problem gets even more computationally intensive. Further work is necessary to address this problem.

9 Conclusions

In summary, we have presented a detailed study on the nonlinear transmission switching phenomenon in 1D Kerr/metamaterial heterostructures in the vicinities of both top and bottom edges of the PP-gap under the influence of a self-defocusing Kerr nonlinearity. Moreover, we also theoretically analyzed the defect modes of a photonic strip composed of a regular nondispersive RHM sandwiched by two Kerr/dispersive metamaterial bilayers for frequencies in the edges of the PP-gap in the linear and nonlinear regime.

As expected, in the study of the superlattice without defects, we find multi stability, and resonant n-soliton modes. By sweeping the frequency regions around the edges of the PP gap where the linear dispersion relation exhibits a plasmon-polariton coupling, we find a different behavior depending on whether the frequency range belongs to the top or bottom edge of the PP gap. The top edge of the gap is shifted to higher frequencies for higher nonlinearities, while the bottom edge remains unchanged. We have found cut-off frequency values ν_n below which there are no n-soliton modes. Furthermore, we find that the depart from the resonant ($T = 1$) transmission frequencies does not hinder soliton formation, although the detuned solitons exhibit smaller amplitudes. Finally, we also presented a physical argument to explain the differences in behavior of the gap edges with an increasing nonlinearity, linking the nonlinear system to a linear one (making a parallel between the nonlinearity to a varying permittivity), and explaining why the bottom edge of the PP-gap is unaffected by the defocusing nonlinearity (stemming from the material properties of the layers rather than an emerging property of the photonic structure). Finally, we would like to point out that, in all cases studied in the present work, the transparency-switching phenomenon is still observable at low levels of loss and absorption in the heterostructure.

The defect modes were also meticulously characterized. A link between the transmission and electric field profile properties exhibited when increasing the defect layer size in the linear regime and an increasing focusing nonlinearity was established. We also find transparency switching, hysteresis and multistable behavior, as it is expected in lattices with a focusing Kerr nonlinearity. Moreover, we also find parity switch and an increase in the number of peaks of the electric field profile for consecutive defect/resonant modes (in the linear and nonlinear regime). We found that every value of defect layer size has a defect mode linked to it in the nonlinear regime.

The metamaterials and Kerr materials presented are justified recent by investigations on the experimental fabrication of gain-enhanced metamaterials, which may open new perspectives to overcome high levels of absorption (PUSCH et al., 2012; HESS et al., 2012).

Thus, we hope that the present theoretical results will be of interest in future experimental work on nonlinear-heterostructure systems. Moreover, the study presented here can be easily replicated to characterize the zero-$< n >$ gap and the Bragg gap (for defect modes and gap-soliton formation), making these straightforward future works. However, despite having the mathematical formulation laid out completely, a computational problem arises for some systems where the transmission becomes a very rapidly function of nonlinear power. In general, this problem arises when treating focusing nonlinearities near gap edges, which require a greater refinement of the nonlinear power for these frequencies (which makes the problem more computationally intensive). A refined version of the adaptive algorithm cited in chapter 6 has to be developed to better address this problem, so that we can verify our conjecture on the nonlinear system and its linear counterpart.

Bibliography

ACEVES, A.; WABNITZ, S. Self-induced transparency solitons in nonlinear refractive periodic media. *Physics Letters A*, Elsevier, v. 141, n. 1-2, p. 37–42, 1989. Cited in page 54.

ACEVES, A. B. Optical gap solitons: Past, present, and future; theory and experiments. *Chaos: An Interdisciplinary Journal of Nonlinear Science*, AIP, v. 10, n. 3, p. 584–589, 2000. Cited in page 54.

ARGYROPOULOS, C. et al. Boosting optical nonlinearities in ε-near-zero plasmonic channels. *Physical Review B*, APS, v. 85, n. 4, p. 045129, 2012. Cited in page 46.

ASHCROFT, N.; MERMIN, N. *Solid State Physics*. Philadelphia: Saunders College, 1976. Cited 4 times in pages 20, 24, 26, and 98.

BAI, Z. et al. Giant kerr nonlinearity and low-power gigahertz solitons via plasmon-induced transparency. *Scientific reports*, Nature Publishing Group, v. 5, 2015. Cited 2 times in pages 22 and 23.

BOLTASSEVA, A.; ATWATER, H. A. Low-loss plasmonic metamaterials. *Science*, American Association for the Advancement of Science, v. 331, n. 6015, p. 290–291, 2011. Cited 3 times in pages 7, 29, and 30.

BORN, M.; WOLF, E. *Principles of optics: electromagnetic theory of propagation, interference and diffraction of light*. [S.l.]: Elsevier, 2013. Cited 2 times in pages 32 and 34.

BORODITSKY, M. et al. Light extraction from optically pumped light-emitting diode by thin-slab photonic crystals. *Applied Physics Letters*, AIP, v. 75, n. 8, p. 1036–1038, 1999. Cited in page 61.

BOYD, R. W. (Ed.). *Nonlinear Optics*. Third edition. Burlington: Academic Press, 2008. ISBN 978-0-12-369470-6. Disponível em: <http://www.sciencedirect.com/science/article/pii/B9780123694706000162>. Cited 4 times in pages 22, 23, 48, and 50.

BROENG, J. et al. Photonic crystal fibers: A new class of optical waveguides. *Optical fiber technology*, Elsevier, v. 5, n. 3, p. 305–330, 1999. Cited in page 61.

BROVENKO, A. et al. Resonant scattering of electromagnetic wave by stripe grating backed with a layer of metamaterial. *Progress In Electromagnetics Research B*, EMW Publishing, v. 15, p. 423–441, 2009. Cited in page 61.

BRUGGEMAN, D. Berechnung verschiedener physikalischer Konstanten von heterogenen Substanzen. I. Dielektrizitätskonstanten und Leitfähigkeiten der Mischkörper aus isotropen Substanzen. *Annalen der Physik*, v. 416, p. 636–664, 1935. Cited in page 20.

BUTCHER, J. C. *Numerical methods for ordinary differential equations*. [S.l.]: John Wiley & Sons, 2016. Cited in page 40.

CAI, W. et al. Optical cloaking with metamaterials. *Nature photonics*, Nature Publishing Group, v. 1, n. 4, p. 224–227, 2007. Cited in page 21.

CARVALHO, C. D. et al. Plasmon polariton and< n>= 0 non-bragg gaps in superlattices with metamaterials. *Physical Review B*, APS, v. 83, n. 8, p. 081408, 2011. Cited 3 times in pages 17, 45, and 76.

CAVALCANTI, S. et al. Bulk plasmon polariton-gap soliton-induced transparency in one-dimensional kerr-metamaterial superlattices. *Optics letters*, Optical Society of America, v. 39, n. 1, p. 178–181, 2014. Cited in page 55.

CAVALCANTI, S. et al. Band structure and band-gap control in photonic superlattices. *Physical Review B*, APS, v. 74, n. 15, p. 153102, 2006. Cited in page 99.

CAVALCANTI, S. et al. Photonic band structure and symmetry properties of electromagnetic modes in photonic crystals. *Physical Review E*, APS, v. 75, n. 2, p. 026607, 2007. Cited in page 99.

CHEN, W.; MILLS, D. Gap solitons and the nonlinear optical response of superlattices. *Physical review letters*, APS, v. 58, n. 2, p. 160, 1987. Cited 3 times in pages 52, 53, and 79.

CHEN, Y. Defect modes merging in one-dimensional photonic crystals with multiple single-negative material defects. *Applied Physics Letters*, AIP, v. 92, n. 1, p. 011925, 2008. Cited in page 61.

CHEN, Y. Tunable omnidirectional multichannel filters based on dual-defective photonic crystals containing negative-index materials. *Journal of Physics D: Applied Physics*, IOP Publishing, v. 42, n. 7, p. 075106, 2009. Cited in page 61.

CHENG, C.-C.; SCHERER, A. Fabrication of photonic band-gap crystals. *Journal of Vacuum Science & Technology B: Microelectronics and Nanometer Structures Processing, Measurement, and Phenomena*, AVS, v. 13, n. 6, p. 2696–2700, 1995. Cited in page 61.

CHRISTODOULIDES, D.; JOSEPH, R. Discrete self-focusing in nonlinear arrays of coupled waveguides. *Optics letters*, Optical Society of America, v. 13, n. 9, p. 794–796, 1988. Cited in page 54.

COJOCARU, E. Electromagnetic tunneling in lossless trilayer stacks containing single-negative metamaterials. *Progress In Electromagnetics Research*, EMW Publishing, v. 113, p. 227–249, 2011. Cited in page 61.

COSTA, A.; MEJÍA-SALAZAR, J.; CAVALCANTI, S. Defect modes in metamaterial photonic superlattices as tunneling resonances in trilayer structures. *JOSA B*, Optical Society of America, v. 33, n. 3, p. 468–473, 2016. Cited 2 times in pages 61 and 63.

DORMAND, J. R.; PRINCE, P. J. A family of embedded runge-kutta formulae. *Journal of computational and applied mathematics*, Elsevier, v. 6, n. 1, p. 19–26, 1980. Cited in page 40.

EGGLETON, B. J. et al. Bragg grating solitons. *Physical Review Letters*, APS, v. 76, n. 10, p. 1627, 1996. Cited in page 54.

FANG, A.; KOSCHNY, T.; SOUKOULIS, C. M. Lasing in metamaterial nanostructures. *Journal of Optics*, IOP Publishing, v. 12, n. 2, p. 024013, 2010. Cited in page 17.

GIBBS, H. *Optical bistability: controlling light with light.* [S.l.]: Elsevier, 2012. Cited 2 times in pages 49 and 52.

GIBBS, H.; MCCALL, S.; VENKATESAN, T. Differential gain and bistability using a sodium-filled fabry-perot interferometer. *Physical Review Letters*, APS, v. 36, n. 19, p. 1135, 1976. Cited in page 52.

GÓMEZ, F. R.; MEJÍA-SALAZAR, J. Bulk plasmon-polariton gap solitons in defective metamaterial photonic superlattices. *Optics letters*, Optical Society of America, v. 40, n. 21, p. 5034–5037, 2015. Cited in page 61.

HEGDE, R. S.; WINFUL, H. G. Optical bistability in periodic nonlinear structures containing left handed materials. *Microwave and Optical Technology Letters*, Wiley Online Library, v. 46, n. 6, p. 528–530, 2005. Cited in page 74.

HEGDE, R. S.; WINFUL, H. G. Zero-n gap soliton. *Optics letters*, Optical Society of America, v. 30, n. 14, p. 1852–1854, 2005. Cited 4 times in pages 9, 54, 55, and 56.

HESS, O. et al. Active nanoplasmonic metamaterials. *Nature materials*, Nature Publishing Group, v. 11, n. 7, p. 573, 2012. Cited in page 87.

HUNT, J. et al. Metamaterial apertures for computational imaging. *Science*, American Association for the Advancement of Science, v. 339, n. 6117, p. 310–313, 2013. Cited in page 22.

INOUE, K.; OHTAKA, K. *Photonic crystals: physics, fabrication and applications.* [S.l.]: Springer, 2013. v. 94. Cited in page 43.

JACKSON, J. D. *Classical electrodynamics.* 3rd ed.. ed. New York, NY: Wiley, 1999. ISBN 9780471309321. Disponível em: <http://cdsweb.cern.ch/record/490457>. Cited 3 times in pages 23, 33, and 41.

JIANG, H. et al. Omnidirectional gap and defect mode of one-dimensional photonic crystals containing negative-index materials. *Applied Physics Letters*, AIP, v. 83, n. 26, p. 5386–5388, 2003. Cited in page 17.

KAHN, L.; ALMEIDA, N.; MILLS, D. Nonlinear optical response of superlattices: multistability and soliton trains. *Physical Review B*, APS, v. 37, n. 14, p. 8072, 1988. Cited in page 53.

KAHN, L.; HUANG, K.; MILLS, D. Comparison of nonlinear optical responses of periodic and quasiperiodic superlattices. *Physical Review B*, APS, v. 39, n. 17, p. 12449, 1989. Cited in page 53.

KANG, Y. et al. Electromagnetic resonance tunneling in a single-negative sandwich structure. *Journal of Modern Optics*, Taylor & Francis, v. 60, n. 13, p. 1021–1026, 2013. Cited in page 61.

KATS, M. A. et al. Effect of radiation damping on the spectral response of plasmonic components. *Optics express*, Optical Society of America, v. 19, n. 22, p. 21748–21753, 2011. Cited in page 23.

KHURGIN, J. B.; SUN, G. In search of the elusive lossless metal. *Applied Physics Letters*, AIP, v. 96, n. 18, p. 181102, 2010. Cited in page 30.

KITTEL, C. *Introduction to solid state physics.* [S.l.]: Wiley, 2005. Cited in page 26.

LAL, S.; LINK, S.; HALAS, N. J. Nano-optics from sensing to waveguiding. *Nature photonics*, Nature Publishing Group, v. 1, n. 11, p. 641–648, 2007. Cited in page 30.

LANDAUER, R. The Electrical Resistance of Binary Metallic Mixtures. *Journal of Applied Physics*, v. 23, p. 779–784, jul. 1952. Cited in page 20.

LI, J. et al. Photonic band gap from a stack of positive and negative index materials. *Physical review letters*, APS, v. 90, n. 8, p. 083901, 2003. Cited 3 times in pages 17, 45, and 75.

LI, Q. et al. Wave propagation in nonlinear photonic band-gap materials. *Physical Review B*, APS, v. 53, n. 23, p. 15577, 1996. Cited in page 54.

LI, Y. et al. On-chip zero-index metamaterials. *Nature Photonics*, Nature Research, v. 9, n. 11, p. 738–742, 2015. Cited in page 31.

LIANG, W.; HE, S.; CHEN, L. On unusual narrow transmission bands for a multi-layered periodic structure containing left-handed materials. *Optics Express*, Optical Society of America, v. 11, n. 11, p. 1283–1290, 2003. Cited in page 43.

LIDORIKIS, E. et al. Optical nonlinear response of a single nonlinear dielectric layer sandwiched between two linear dielectric structures. *Physical Review B*, APS, v. 56, n. 23, p. 15090, 1997. Cited 2 times in pages 53 and 61.

LU, Z. Multiple narrow bandpass optical filters based on one-dimensional rugate photonic structures of two periodicities. *Optics letters*, Optical Society of America, v. 36, n. 4, p. 573–575, 2011. Cited in page 61.

LUGIATO, L. A. Ii theory of optical bistability. *Progress in optics*, Elsevier, v. 21, p. 69–216, 1984. Cited in page 49.

MARBURGER, J.; FELBER, F. Theory of a lossless nonlinear fabry-perot interferometer. *Physical Review A*, APS, v. 17, n. 1, p. 335, 1978. Cited in page 52.

MARCOS, J. S.; SILVEIRINHA, M. G.; ENGHETA, N. μ-near-zero supercoupling. *Physical Review B*, APS, v. 91, n. 19, p. 195112, 2015. Cited in page 30.

MATLAB. *version 9.2.0 (R2017a)*. Natick, Massachusetts: The MathWorks Inc., 2017. Cited in page 57.

MILLS, D.; TRULLINGER, S. Gap solitons in nonlinear periodic structures. *Physical Review B*, APS, v. 36, n. 2, p. 947, 1987. Cited in page 53.

MILLS, D. L. *Nonlinear Optics*. Berlin, Heidelberg: Springer Berlin Heidelberg, 1998. ISBN 978-3-540-64182-7. Disponível em: <http://link.springer.com/10.1007/978-3-642-58937-9>. Cited in page 33.

OUCHANI, N. et al. Defect modes in one-dimensional anisotropic photonic crystal. *Journal of Applied Physics*, AIP, v. 106, n. 11, p. 113107, 2009. Cited in page 61.

OWYOUNG, A. *The origins of the nonlinear refractive indices of liquids and glasses*. California Institute of Technology, 1972. (CIT theses). Disponível em: <https://books.google.com.br/books?id=deQaAQAAIAAJ>. Cited in page 46.

PARAZZOLI, C. et al. Performance of a negative index of refraction lens. *Applied physics letters*, AIP, v. 84, n. 17, p. 3232–3234, 2004. Cited in page 17.

PENDRY, J. B. et al. Low frequency plasmons in thin-wire structures. *Journal of Physics: Condensed Matter*, IOP Publishing, v. 10, n. 22, p. 4785, 1998. Cited in page 28.

PENDRY, J. B. et al. Extremely low frequency plasmons in metallic mesostructures. *Physical review letters*, APS, v. 76, n. 25, p. 4773, 1996. Cited in page 28.

PENDRY, J. B. et al. Magnetism from conductors and enhanced nonlinear phenomena. *IEEE transactions on microwave theory and techniques*, IEEE, v. 47, n. 11, p. 2075–2084, 1999. Cited in page 28.

PENDRY, J. B.; SMITH, D. R. Reversing light with negative refraction. *Physics Today*, v. 57, n. 6, p. 37, 2005. Cited in page 24.

PESCHEL, T. et al. Investigation of optical tunneling through nonlinear films. *JOSA B*, Optical Society of America, v. 5, n. 1, p. 29–36, 1988. Cited in page 41.

PIMENOV, A. et al. Negative refraction observed in a metallic ferromagnet in the gigahertz frequency range. *Physical review letters*, APS, v. 98, n. 19, p. 197401, 2007. Cited in page 74.

PIMENOV, A. et al. Negative refraction in ferromagnet-superconductor superlattices. *Physical review letters*, APS, v. 95, n. 24, p. 247009, 2005. Cited in page 25.

PUSCH, A. et al. Coherent amplification and noise in gain-enhanced nanoplasmonic metamaterials: A maxwell-bloch langevin approach. *ACS nano*, ACS Publications, v. 6, n. 3, p. 2420–2431, 2012. Cited in page 87.

RAMAKRISHNA, S. A. Physics of negative refractive index materials. *Reports on progress in physics*, IOP Publishing, v. 68, n. 2, p. 449, 2005. Cited in page 31.

RESHEF, O. et al. Direct observation of phase-free propagation in a silicon waveguide. *ACS Photonics*, ACS Publications, 2017. Cited in page 31.

REYES-GÓMEZ, E.; CAVALCANTI, S.; OLIVEIRA, L. Absorption effects on plasmon polariton-gap solitons in kerr/metamaterial superlattices. *EPL (Europhysics Letters)*, IOP Publishing, v. 106, n. 6, p. 64001, 2014. Cited 2 times in pages 17 and 18.

REYES-GÓMEZ, E.; CAVALCANTI, S.; OLIVEIRA, L. Non-bragg-gap solitons in one-dimensional kerr-metamaterial fibonacci heterostructures. *Physical Review E*, APS, v. 91, n. 6, p. 063205, 2015. Cited in page 17.

REYES-GÓMEZ, E.; CAVALCANTI, S.; OLIVEIRA, L. Soliton-induced transparency in disordered kerr-metamaterial heterostructures. *JOSA B*, Optical Society of America, v. 33, n. 3, p. 320–327, 2016. Cited in page 17.

REYES-GÓMEZ, E. et al. Plasmon polaritons in photonic superlattices containing a left-handed material. *EPL (Europhysics Letters)*, IOP Publishing, v. 88, n. 2, p. 24002, 2009. Cited 4 times in pages 17, 31, 45, and 76.

RUSSELL, J. S. Report on waves. In: *14th meeting of the British Association for the Advancement of Science.* [S.l.: s.n.], 1844. v. 311, n. 390, p. 1844. Cited in page 50.

SCHURIG, D. et al. Metamaterial electromagnetic cloak at microwave frequencies. *Science*, American Association for the Advancement of Science, v. 314, n. 5801, p. 977–980, 2006. Cited in page 22.

SHELBY, R. et al. Microwave transmission through a two-dimensional, isotropic, left-handed metamaterial. *Applied Physics Letters*, AIP, v. 78, n. 4, p. 489–491, 2001. Cited in page 28.

SHELBY, R. A.; SMITH, D. R.; SCHULTZ, S. Experimental verification of a negative index of refraction. *science*, American Association for the Advancement of Science, v. 292, n. 5514, p. 77–79, 2001. Cited 2 times in pages 17 and 28.

SHIH, R. et al. Microwave phase conjugation in a liquid suspension of elongated microparticles. *Physical review letters*, APS, v. 65, n. 5, p. 579, 1990. Cited in page 74.

SIHVOLA, A. Metamaterials in electromagnetics. *Metamaterials*, Elsevier, v. 1, n. 1, p. 2–11, 2007. Cited in page 21.

SILVEIRINHA, M.; ENGHETA, N. Tunneling of electromagnetic energy through subwavelength channels and bends using ε-near-zero materials. *Physical review letters*, APS, v. 97, n. 15, p. 157403, 2006. Cited in page 30.

SMITH, D. R. et al. Composite medium with simultaneously negative permeability and permittivity. *Physical review letters*, APS, v. 84, n. 18, p. 4184, 2000. Cited 2 times in pages 22 and 28.

SOLYMAR, L.; SHAMONINA, E. *Waves in metamaterials.* [S.l.]: Oxford University Press, 2009. Cited 2 times in pages 21 and 32.

SUKHORUKOV, A. A.; KIVSHAR, Y. S. Discrete gap solitons in modulated waveguide arrays. *Optics letters*, Optical Society of America, v. 27, n. 23, p. 2112–2114, 2002. Cited in page 54.

TRUTSCHEL, U.; LEDERER, F. Optical response of nonlinear absorbing and saturable superlattices. *JOSA B*, Optical Society of America, v. 5, n. 12, p. 2530–2536, 1988. Cited 2 times in pages 41 and 53.

VALENTINE, J. et al. An optical cloak made of dielectrics. *nature materials*, Nature Publishing Group, v. 8, p. 568–571, 2009. Cited in page 17.

VALENTINE, J. et al. Three-dimensional optical metamaterial with a negative refractive index. *nature*, Nature Publishing Group, v. 455, n. 7211, p. 376, 2008. Cited in page 17.

VESELAGO, V. Electrodynamics of media with simultaneously negative magnetic and electric permeabilities. *Sov. Phys.—Usp.*, v. 10, p. R04, 1968. Cited 2 times in pages 17 and 21.

VIGNERON, J. P.; SIMONIS, P. Natural photonic crystals. *Physica B: Condensed Matter*, Elsevier, v. 407, n. 20, p. 4032–4036, 2012. Cited in page 42.

WEST, P. R. et al. Searching for better plasmonic materials. *Laser & Photonics Reviews*, Wiley Online Library, v. 4, n. 6, p. 795–808, 2010. Cited 2 times in pages 30 and 31.

WILTSHIRE, M. et al. Microstructured magnetic materials for rf flux guides in magnetic resonance imaging. *Science*, American Association for the Advancement of Science, v. 291, n. 5505, p. 849–851, 2001. Cited in page 17.

WINFUL, H. G.; MARBURGER, J.; GARMIRE, E. Theory of bistability in nonlinear distributed feedback structures. *Applied Physics Letters*, AIP, v. 35, n. 5, p. 379–381, 1979. Cited in page 52.

XIAO, S. et al. Loss-free and active optical negative-index metamaterials. *Nature*, Nature Publishing Group, v. 466, n. 7307, p. 735, 2010. Cited in page 17.

XIAO, S. et al. Loss-free and active optical negative-index metamaterials. *Nature*, Nature Research, v. 466, n. 7307, p. 735–738, 2010. Cited in page 30.

YABLONOVITCH, E. Photonic band-gap crystals. *Journal of Physics: Condensed Matter*, IOP Publishing, v. 5, n. 16, p. 2443, 1993. Cited in page 43.

YEH, P. *Optical waves in layered media.* [S.l.]: Wiley-Interscience, 2005. v. 61. Cited 2 times in pages 32 and 38.

Appendix

APPENDIX A – Dispersion relation

A.1 Dispersion relation

This appendix is devoted to show the derivation of the dispersion relation for an infinite lattice composed of two materials, A and B, with widths a and b respectively, as the figure A.1 shows.
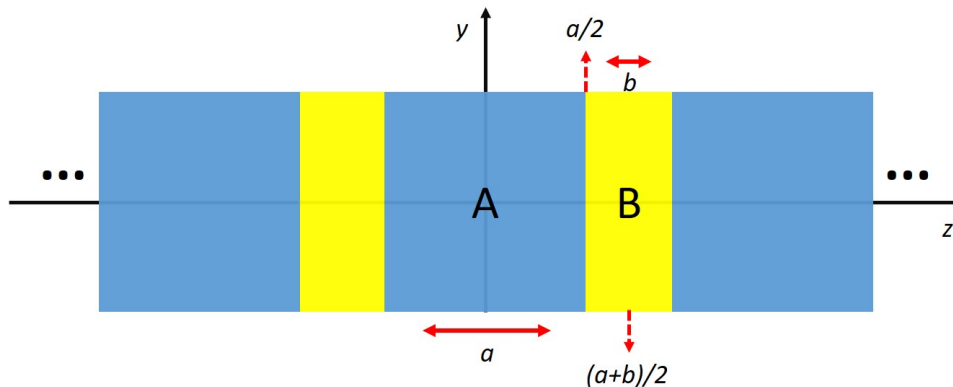
Figure 45 – Infinite periodic lattice composed of two materials A and B.

Assume, in this chapter, that:

$$\mathbf{\Phi}(z) = \left(\begin{array}{c} E_x(z) \\ c\mu_0 H_y(z) \end{array} \right)$$

.

If we want to know the fields on the point $z = a/2$ we have:

$$\mathbf{\Phi}\left(\frac{a}{2}\right) = \mathbf{M}_A\left(\frac{a}{2}\right)\mathbf{\Phi}(0) \tag{A.1}$$

where:

$$\mathbf{M}_A(z) = \left(\begin{array}{cc} \cos q_A z & \frac{i}{p_A}\sin q_A z \\ ip_A\sin q_A z & \cos q_A z \end{array} \right)$$

with $q_A = \frac{\omega}{c}\sqrt{\epsilon_A\mu_A - \beta^2}$, $p_A = \frac{q_A c\mu_0}{\omega\mu_A}$.

Doint the same procedure for $z = (a + b)/2$, one can find:

$$\mathbf{\Phi}\left(\frac{a + b}{2}\right) = \mathbf{M}_B\left(\frac{b}{2}\right)\mathbf{\Phi}\left(\frac{a}{2}\right) \tag{A.2}$$

which, by replacing eq. A.1, gives:

$$\mathbf{\Phi}\left(\frac{a + b}{2}\right) = \mathbf{M}_B\left(\frac{b}{2}\right)\mathbf{M}_A\left(\frac{a}{2}\right)\mathbf{\Phi}(0) \tag{A.3}$$

where:

$$\mathbf{M}_B(\frac{b}{2}) = \begin{pmatrix} \cos\frac{q_B b}{2} & \frac{i}{p_B}\sin\frac{q_B b}{2} \\ ip_B\sin\frac{q_B b}{2} & \cos\frac{q_B b}{2} \end{pmatrix}$$

with $q_B = \frac{\omega}{c}\sqrt{\epsilon_B\mu_B - \beta^2}$ and $p_B = \frac{q_B c\mu_0}{\omega\mu_B}$. Making:

$$\mathbf{T}(a,b) = \mathbf{M}_B\left(\frac{b}{2}\right)\mathbf{M}_A\left(\frac{a}{2}\right) = \begin{pmatrix} p & q \\ r & s \end{pmatrix} \tag{A.4}$$

in which:

$$p = \cos\left(\frac{q_A a}{2}\right)\cos\left(\frac{q_B b}{2}\right) - \frac{p_A}{p_B}\sin\left(\frac{q_B b}{2}\right)\sin\left(\frac{q_A a}{2}\right) \tag{A.5}$$

$$q = \frac{i}{p_A}\sin\left(\frac{q_A a}{2}\right)\cos\left(\frac{q_B b}{2}\right) + \frac{i}{p_B}\sin\left(\frac{q_B b}{2}\right)\cos\left(\frac{q_A a}{2}\right) \tag{A.6}$$

$$r = ip_B\sin\left(\frac{q_B b}{2}\right)\cos\left(\frac{q_A a}{2}\right) + ip_A\sin\left(\frac{q_A a}{2}\right)\cos\left(\frac{q_B b}{2}\right) \tag{A.7}$$

$$s = -\frac{p_B}{p_A}\sin\left(\frac{q_B b}{2}\right)\sin\left(\frac{q_A a}{2}\right) + \cos\left(\frac{q_B b}{2}\right)\cos\left(\frac{q_A a}{2}\right). \tag{A.8}$$

Using the same formalism, one can obtain for the oposite direction ($z = -(a+b)/2$):

$$\mathbf{\Phi}\left(-\frac{a+b}{2}\right) = \mathbf{M}_B\left(-\frac{b}{2}\right)\mathbf{M}_A\left(-\frac{a}{2}\right)\mathbf{\Phi}(0); \tag{A.9}$$

thus:

$$\mathbf{\Phi}\left(-\frac{a+b}{2}\right) = \mathbf{T}(-a,-b)\mathbf{\Phi}(0). \tag{A.10}$$

From eq. A.3, one can find:

$$\mathbf{T}(-a,-b) = \mathbf{M}_B\left(-\frac{b}{2}\right)\mathbf{M}_A\left(-\frac{a}{2}\right) = \begin{pmatrix} p & -q \\ -r & s \end{pmatrix} \tag{A.11}$$

To proceed with this demonstration the use of Bloch's theorem will be needed (ASHCROFT; MERMIN, 1976). Bloch's theorem is very important in periodic media because it permitts one to write the fields of interest to be written as a plane wave modulated by a periodic function (with the periodicity of the lattice). For our case, one could write the Bloch's theorem as:

$$\mathbf{\Phi}\left(\frac{a+b}{2}\right) = e^{iSd}\mathbf{\Phi}\left(-\frac{a+b}{2}\right) \tag{A.12}$$

where S is the bloch wave vector along the z direction. By replacing equations A.3 and A.10 into eq. A.12 (and by making use of the $\mathbf{T}$ matrix), one can obtain:

$$\begin{pmatrix} p & q \\ r & s \end{pmatrix}\mathbf{\Phi}(0) = e^{iSd}\begin{pmatrix} p & -q \\ -r & s \end{pmatrix}\mathbf{\Phi}(0)$$

. Some trivial algebra leads to:

$$\begin{pmatrix} p(1 - e^{iSd}) & q(1 + e^{iSd}) \\ r(1 + e^{iSd}) & s(1 - e^{iSd}) \end{pmatrix} \mathbf{\Phi}(0) = 0$$

. Equation A.1 has a nontrivial solution if and only if:

$$\begin{vmatrix} p(1 - e^{iSd}) & q(1 + e^{iSd}) \\ r(1 + e^{iSd}) & s(1 - e^{iSd}) \end{vmatrix} = 0$$

thus:

$$ps(1 - e^{iSd})^2 - qr(1 + e^{iSd})^2 = 0. \tag{A.13}$$

One can show that $ps - qr = 1$ just by using eqs. A.5 to A.8 and some trigonometric relations. Some algebra now is necessary to find the dispersion relation, it follows from A.13:

$$\cos(Sd) = ps + qr; \tag{A.14}$$

Using eqs. A.5 to A.8 one can obtain:

$$\cos(Sd) = \cos(q_A a)\cos(q_B b) - \frac{1}{2}\left(\frac{p_B}{p_A} + \frac{p_A}{p_B}\right)\sin(q_A a)\sin(q_B b) \tag{A.15}$$

This equation allows us to obtain the dispersion relations $\omega = \omega(K)$ commonly used in optical lattices and solid state physics. A more detailed explanation about this derivation and some insightfull applications can be found in (CAVALCANTI et al., 2006) and (CAVALCANTI et al., 2007), for example.

Annex

Gap soliton transparency switch in one-dimensional Kerr-metamaterial superlattices

T. P. Lobo

Laboratório de Computação Científica e Visualização (LCCV), Universidade Federal de Alagoas, Maceió-AL, 57072-970, Brazil

L. E. Oliveira

Instituto de Física, Universidade Estadual de Campinas-Unicamp, Campinas-São Paulo, 13083-859, Brazil

S. B. Cavalcanti

Instituto de Física, Universidade Federal de Alagoas, Maceió-AL, 57072-970, Brazil

Abstract

Plasmon-polariton gap soliton formation and transparency switching in one-dimensional nonlinear layered systems composed of alternate layers of a Kerr material and a dispersive linear metamaterial are theoretically studied. The behavior of the electric field profile inside the layered system is shown for different values of nonlinear power, linking the localized modes of the electric field with complete transparency states of the system. A detailed investigation on the influence of a defocusing nonlinearity on the transmission switching phenomenon, in the frequency range where the linear dispersion predicts the photon-plasmon coupling, is made, revealing different effects in the top and bottom edges of the plasmon-polariton gap. Specifically, we found a broadening of the plasmon-polariton gap when increasing the nonlinear power. In addition, a switching from very low to high transmission states is obtained and localized plasmon-polariton gap solitons of various orders are found for various values of frequencies and nonlinear strength.

Keywords: Science, Publication, Complicated

1. Introduction

In the last few decades, researchers all over the world have managed to produce artificial complex materials widely used to shape and manipulate light [1, 2]. The remarkable flexibility of high-quality optical materials has allowed the fabrication of nanostructures [3, 4], where one may tailor the electromagnetic dispersion and mode structures at one's choice, providing new phenomena for further investigations and new device applications. In addition, such new materials have given a refreshing flavor to old subjects as nonlinear wave propagation through one-dimensional (1D) layered systems [5]. In particular, systems containing metamaterials, which exhibit electric and magnetic negative responses to an optical field within the same frequency range, provide excellent man-made materials for a number of areas of intense interest [6, 7]. Recently, the merging of plasmonic and metamaterial areas has opened up a new perspective toward achieving the ultimate control of light in the nanoscale dimension [8, 9].

Plasmon-polaritons (PPs) are elementary excitations due to the resonant coupling of plasmons with light. Recent work on the dispersion relation of a layered system composed by bilayers AB of a dispersive metamaterial (A) and air (B) has demonstrated that, under oblique incidence of light, a resonant coupling between a plasmon and a photon gives rise to a non-Bragg bulk-like PP gap at the plasmonic frequency [10]. As photons and plasmons have different dispersion relations, there is an anticrossing region evidencing the photon-plasmon coupling. Outside this region there is no coupling and therefore, plasmons and photons retrieve their individual character. By substituting the air layers by a nonlinear Kerr material, and choosing a particular frequency within the anticrossing region, multistability, transmission switch and resonant formation of soliton waves seem to occur at particular values of nonlin-

earity intensities for which total transmission ($T = 1$) is possible. Various layer arrangements were studied such as periodic, quasi-periodic and disordered arrangements, with absorption included, indicating that nonlinear switching with soliton formation is a robust phenomenon [11, 12, 13].

In this work we extend these previous findings on layered systems, to understand the role of nonlinearity on the dispersion relation around the anticrossing region. To this end, we investigate the transmission properties of incident light, under oblique incidence, upon a layered system composed of bilayers nonlinear/metamaterial in a periodic arrangement. A thorough investigation on the influence of nonlinearity on the transparency-switching phenomenon is made, by sweeping the frequency region where the photon-plasmon coupling occurs in the case of a self-defocusing Kerr nonlinearity. It should be noted here that we have previously shown [11] that the transparency switching phenomenon is robust with respect to absorption and could be observed even in the case of a single bilayer and relatively high levels of absorption. As expected, there are no total transmission states as those now have lower intensity, however the overall behavior is the same with or without absorption. For this reason here, we neglect absorption and focus on the influence of the nonlinearity on the transparency switching phenomenon by sweeping the frequency region where the photon-plasmon coupling occurs in the case of a self-defocusing nonlinearity. We find that the detuning, that is, the depart of the frequency investigated from the resonant frequency, does not hinder soliton formation. Actually, we find that within the whole range of frequencies between the resonant points of total transmission ($T = 1$), lower intensity solitons of all orders are still formed. Furthermore, we show that in the self-defocusing case, the top edge of the PP gap is shifted to higher frequencies proportionally to the nonlinearity intensity while the lower PP gap edge essentially does not change in frequency. Thus, the "nonlinear PP gap" becomes larger than the linear one. We present our investigations on the role of the nonlinearity in the transparency switching phenomenon as follows: Section 2 consists of the theoretical development and basic definitions. Section 3 deals with the transmission switching due to gap soliton formation in the neighborhood of the non-Bragg PP gap. Finally, in Section 4 we present our conclusions.

2. Theoretical framework

The geometry of the problem discussed in this paper is shown in fig 1(a), where the z-direction is chosen as the stacking direction of the lattice. The heterostructure, with length L, is sandwiched between vacuum on the left and right side, and is composed of $N = 32$ unit cells AB formed by a Kerr medium (layers A) and a metamaterial (layers B) whose widths are $d_A = 10$ mm and $d_B = 10$ mm, respectively. To accommodate a more general class of problems, we assume throughout this section that the superlattice is sandwiched by media with magnetic permeability μ_1, μ_2 and electric permittivity ϵ_1, ϵ_2 in the left and right sides, respectively [cf. Fig. 1(a)]. In this study, layers A are characterized by a magnetic permeability μ_A and an electric permittivity $\epsilon_A = \epsilon_A^0 + a|E|^2$, where $E = E(z)$ is the electric-field amplitude of the electromagnetic field inside the superlattice. The slabs B are characterized by a metamaterial with magnetic permeability and electric permittivity defined as [14]

$$\epsilon_B = 1.6 + \frac{40}{0.81 - v^2 - iv\gamma} \qquad (1)$$

$$\mu_B = 1.0 + \frac{25}{0.814 - v^2 - iv\gamma} \qquad (2)$$

where v is the frequency in GHz and γ accounts for absorption. Throughout this paper only cases where there is no absorption ($\gamma = 0$) are studied. Considering the oblique incidence of TE waves polarized along the x-axis direction, the electric-field amplitude, inside the superlattice, satisfies the differential equation

$$-\frac{d}{dz}\frac{1}{\mu(z)}\frac{d}{dz}E(z) = \left[\frac{\omega^2}{c^2}\epsilon(z) - \frac{\omega^2\beta}{c^2\mu(z)}\right]E(z) \qquad (3)$$

where $\omega = 2\pi v$, $\beta = n \sin\theta$ with n being the refractive index, θ is the incidence angle, and $\epsilon(z)$ and $\mu(z)$ are the electric permittivity and magnetic permeability of the heterostructure which are given by $\epsilon_A(\epsilon_B)$ and $\mu_A(\mu_B)$, respectively, in layer A(B). As dictated by Snell's law, β is constant throughout the heterostructure. By introducing a dimensionless position ($\zeta = k_0 z$), with $k_0 = \omega/c$, the equation for the amplitude of the electric field within the slab i may be rewritten as

$$\frac{d^2}{d\zeta^2}E + (\epsilon_i\mu_i - \beta^2)E = 0 \qquad (4)$$

where $i = A, B$.

The procedure outlined here for the numerical integration of Eq. 4 is an extension of the work of Trutschel and Lederer [15] and Peschel *et al.* [16]. While they numerically solve Eq. 4 for nonmagnetic media, we proceed by showing the calculations for materials where $\mu \neq 1$. Let us then begin by choosing $E(k_0 L_i)$ and its derivative $\frac{d}{d\zeta}E(k_0 L_i)$, and integrating Eq. 4 using an
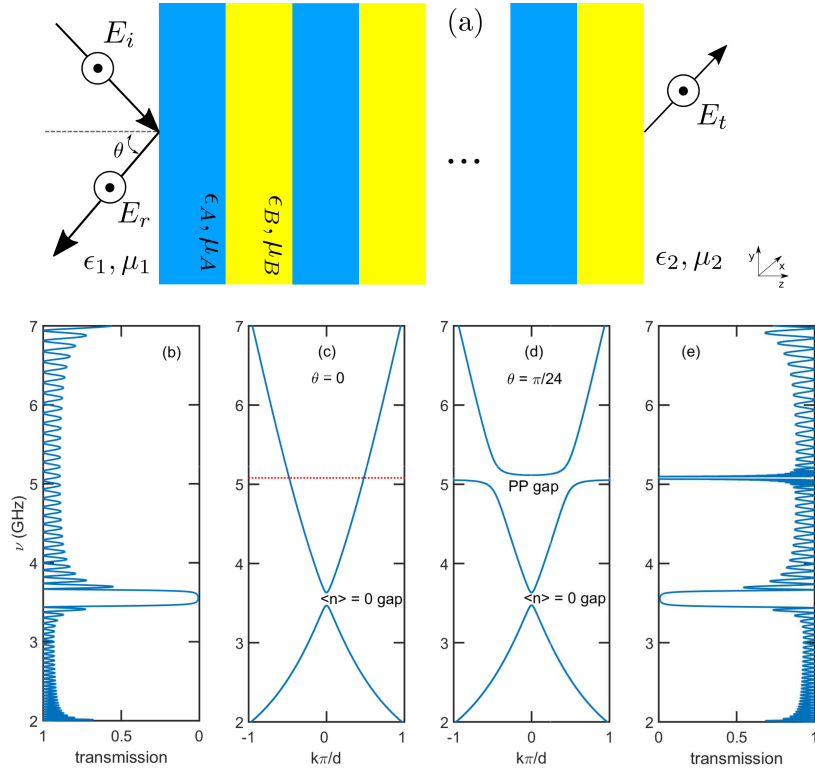
Figure 1: (a)(Color online) Pictorial view of the *z*-growth photonic superlattice with A and B alternated layers in a periodic arrangement, for TE-like incident electromagnetic waves; transmission coefficient as a function of the wave frequency in a heterostructure composed of 32 AB layers, with $a = b = 10$ mm, in the absence of absorption and nonlinearity ($\gamma = 0$ and $a = 0$ respectively), for (b) normal, $\theta = 0$, and (e) TE oblique incidence, $\theta = \pi/24$. Panels (c) and (d) depict the dispersion relation corresponding to the infinite heterostructure for normal ($\theta = 0$) and oblique ($\theta = \pi/24$) incidence, respectively. The following parameters were chosen: for the linear RHM layer $\epsilon_A^0 = \epsilon_A = 2, \mu_A = 1$, and, for the linear LHM, the parameters are the same given by Eqs. (1) and (2). In panel (c) we also indicate by a dotted line the $\nu_m^p = 5.08$ GHz bulk-like longitudinal magnetic plasmon frequency.

3

adapted fourth-order Runge-Kutta method from $\zeta = kL_i$ to $\zeta = k(L_i - d_i)$, where L_i is the position of the outer surface of the i-th layer. The field in the remaining layers are integrated in a similar fashion, but the initial values E and $\frac{d}{d\zeta}E$, for each new integration, are now obtained by ensuring the continuity of both E and $\frac{1}{\mu}\frac{d}{d\zeta}E$ through each interface. To obtain reflection and transmission coefficients, one needs to calculate the incident E_i, reflected E_r and transmitted E_t electric fields, which are obtained by the imposition of boundary conditions at the vacuum regions. The electric field for $\zeta < 0$ is formed by a superposition of the incident and the reflected field whereas the electric field for $\zeta > k_0L$ is given by the transmitted field

$$E(\zeta) = \begin{cases} E_i e^{iQ_1\zeta} + E_r e^{-iQ_1\zeta} & \text{if } \zeta < 0 \\ E_t e^{iQ_2(\zeta - k_0L)} & \text{if } \zeta > k_0L \end{cases} \quad (5)$$

where $Q_i = \sqrt{\epsilon_j\mu_j - \beta^2}$, with $j = 1, 2$ if $\zeta < 0$ or $\zeta > k_0L$ respectively. By assuring the continuity of both E and $\frac{1}{\mu}\frac{dE}{d\zeta}$ at $\zeta = k_0L$, one may assign a value for the electric-field amplitude E_t in the outer interface and obtain the values of both $E(k_0L) = E_t$ and $\frac{d}{d\zeta}E(k_0L) = iQ\mu_B E_t/\mu_2$. Then, by integrating equation 4 for each internal layer, as described before, one may find $E(0)$ and $\frac{d}{d\zeta}E(0)$. By imposing the continuity of both E and $\frac{1}{\mu}\frac{dE}{d\zeta}$ in $\zeta = 0$ one may find the incident and reflected fields as a function of $E(0)$ and $\frac{dE(0)}{d\zeta}$,

$$E_i = \frac{1}{2}\left[E(0) - \frac{i\mu_1}{Q\mu_A}\frac{dE(0)}{d\zeta}\right] \quad (6)$$

$$E_r = \frac{1}{2}\left[E(0) + \frac{i\mu_1}{Q\mu_A}\frac{dE(0)}{d\zeta}\right] \quad (7)$$

Moreover, the transmittance T and reflectivity R are given by

$$T = \frac{\sqrt{\epsilon_2}\sqrt{\mu_1}n_{z,2}}{\sqrt{\epsilon_1}\sqrt{\mu_2}n_{z,1}}\left|\frac{E_t}{E_i}\right|^2 \quad (8)$$

$$R = \left|\frac{E_r}{E_i}\right|^2 \quad (9)$$

where $n_{z,1}$ and $n_{z,2}$ are the z components of the normalized wave vector $\mathbf{k}$ in the vacuum regions.

3. Results and Discussion

We begin by discussing the transmission of the heterostructure in the absence of absorption ($\gamma = 0$) and nonlinearity ($a = 0$). In Figs. 1(b) and (e) we show the
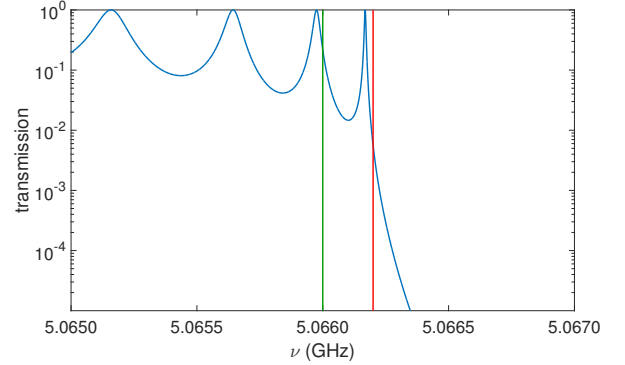

Figure 2: (Color online) Transmission through the same structure and linear parameter as in Fig 1, for $\theta = \pi/24$, and TE incidence in the vicinity of the lower edge of the PP gap. The red vertical line is at $\nu = 5.0662$ GHz, for which $T \approx 0.0056$, and the green vertical line is at at $\nu = 5.0660$ GHz, for which $T \approx 0.2174$.

transmission as a function of the incoming wave frequency for normal incidence ($\theta = 0$) and oblique incidence ($\theta = \pi/24$), respectively, showing that when the frequency is near ν_m^p, the bulk-like longitudinal plasmon frequency ($\mu_B = 0$ at $\nu = \nu_m^p = 5.0807$ GHz), there is a region of zero-transmittance when treating the case of oblique incidence. In a TE configuration, and for oblique incidence, there is a component of the magnetic field in the direction of the stratification, which couples to the bulk-like longitudinal magnetic plasmon mode, giving origin to the PP gap [10], the zero-transmittance region around ν_m^p. It is also plotted the dispersion relation for an infinite-layered system (Figs. 1(c) and (d)), and one may observe that the PP gap opens up around the magnetic plasmon frequency ν_m^p for the case of oblique incidence, predicting the behavior of the finite superlattice used in Fig. 1(e). It should be noted that the system studied in this work ($N = 32$) also shows good agreement with the infinite-layered superlattice (Figs. 1(c) and (d)) with respect to the zero-n gap.

Here we focus our attention within the frequency regions around the edges of the longitudinal bulk-like PP gap for the finite heterostructure described in Fig. 1, and investigate the behavior of the transmission and the electromagnetic field profile by increasing the nonlinear power $a|E_i|^2$. In Fig. 2 we plot the transmission of the structure for $\theta = \pi/24$ at the lower edge of the PP gap and absence of nonlinearity ($a = 0$). As a starting point we choose two frequencies ($\nu = 5.0660$ GHz, 5.0662 GHz) and study the influence of a defocusing nonlinearity ($a < 0$) on the electric field profile inside the structure and in its transmission proper-
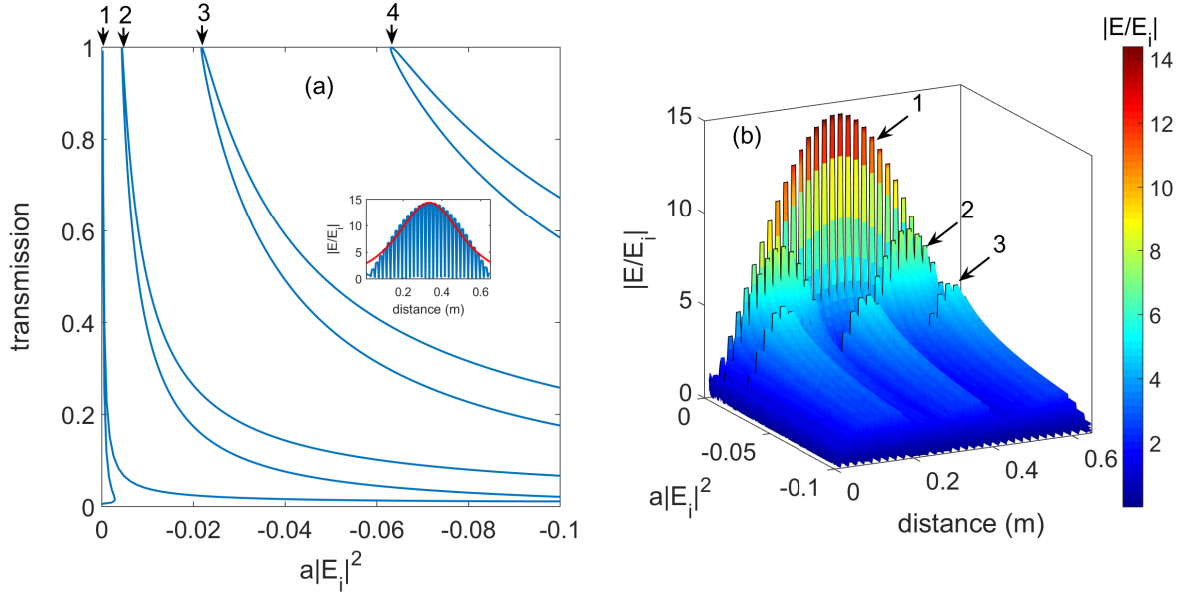
4

Figure 3: (Color online) Calculated results for the same structure and linear parameters as in Fig 1: (a) Transmission as a function of increasing power of a defocusing nonlinearity for $\theta = \pi/24$ in the case of TE incidence. We show several transparency (transmission $T = 1$) points for $\nu = 5.0662$ GHz, occurring at values (see arrows) of $a|E_i|^2$ equal to $-0.0002, -0.0044, -0.022$ and -0.063; the inset illustrates the fitting of a one-soliton mode envelope to a $\text{sech}(\alpha z)$ function (α as the fitting parameter) indicating that we do have essentially a soliton-like solution. (b) Spatial profile for the electric field versus the nonlinear power, with $\nu = 5.0662$ GHz. Outlined in black and highlighted by the arrows are the places where full transparency is found (transmission T=1), for values of $a|E_i|^2$ equal to $-0.0002, -0.0044, -0.022$. There are (see arrows) one-soliton, two-soliton and three-soliton modes in the nonlinear power range shown.
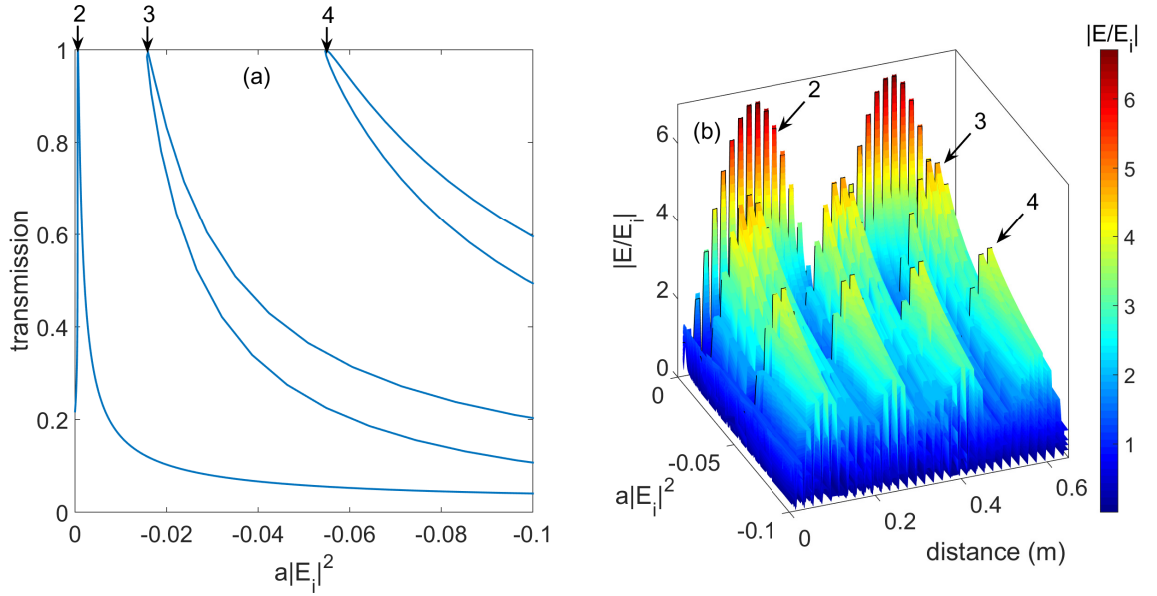

Figure 4: (Color online) Calculated results for the same structure and linear parameters as in Fig 1: (a) Transmission as a function of increasing power of a defocusing nonlinearity for $\theta = \pi/24$ in the case of TE incidence. We show several transparency (transmission $T = 1$) points for $\nu = 5.0660$ GHz, for values (see arrows) of $a|E_i|^2$ equal to $-0.00062, -0.016$ and -0.055; (b) Corresponding spatial profile for the electric field versus the nonlinear power, with $\nu = 5.0660$ GHz. Outlined in black and highlighted by the arrows are the places where full transparency is found (T=1). There are (see arrows) two-soliton, three-soliton and four-soliton modes in the nonlinear power range shown.
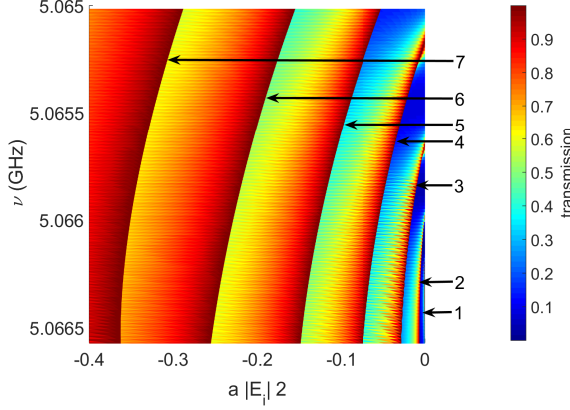
5

Figure 5: (Color online) Color plot of the transmission coefficient for different values of the nonlinear power and frequencies in the vicinity of the lower edge of the PP gap, for the system considered in Fig. 1, and $\theta = \pi/24$ in the TE configuration. In red are the regions where we find transparency and soliton modes (see arrows). The n = 1,2,...,7 arrow numbers indicate the n-soliton modes in the nonlinear power range shown.

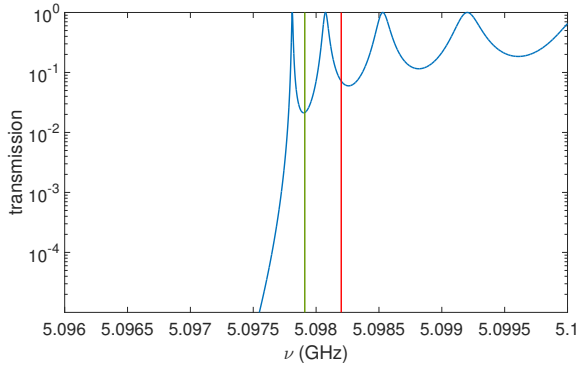

Figure 6: (Color online) TE Transmission through the same structure and linear parameter as in Fig 1, for $\theta = \pi/24$, and for frequencies in the vicinity of the top edge of the PP gap. The green vertical line is at $\nu = 5.09820$ GHz, for which $T \approx 0.07$, and the red vertical line is at $\nu = 5.09791$ GHz, for which $T \approx 0.02$.

ties. For $\nu = 5.0662$ GHz one finds $T \approx 0.0056$ when $a = 0$. A defocusing nonlinearity gives rise to a multistable behavior of the transmission (Fig. 3(a)), and there are four transparency ($T = 1$) points in the nonlinear power range shown. Specifically one obtains $T = 1$ when $a|E_i|^2 = -0.0002, -0.0044, -0.022, -0.063$. In Fig. 3(b) we plot the spatial profile for the electric field versus the nonlinear power, revealing that each transparency point is connected to a stable branch of the electric field, as shown by the arrows. In addition, the envelope function of the one mode branch is fitted accurately by the function $f(x) = E^M (\text{sech } \alpha x)$, where E^M is the maximum value of E, and α is a fitting parameter, which suggests that these modes mimic the behavior of true solitons, as commented by Chen [17]. For $\nu = 5.0660$ GHz we have $T \approx 0.2174$ when $a = 0$ and Fig. 4 shows that the nonlinearity creates three transparency points in the nonlinear power range shown ($a|E_i|^2 = -0.00062, -0.016, -0.055$). The electric field versus the nonlinear power plot [cf. Fig. 4(b)] shows that each transparency point is connected to a stable branch of the electric field, as shown by the arrows, the same behavior encountered for $\nu = 5.06624$ GHz. However, there is no one-mode soliton branch for this frequency, i.e, no value of the nonlinear power, for a defocusing nonlinearity, is associated with a one-soliton like profile of the electric field. This stems from the fact that as we consider smaller frequencies, driving away from the PP gap edge, in the nonlinear regime, the otherwise stable soliton-like modes disappear. There is a cut-off frequency value ν_1 below which there is no fundamental soliton mode, and the same occurs for each of the n-soliton modes observed, as they disappear for frequencies smaller than ν_n. In Fig. 5 we plot the transmission as a function of the nonlinear power and frequency, to illustrate this fact. Each $T = 1$ curve is associated with a n-soliton like mode, where n is outlined by numbers and arrows. Note that these curves appear around the edge of the PP gap and vanish for specific values ν_n of the frequency.

We proceed by extending the study to the top edge of the TE PP gap, turning to Fig. 6 which shows the transmission as a function of the incident frequency when there is no nonlinearity ($a = 0$), with $\theta = \pi/24$. We choose two frequency points ($\nu = 5.0982$ GHz, 5.09791 GHz) to observe the effects of an increasing defocusing nonlinearity in the transmission properties and electric field profiles inside the structure. The inclusion of nonlinearity is depicted in Figs. 7(a) and 8(a), for $\nu = 5.09791$ GHz and $\nu = 5.0982$ GHz, respectively. Transparency switching is observed for both frequencies but while for $\nu = 5.09791$ GHz the first trans-
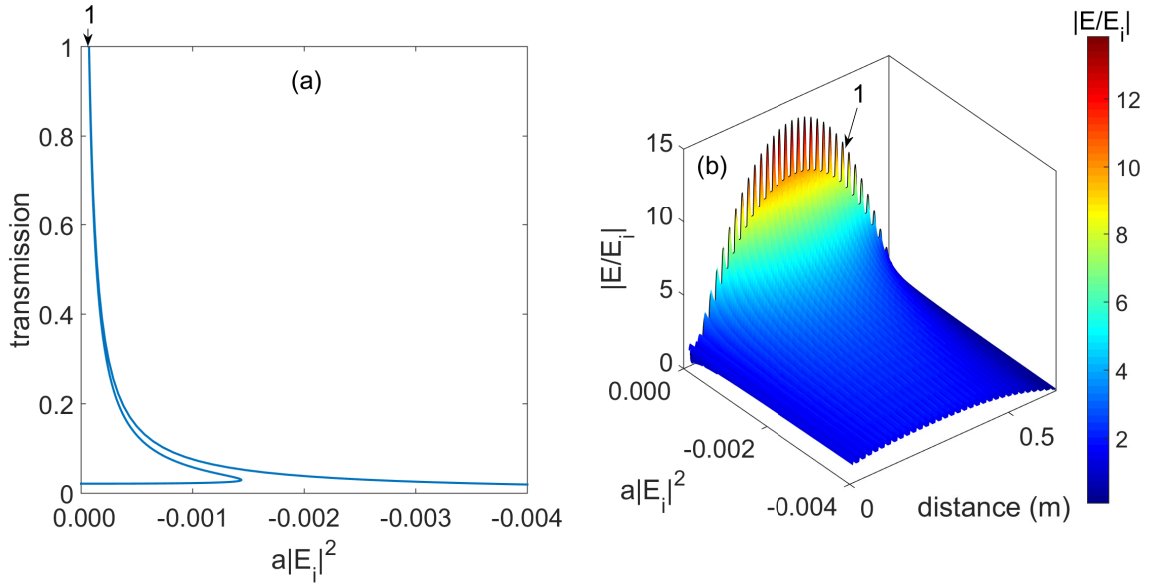
6

Figure 7: (Color online) Calculated results for the same structure and linear parameters as in Fig 1: (a) Transmission as a function of increasing power of a defocusing nonlinearity for $\theta = \pi/24$ in the case of TE incidence. Only one transparency ($T = 1$) point is found for $\nu = 5.09791$ GHz, at a value of $a|E_i|^2$ (see arrow) equal to -0.00007; (b) Corresponding spatial profile for the electric field versus the nonlinear power. Outlined in black and highlighted by the arrow is the place where full transparency is found ($T = 1$), at a value of $a|E_i|^2$ equal to -0.00007. There are (see arrow) only one-soliton like modes in the nonlinear power range shown.
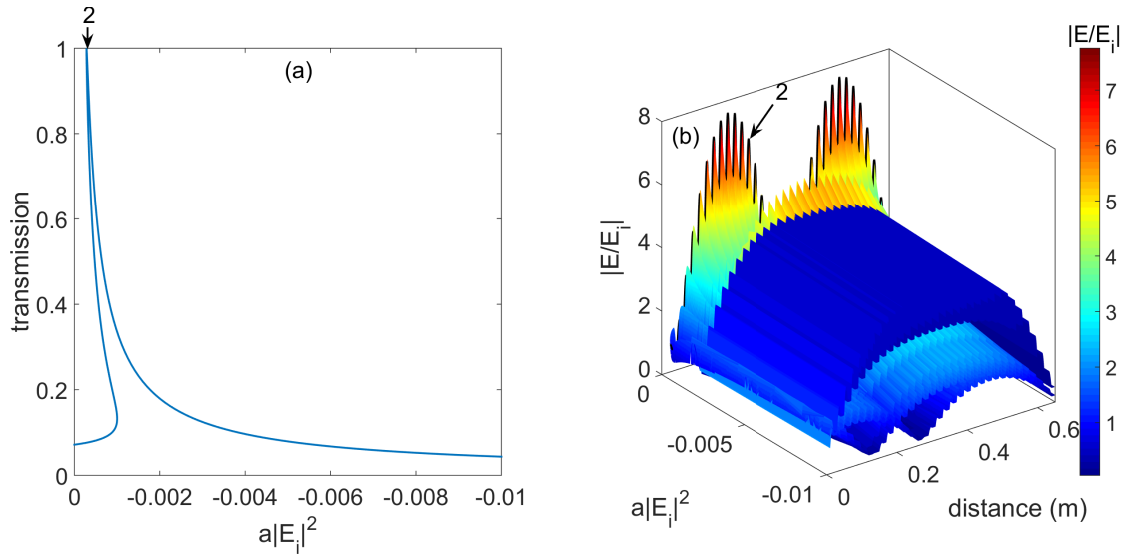

Figure 8: (Color online) Calculated results for the same structure and linear parameters as in Fig 1: (a) Transmission as a function of increasing power of a defocusing nonlinearity for $\theta = \pi/24$ in the case of TE incidence. Only one transparency ($T = 1$) point is found for $\nu = 5.0982$ GHz, at a value of $a|E_i|^2$ (see arrow) equal to -0.00028.; (b) Corresponding spatial profile for the electric field for the two-soliton like mode.
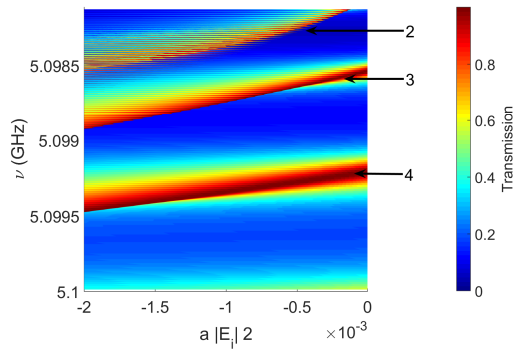
Figure 9: (Color online) Color plot of the transmission coefficient for different values of the nonlinear power and frequencies in the vicinity of the top edge of the PP gap, for the system considered in Fig. 1, with $\theta = \pi/24$ and TE incidence. In red are the regions where we find transparency and soliton modes (see arrows). The n = 2,3,4 arrow numbers indicate the n-soliton modes in the nonlinear power range shown.
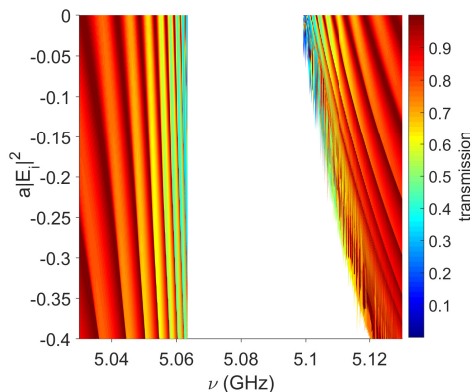

Figure 10: (Color online) Color plot for the transmission coefficient for different values of nonlinear power and frequency for the system considered in Fig. 1, for $\theta = \pi/24$ and TE incidence. For greater clarity, the $T = 0$ gap region is shown in white.

parency point is associated with the one-soliton mode [cf. Fig. 7(a)], we observe that the first transparency point for $\nu = 5.0982$ GHz is associated with a two-soliton mode and no one-soliton mode is observed for this frequency. As shown before for frequencies near the lower edge of the PP gap, Fig. 9 indicates that by choosing frequencies deviating from the top edge of the PP gap, the $T = 1$ curves associated with the n-soliton branch (as illustrated by the arrows) vanish for a frequency ν_n. However, the behavior of the system is dramatically different when comparing the transmission around the lower edge or top edge of the PP gap, as shown in Fig. 10. The top PP gap edge moves to higher frequencies as the nonlinear power increases whereas the bottom PP edge remains essentially unchanged and, therefore, the 'nonlinear gap' becomes larger with increasing self-defocusing nonlinearity.

4. Conclusions

In summary, we have presented a detailed study on the nonlinear transmission switching phenomenon in 1D Kerr/metamaterial heterostructures in the vicinities of both top and bottom edges of the PP-gap under the influence of a self-defocusing Kerr nonlinearity. As expected, we find multi stability, and resonant n-soliton modes. By sweeping the frequency regions around the edges of the PP gap where the linear dispersion relation exhibits a plasmon-polariton coupling, we find different behavior depending on whether the frequency range belongs to the top or bottom edge of the PP gap. The top edge of the gap is shifted to higher frequencies for higher nonlinearities, while the bottom edge remains unchanged. We have found cut-off frequency values ν_n below which there are no n-soliton modes. Furthermore, we find that the depart from the resonant ($T = 1$) transmission frequencies does not hinder soliton formation, although the detuned solitons exhibit smaller amplitudes. Finally, we would like to point out that, in all cases studied in the present work, the transparency-switching phenomenon is still observable at low levels of loss and absorption in the heterostructure. Recent investigations on the experimental fabrication of gain-enhanced metamaterials may open new perspectives to overcome high levels of absorption [18, 19] so that we hope that the present theoretical results will be of interest in future experimental work on nonlinear-heterostructure systems.

5. Acknowledgments

[1] J. Valentine, S. Zhang, T. Zentgraf, E. Ulin-Avila, D. A. Genov, G. Bartal and X. Zhang, Nature **455**, 376 (2008).

[2] J. Valentine, J. Li, T. Zentgraf, G. Bartal and X. Zhang, Nature Materials **8**, 568 (2009).

[3] V. G. Veselago, Sov. Phys. Usp. **10**, 509 (1968).

[4] R. A. Shelby, D. R. Smith, and S. Schultz, Science **292**, 77 (2001).

[5] J. Li, L. Zhou, C. T. Chan, and P. Sheng, Phys. Rev. Lett. **90**, 083901 (2003); H. Jiang, H. Chen, H. Li, Y. Zhang, and S. Zhu, Appl. Phys. Lett. **83**, 5386 (2003).

[6] C. G. Parazzoli, R. B. Greegor, J. A. Nielsen, M. A. Thompson, K. Li, A. M. Vetter, M. H. Tanielian and D. C. Vier, Appl. Phys. Lett. **84**, 3232 (2004).

[7] M. C. K. Wiltshire, J. B. Pendry, I. R. Young, D. J. Larkman, D. J. Gilderdale and J. V. Hajnal, Science **291**, 849 (2001).

[8] A. Fang, T. Koschny, and C. M. Soukoulis, J. Opt. **12**, 024013 (2010).

[9] S. Xiao, V. P. Drachev, A. V. Kildishev, X. Ni, U. K. Chettiar, H-K. Yuan, and V. M. Shalaev, Nature **466**, 735 (2010).

[10] E. Reyes-Gómez, D. Mogilevtsev, S. B. Cavalcanti, C. A. A. Carvalho, and L. E. Oliveira, Europhys. Lett. **88**, 24002 (2009); C. A. A. de Carvalho, S. B. Cavalcanti, E. Reyes-Gómez, and L. E. Oliveira, Phys. Rev. B **83**, 081408(R) (2011).

[11] E. Reyes-Gómez, S. B. Cavalcanti and L. E. Oliveira, Europhys. Lett. **106**, 64001 (2014).

[12] E. Reyes-Gómez, S. B. Cavalcanti, and L. E. Oliveira, Phys. Rev. E **91**, 063205 (2015).

[13] E. Reyes-Gómez, S. B. Cavalcanti and L. E. Oliveira, J. Opt. Soc. Am. B **33**, 320 (2016).

[14] R. S. Hedge and H. G. Winful, Microwave and Opt. Tech. Lett. **46**, 528 (2005).

[15] U. Trutschel and F. Lederer, J. Opt. Soc. Am. B **5**, 2530 (1988).

[16] T. Peschel, P. Dannberg, U. Langbein, and F. Lederer, J. Opt. Soc. Am. B **5**, 29 (1988).

[17] W. Chen and D. L. Mills, Phys. Rev. Lett. **58**, 160 (1987).

[18] A. Pusch, S. Wuestner, J.M. Hamm, K.L. Tsakmakidis and O. Hess, ACS Nano, **6**, 3 (2012).

[19] O. Hess, J.B. Pendry, S.A. Maier, R.F. Oulton, J.M. Hamm and K.L. Tsakmakidis, Nat. Mater., **11**, 7 (2012).